9-29-2017

Visualization and Analysis of a Numerical Simulation of GW150914

Nicole Rosato
ncr8062@rit.edu

Recommended Citation

Rosato, Nicole, "Visualization and Analysis of a Numerical Simulation of GW150914" (2017). Thesis. Rochester Institute of Technology. Accessed from

Visualization and Analysis of a Numerical Simulation of GW150914

by

Nicole Rosato

Thesis Advisor: Dr. Carlos Lousto

A thesis submitted in partial fulfillment of the
requirements for the degree of Master of Science
in Applied and Computational Mathematics

School of Mathematical Sciences

Rochester Institute of Technology

September 29, 2017

Committee Approval

Dr. Carlos Lousto

Professor of Mathematics, School of Mathematical Sciences

Thesis Advisor

Dr. Yosef Zlochower

Associate Professor of Mathematics, School of Mathematical Sciences

Committee Member

Dr. Elizabeth Cherry

Associate Professor of Mathematics, School of Mathematical Sciences

Director, Mathematical Modeling Ph.D. Program

Committee Member

Acknowledgements

To my parents, thank you for your unending support of my pursuit of education, and for providing me with love and guidance through my most difficult challenges. Without either of you, none of this would have been possible. I love you.

I would also like to thank my advisor, Carlos Lousto, for providing support, motivation, and direction during all parts of this thesis, and for helping me navigate through the intricate waters of relativity.

Nicole Rosato
26 July 2017

Abstract

We present a visualization and analysis of a supercomputer simulation displaying the apparent horizons' curvature and radiation emitted from a binary black hole system modeling the LIGO observed signal GW150914. The simulation follows the system from seven orbits prior to merger down to the resultant final Kerr black hole. Apparent horizons are calculated during the simulation with mean curvature data displayed on them. Radiation data was visualized via the real part of the Ψ_4 component of the Weyl scalars, which were determined using a numerical quasi-Kinnersley method. We also present a comparative study of the differences in using the quasi-Kinnersley and PsiKadelia tetrads to construct Ψ_4 and the benefits, particularly in the strong field region of a binary black hole system, of using a tetrad in a transverse ($\Psi_1 = \Psi_3 = 0$) frame. The second part of our studies focus on the relationship between the mean curvature displayed on the apparent horizons and the trajectories of the black holes. We notice that prior to merger, for each black hole, the directionality of the mean curvature tracks that of the trajectory with either a positive or negative phase shift between the two curves. Finally, we provide a brief analysis suggesting that the phase shift and the frame dragging effects are likely related.

Contents

Chapter 1

Introduction

1.1 First Detection of Gravitational Waves

On September 14, 2015, the Laser Interferometer Gravitational Wave Observatory (LIGO) detected a gravitational wave signal from the merger of two binary black holes approximately 1.3 billion lightyears away. The detection of gravitational waves from this system (now referred to as GW150914) was the first of its kind and the significance of such a detection should not be lost on the reader. This confirmation of the existence of gravitational waves provides us with significant assurance of the correctness of the Theory of General Relativity and a strong foundation for the next generation of gravitational wave astrophysics.

1.1.1 How do we detect gravitational waves?

The short answer to this question is with advanced LIGO (aLIGO). More specifically, we use a machine with lasers, long arms, and mirrors called a Michelson interferometer. Currently, there are two active interferometers, one in Livingston, Louisiana, and one in Hanford, Washington, with more coming online in the next few years. The goal is to have as many of these powerful detectors as possible, and to place them at significant distances from each other. This not only helps to verify that a detection is actually a gravitational wave and not some other source of noise, but also helps determine in what area the gravitational wave was emitted from.

Figure 1.1 helps to illustrate exactly how a LIGO Interferometer works. This detector uses very powerful lasers to detect the Earth's stretching and squeezing due to the passage of a gravitational wave.

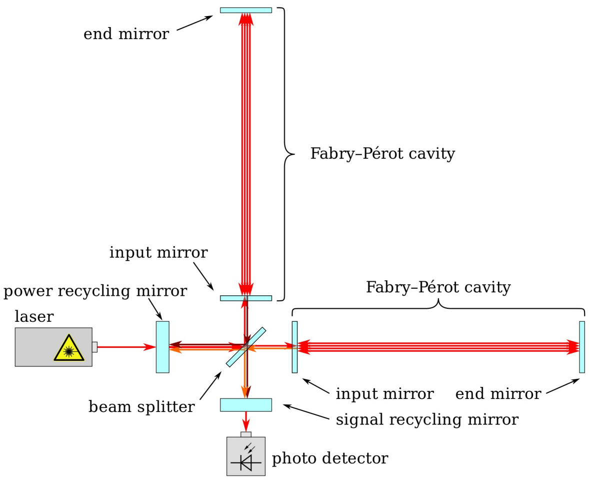

Figure 1.1: An infographic of aLIGO. Each of the Fabry-Perot cavities (referred to as the arms) is 4 km long.

In Figure 1.1 we see a cartoon of a LIGO interferometer with parts labeled. It works by shooting a laser into the beam splitter, which sends photons down each of the perpendicular arms to mirrors that reflect each laser nearly 280 times before the split lasers merge again. These reflections help increase the sensitivity of the detector by increasing the distance traveled by each beam of photons from 4 km to 1120 km. Sensitivity is a key factor here since we are attempting to detect variations in arm length on the order of less than 1/10000th the size of a proton [1].

When a gravitational wave (GW) passes through the LIGO interferometer, the length of one arm will be shortened and the other lengthened by a very small amount, and as the wave passes through the detector, the sizes of the arms oscillates back and forth. This change in arm length causes the lasers in each of the arms to become slightly out of phase with each other, which is measurable when the two beams are recombined in the beam splitter and sent to the photodector. The difference in phase is what is detected, measured, and plotted by LIGO, and both detectors' results are compared to verify that a GW source has actually passed through the detector.

1.1.2 First Detection

During the first (O1) run of aLIGO, a signal was detected on September 14, 2015 and determined to be a gravitational wave with a confidence level of 5.1 σ. Comparison with numerical relativity simulations of gravitational wave strain from binary black hole mergers allowed for the determination of the total mass of the system (62^{+4}_{-3} solar masses), the mass of each black hole (36^{+5}_{-4} and 29^{+4}_{-4} solar masses), and the amount of mass radiated away in gravitational waves ($3 \pm .5$ solar masses) [1] during the inspiral and merger. The figure below, from [1], shows the observed gravitational wave strain overlaid with numerical relativity simulations whose black holes produce gravitational waveforms matching those observed by the detector.

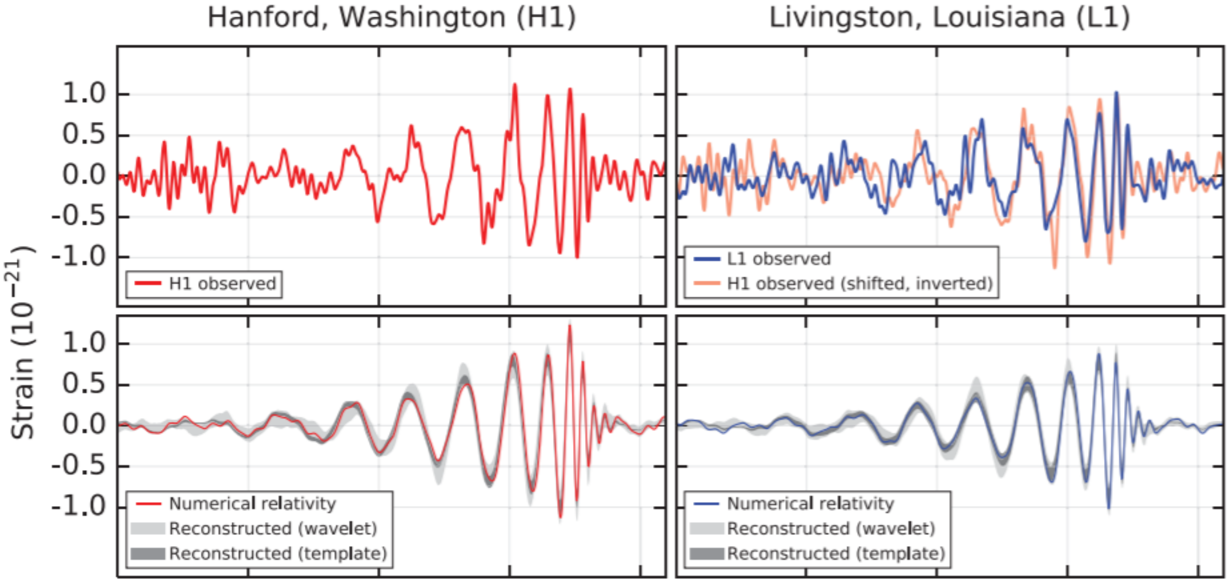

Figure 1.2: The observed gravitational wave in both detectors versus a matching gravitational wave produced by numerical relativity simulations.

It is exciting that observers were able to detect gravitational waves, but we would have not even known what to look for without the numerical relativity simulations that gave us the waveform models in Figure 1.2. In fact, this breakthrough was relatively recent. Up until 2005, researchers were unable to solve the equations of relativity to extract gravitational waves. However, three separate research groups [25], [10], and [6] came up with different methodologies to solve the same problem in 2005 and were finally able to simulate gravitational waveforms. We will discuss some of the techniques used in a more sophisticated fashion throughout this thesis, but an in depth comparison among the techniques is given in [20].

1.1.3 Distinguishing gravitational waves from background noise

Gravitational waves are extremely small perturbations in the fabric of spacetime - they are on the order of 10^{-26} when emitted by large objects like binary black holes, and are even smaller when coming from less compact objects like neutron stars or neutron star black hole binaries. The sensitivity, then, required for a detector like aLIGO to be successful must also be on that order. However, as one would expect aLIGO is obviously able to pick up many other vibrations (earthquakes, cars passing on the road, and refrigerators are just some of the things that have interfered with aLIGO). Small-scale disturbances such as these can be eliminated by the use of multiple detectors; however, we are also limited by the design of aLIGO itself. As discussed before, the length of the arms is what really gives the interferometer its sensitivity, and so obviously one would expect that extending the arm length will increase the sensitivity of the detectors. There are a significant number of non-removable (or very challenging and expensive) sources of noise in the detector itself and, although beyond the scope of this thesis to discuss, the reader is pointed again to [1] for further discussion on potential improvements to aLIGO.

1.2 Numerical Relativity

So far, there have been three confirmed detections of gravitational waves emitted by merging black hole binaries. As more are detected by aLIGO, it will be useful for researchers to have waveforms to compare with the data from observations. A significant amount of time is spent cataloging waveforms of black hole binaries with different mass/spin configurations for exactly this purpose. Since each simulation takes on the order of weeks to months of supercomputer time to complete, improvements to these techniques are always an important aspect of NR research, but will not be the main focus of this thesis. In this section a brief overview of NR is provided and a more in depth, mathematically-based discussion of numerical relativity techniques and methodologies will be the focus of much of the thesis.

Numerical relativity uses an algorithmic, iterative approach to solve the partial differential equations of general relativity and often employs supercomputers to study the coalescence of compact binary objects. Since this thesis focuses on a particular dynamic spacetime, several different methods must be employed to evolve the particular binary system associated with GW150914. First we calculate the initial data of the system based on what we *want* the system to look like - particularly, the mass ratio q and the magnitudes and directions of the spins a_1 and a_2 of the black holes. This initial data is then used in conjunction with the Einstein ToolKit[1] to simulate our particular spacetime.

More generally, however, numerical relativistic techniques can be applied to many areas of general relativity that cannot be solved analytically. They have the benefit of providing us with a solution that is correct (often up to machine precision) and informative, but their detriment is - as always - their computational expense. Supercomputers are often required to assist in solving these complex equations. This is for several reasons: first, spacetimes are discretized into millions of points, and the Einstein Field Equations (EFEs) must be solved at each of these points. Second, the spacetimes that are most interesting are *dynamic*, or changing with time, so not only do we need to solve the EFEs at a large number of points, this needs to be done several hundred (or thousand) times.

Despite this seemingly large obstacle, numerical relativists were able to successfully evolve a binary black hole spacetime through inspiral, merger, and ringdown for the first time in 2005 [25], [10], and [6]. Since then, hundreds more have been completed, without which this thesis would not have been possible. Many technical improvements are being made both to the methodologies and to the supercomputers themselves, which will allow for further, more advanced simulations and breakthroughs in numerical relativity in the coming years.

---

[1] https://einsteintoolkit.org/

1.3 Motivation and Brief Discussion

Although this thesis is motivated in part by the detection of gravitational waves by LIGO in September of 2015, we are also seeking to improve upon existing numerical relativity techniques to further other areas of astrophysics. This is important since there have been three confirmed detections of BBH mergers [2] during LIGO's O1 run and we expect to observe more during the O2 run. Accurate numerical relativity waveforms are key to the identification and confirmation of LIGO's observations. At its most fundamental level a BBH simulation is just a numerical computation of the two-body problem for general relativity, the solution of which has far-reaching applications. In addition to studying the merger of compact objects, improvements in NR techniques will allow us to make great strides in fields such as strong gravity and high-energy physics, higher-dimensional black holes, Trans-Planckian scattering, and alternative theories of gravity. More information on any of these topics can be found in [11], but no further discussion will be provided here.

Specifically, we seek to improve upon and contribute to the current techniques used in numerical relativity simulations of binary black hole systems. Much of the work is background information required to understand and analyze a particular simulation of event GW150914 and the physical properties that are exhibited in a visualization of this simulation, with the final analysis and contribution being held until the final chapters.

The remainder of this thesis is outlined as follows: chapters 2 and 3 provide in-depth mathematical reviews of horizons and radiation respectively. Chapter 4 begins the discussion of the completed visualization of GW150914. It also includes the initial parameters used to configure our particular simulation so that it corresponds with LIGO's observation of GW150914. Chapter 5 is the final content chapter; it looks in depth at features such as horizon curvature changes displayed in the movie and the accuracy of different radiation extraction techniques.

Chapter 2

Horizons

One of the main points of this thesis will be to discuss something called the *mean curvature* of an *apparent horizon*, which can be computed during a binary black hole simulation and then displayed on the apparent horizons of the black holes. In order to understand what apparent horizons are, or what mean curvature tells us, we must first discuss a bit about what a *horizon* is from a mathematical perspective. This chapter begins by discussing necessary concepts from differential geometry and basic properties of manifolds then applies them to astrophysical phenomena relevant to this thesis (namely event and apparent horizons). It is also important to discuss how, in practice, one locates horizons of a black hole both for isolated black holes and when there are two black holes in a binary. We can then finally discuss mean curvature as it is displayed in the visualization and computed in the simulation of event GW150914.

2.1 Manifolds and Tensors

When discussing general relativity, a significant knowledge of differential geometric concepts is required to fully understand the theory. For our purposes, however, we will introduce only concepts that are relevant to the results of our research. The two main topics we will discuss are manifolds and tensors.

2.1.1 Manifolds

When performing mathematical operations between vectors or scalars, we generally perform them on the flat plane $\mathbb{R}^n$. However, performing similar operations on curved or topologically complicated spaces requires the introduction of a mathematical field called a *manifold* on which functions and operators behave locally like they exist on the space $\mathbb{R}^n$, but globally the metric is not necessarily 'topologically flat'. Manifolds are constructed from the union of all such local regions, given that the regions all have the same dimensionality n. It is also important to note that if a space has a point which *locally* does not behave like $\mathbb{R}^n$ anywhere, then it cannot be a manifold. For example, a line intersecting a 2-plane is not a manifold, since the dimensionality of both surfaces is different. Nor is a cone-like shape since there is a non-removable, non-differentiable point in the center. However, a donut-shaped torus is a manifold despite the hole in the center since there are no discontinuities or non-differentiable points on the surface of the torus.

Now that manifolds are somewhat understandable on an intuitive level, it would be helpful to develop a more rigorous definition so that we will be able to discuss horizons and spacetime metrics in great detail. The construction of our definition will follow both Carroll's and Wald's conventions [12], [30]. We begin with some basic notions from Set Theory and Real Analysis, which we can then use to help us construct our definition of a manifold.

Given two sets A and B, define a *map* ψ such that $\psi : A \to B$, where each element in A is mapped to exactly one element in B. A map, like a function, can be injective (one-to-one), surjective (onto), or bijective. Define a map $\psi : \mathbb{R}^m \to \mathbb{R}^n$. Then we have the set of functions:

$$y_1 = \psi_1(x_1, \cdots, x_m) \tag{2.1}$$

$$\vdots$$

$$y_n = \psi_n(x_1, \cdots, x_m). \tag{2.2}$$

A function y_i is called C^p if its p^{th} derivative exists and is continuous. For example, a C^0 function is continuous but is not differentiable everywhere, whereas a function such as $f(x) = e^x$ is called C^∞ or *smooth* since it is infinitely differentiable and always continuous. Furthermore, if a C^∞ map $\phi : A \to B$ exists with inverse $\phi^{-1} : B \to A$ that is also C^∞. Then A and B are *diffeomorphic* and a *diffeomorphism* ϕ exists between them.

Consider vectors $x, y \in \mathbb{R}^n$ and some $r \in \mathbb{R}$. An *open ball* exists where the two norm satisfies $||x - y||_2 < r$. An *open set* is a union of $k \in \mathbb{Z}$ open balls (note that k might be infinite). Define a *chart* as a subset $C \subset A$ which has injective mapping $\psi : C \to \mathbb{R}^n$ where $\psi(C)$ is open in $\mathbb{R}^n$. If this is the case, the *image* $\psi(C)$ is invertible by the injectivity of the mapping ψ and so subset C must be open under A. We can now define an *atlas*, which is a C^∞ collection of charts $(C_\alpha, \psi_\alpha)|\alpha \in \mathbb{Z}^+ \cup 0$ that satisfy

- $\cup_{\alpha=1}^{k} C_\alpha = A$ and
- The maps are smoothly sewn together.

An atlas A that contains all possible charts consistent with A is known as *maximal.* A *manifold* is then a set M with a maximal atlas which contains every possible chart. This means that multiple equivalent spaces which have different atlases are not different manifolds. It is also important to recognize that forcing manifolds to be composed of atlases allows us to perform calculus on the manifold itself. However, atlases are made up of charts that are, by construction, open. This makes it impossible for many manifolds to be covered by one single chart.

Consider the 1-sphere S^1: if we let our coordinates be either $\theta \in [0, 2\pi)$ or $\theta \in (0, 2\pi]$, we have included one point too many and our chart is closed. This means that we need two overlapping open charts to cover the 1-sphere in such a way that it is a manifold. More rigorously, define a chart covering S^1 to be $A : S^1 \backslash (1, 0)$ so that all points except $\theta = 0 \equiv 2\pi$ are included. Define a mapping $\psi_1 : A \to B$ where $B = S^0$ or a line through the coordinates $(1, \pi)$ on the unit circle. Our mapping works via stereographic projection - to see what this is, draw a line l from $(1, 0)$ through the circle to any point on the set of points B. The line l should intersect the open 1-sphere at two points: first at $(1, 0)$ and second at some arbitrary point (r, θ). If we project every point on the 1-sphere to every point on the line, we have successfully utilized the mapping $\psi_1 : A \to B$. Define a second mapping $\psi_2 : S^1 \backslash (1, \pi) \to B$ where this time B passes through the coordinates $(1, 0)$. If we use ψ_1 and ψ_2 in this way, we have successfully covered the manifold S^1 with two open charts and have satisfied our definition.

In fact, this method can be used to show that any n-sphere of radius $r = 1$ can be covered in two open charts in exactly the same way. We will not prove this rigorously, but will provide general formulas for the charts which work for any n-dimensional sphere. Consider

$$S^n = \sum_{i=0}^{n} (x_i)^2 = 1. \tag{2.3}$$

the atlas with two charts is given by [12]

$$C_\alpha = S^n \backslash (\pm 1, 0, \cdots, 0) \text{ and} \tag{2.4}$$

$$\psi_\alpha = \frac{1}{\pm 1 - x_0}(x_1, \cdots, x_n) \tag{2.5}$$

$$\tag{2.6}$$

which cover the manifold completely for any n-sphere S^n. Since many concepts in general relativity are based around manifolds and depend so heavily on coordinate systems, this brief outline of some of these basic concepts will allow us to discuss in depth spacetime metrics and curvature in the following few sections.

2.1.2 Coordinate Definitions, Invariance, and Minkowski Space

Both general relativity (GR) and special relativity (SR) work in four-dimensional space consisting of three spatial dimensions and one dimension t for time. We consider $t = c\tau$ where $c = 3 \times 10^8$ meters per second is the speed of light. The units are then scaled so that $c = 1$ and thus time is measured such that 1 second is equivalent to 3×10^8 meters. The spatial coordinates we work with can be Cartesian, polar, or spherical, and depend entirely on the form of the *metric* we are using and what type of surface we are working on. Coordinates themselves are typically denoted using numbers rather than Greek or Latin letters, unless we are working in a specific coordinate system. In this thesis we will choose x^0 to be our time component and the remainder $x^1,\ x^2,\ x^3$ will be our spatial components:

$$(x^0, x^1, x^2, x^3) \equiv (t, r, \theta, \phi) \tag{2.7}$$

Here we could have used also (t, x, y, z). Our choice of using polar coordinates was arbitrary and more meant to be illustrative of how the components correspond to the indexed x^i's. Later on we will discuss the importance of choosing a proper *coordinate system* which is not necessarily the same as choosing (t, x, y, z) over (t, r, θ, ϕ) or vice versa.

It now seems natural to discuss the notion of *coordinate invariance*. Many interesting geometrical features of a spacetime are independent of the choice of coordinates, by which we mean that they maintain their properties no matter what the explicit coordinate values are. Take, for example, the distance between two Cartesian points x and y. The distance $d = \sqrt{x^2 + y^2}$ is maintained even if the two points x and y are relabeled using polar coordinates (r_1, ϕ_1) and (r_2, ϕ_2). This means that d is *coordinate invariant*, and is the same regardless of the coordinate system chosen. Coordinate invariance is important in GR since we want to be able to calculate, simulate, and understand real physical quantities extracted from the Einstein equations that are independent of our choice of coordinate system. These quantities must be the same across all coordinate systems, else the physicality of the results can be called into question.

2.1.3 The Metric $g_{\mu\nu}$ and Tensors

In special relativity, we write the infinitesimal separation of two objects using a *spacetime interval* or *metric*:

$$ds^2 = -dt^2 + dx^2 + dy^2 + dz^2 \tag{2.8}$$

which allows us to compare *local intertial frames*. These describe a homogenous, isotropic, and time independent spacetime which means that objects moving within a local inertial frame cannot detect motion. This can be written as a tensor equation using the *Minkowski metric* $\eta_{\mu\nu}$:

$$ds^2 = \eta_{\mu\nu} dx^\mu dx^\nu \tag{2.9}$$

also known as a *line element* where

$$\eta_{\mu\nu} = \begin{pmatrix} -1 & 0 & 0 & 0 \\ 0 & 1 & 0 & 0 \\ 0 & 0 & 1 & 0 \\ 0 & 0 & 0 & 1 \end{pmatrix} \tag{2.10}$$

describes the same homogeneous, isotropic spacetime. Equation (2.9) is a tensor equation, and we are using Einstein's summation convention here, in which these *dummy indices* are summed over when they appear as a pair in an equation as both a super- and sub-script.

It is important to mention here the concept of a *geodesic*. A *geodesic* is a way of relating curved space to flat space. Particles under the influence of gravity travel along geodesics through spacetime. When we say something moves along a geodesic, we mean an extremal curve; null curves have zero length (thus so do null geodesics), spacelike curves between two events are of minimum length and timelike curves are of maximum length. So, when we say a particle travels along a timelike geodesic, it is traveling along a path of maximum size along a timelike curve. It is important to also add that massless particles travel along null geodesics. Massive particles cannot travel along spacelike geodesics, this would require faster than light travel since we can think of spacelike geodesics as lateral lines through space with no change in proper time.

2.1.4 Tensors

In Section 2.1.1 we learned about differentiable, n-dimensional spaces called manifolds. We also discussed that manifolds are covered by *charts* which are one to one mappings from $\mathbb{R}^n \to M$. We can also define a *curve* on a manifold to be a function from a segment of the real line into the manifold, for example, the curve x^α can be written $x^\alpha(\lambda)$ for $\lambda \in \mathbb{R}$. A *vector* is simply a set of points tangent to the curve, which can be represented as a linear combination of basis vectors $\vec{e}_\alpha$ which will be important in the coming chapters:

$$\vec{v} = v^\alpha \vec{e}_\alpha. \tag{2.11}$$

In Equation (2.11), we have a vector $\vec{v}$ made up of its components v^α and basis vectors $\vec{e}_\alpha$. Defining the basis vectors to be

$$\partial_\alpha = \vec{e}_\alpha \tag{2.12}$$

sets up a *coordinate basis* where basis vectors $\vec{e}_\alpha$ are chosen to point along the coordinate axes. As we will see in Chapter 3, coordinate bases are not always the most prudent choice, since they are neither normalized nor orthogonal to each other.

A similar object to a vector is a *one-form* (or *covector*). A covector q takes a vector $\vec{v}$ and maps it to the real numbers, so $q(\vec{v}) \in \mathbb{R}$. Consider a set of basis dual vectors $\vec{\omega}^\alpha$ such that

$$\vec{\omega}^\alpha(\vec{e}_\beta) = \delta^\alpha_\beta \tag{2.13}$$

where δ^α_β is the Kroenecker-delta function:

$$\delta^\alpha_\beta = \begin{cases} 1 & \text{if } \alpha = \beta \\ 0 & \text{else.} \end{cases} \tag{2.14}$$

This allows us to write one-forms in terms of components such that $q = q_\alpha \vec{\omega}^\alpha$ which we will denote q_α for simple indexing.

An operation one can perform on a vector or a one-form is a *contraction*, which has the benefit of providing a real number which is independent of the coordinate basis chosen. To contract over indices, we do the following:

$$q_\alpha v^\beta \delta^\alpha_\beta = q_\alpha v^\alpha. \tag{2.15}$$

We are now ready to define a *tensor* T. Consider real valued functions of m one-forms and n vectors with linear arguments. These functions are tensors of type (m, n) such that:

$$T^{\alpha\beta}{}_{\mu\nu} = T(q^\alpha, q^\beta; \vec{e}_\mu, \vec{e}_\nu) \tag{2.16}$$

is a $(2, 2)$ tensor with one-forms identified by the superscript of q^λ and basis vectors $\vec{e}_\lambda$.

2.1.5 The metric $g_{\mu\nu}$

Consider a vector $\vec{v}$ for which we can define the length of the vector to be the 2-norm

$$||v||_2 = \sqrt{\vec{v} \cdot \vec{v}}. \tag{2.17}$$

The $(0, 2)$ tensor $g_{\mu\nu}$ can be used to define the distance between any two arbitrarily close points via

$$ds^2 = g_{\mu\nu} dv^\mu dv^\nu, \tag{2.18}$$

where the operator $g(\vec{v}, \vec{v}) = ||v||_2^2$. The *signature* of the metric $g_{\mu\nu}$ is given by the signs of the eigenvalues of the matrix components of the metric and is written, for Lorentzian metrics (with three spatial dimensions), to be $(-, +, +, +)$. We can use the metric tensor to raise and lower indices:

$$v_\beta = g_{\alpha\beta} v^\alpha. \tag{2.19}$$

Furthermore, the metric is assumed to be nonsingular with inverse $g^{\mu\nu}$ and thus its determinant g is always nonzero. Under $g_{\mu\nu}$ vectors and one-forms can be used interchangeably and indices (denoting the components of a vector $\vec{v}$) can be raised and lowered via the metric:

$$v_\mu = g_{\mu\nu} v^\nu \tag{2.20}$$

$$v^\mu = g^{\mu\nu} v_\nu \tag{2.21}$$

and the dot product of two vectors $\vec{v}$ and $\vec{u}$ is computed:

$$\vec{v} \cdot \vec{u} = g_{\mu\nu} v^\mu u^\nu = v_\mu u^\mu. \tag{2.22}$$

2.1.6 The Connection

It will be useful to here define several operations which involve the metric. We begin by writing a connection, which is vital in describing curvature. A connection transports vectors among tangent spaces and is thus a way of relating vectors in tangent spaces. There are two operators which are described via the term connection; the first is the *Christoffel symbol* $\Gamma^\lambda_{\mu\nu}$ which is given by

$$\Gamma^\lambda_{\mu\nu} = \frac{1}{2} g^{\lambda\sigma} (\partial_\mu g_{\nu\sigma} + \partial_\nu g_{\sigma\mu} - \partial_\sigma g_{\mu\nu}), \tag{2.23}$$

also called a connection coefficient. The second is the *covariant derivative* ∇_μ of a vector field $\mathbf{v}^\nu$ and uses the Christoffel symbol:

$$\nabla_\mu \mathbf{v}^\nu = \partial_\mu \mathbf{v}^\nu + \Gamma^\nu_{\mu\lambda} \mathbf{v}^\lambda. \tag{2.24}$$

Connection coefficients or Christoffel symbols also help us determine whether a curve $x^\mu(\lambda)$ is geodesic via the *geodesic equation* where

$$\frac{d^2 x^\mu}{d\alpha^2} + \Gamma^\mu_{\rho\sigma} \frac{dx^\rho}{d\alpha} \frac{dx^\sigma}{d\alpha} = f(\alpha) \frac{dx^\mu}{d\alpha} \tag{2.25}$$

for arbitrary parameter $\alpha(\lambda)$ where λ is an *affine parameter*. An affine parameter is one which is related to proper time τ in the following way:

$$\tau \to \lambda = a\tau + b \tag{2.26}$$

for constants a, b. The geodesic equation can also be written as

$$u^{\mu}\nabla_{\mu}u^{\alpha} = 0 \tag{2.27}$$

where $\vec{u}$ is the four-veolocity $u^{\alpha} = dx^{\alpha}/d\tau$.

2.1.7 Curvature Tensors and the Einstein Field Equations

To continue our discussion of spacetime curvature, we must now study the mathematical objects which represent curvature and spacetime itself. The gravitational field is measured by the spacetime curvature generated by matter. This is quantified by the *stress-energy tensor* T^{ab}, which encodes the energy, momentum, and stress of matter on a spacetime. It should follow then that in a vacuum T^{ab} vanishes.

Related to the stress-energy tensor is the Riemann Tensor R_{abcd}, which measures the curvature of a gravitational field and has the form

$$R_{abcd} = \partial_c \Gamma^a{}_{bd} - \partial_d \Gamma^a{}_{bc} + \Gamma^a{}_{ec}\Gamma^e{}_{bd} - \Gamma^a{}_{ed}\Gamma^e{}_{bc}, \tag{2.28}$$

which in flat spacetime is such that $R_{abcd} = 0$ since there is no curvature. The Riemann tensor obeys the following identities:

- Antisymmetry in its first two indices, last two indices, and symmetry between pairs of indices:

$$R_{abcd} = -R_{bacd} \qquad R_{abcd} = -R_{abdc} \qquad R_{abcd} = R_{cdab} \tag{2.29}$$

- Cyclic identity:

$$R_{abcd} + R_{adbc} + R_{acdb} = 0 \tag{2.30}$$

- Bianchi identities:

$$\nabla_e R_{abcd} + \nabla_d R_{abec} + \nabla_c R_{abde} = 0. \tag{2.31}$$

From R_{abcd} we can define the Ricci tensor and Ricci scalar (respectively):

$$R_{ab} = R^{c}{}_{acb}, \tag{2.32}$$

$$R = R^{a}{}_{a}, \tag{2.33}$$

where R_{ab} has ten independent components and is the trace of R_{abcd} [12]. The trace-free component is known as the Weyl Tensor, which will be discussed in great detail in Chapter 3. We can use R_{ab} and R to define the symmetric Einstein tensor

$$G_{ab} = R_{ab} - \frac{1}{2} g_{ab} R, \tag{2.34}$$

which is related to T_{ab} via Einstein's Field Equations

$$G_{ab} = 8\pi T_{ab}, \tag{2.35}$$

and the inclusion of the cosmological constant Λ gives the true form of the EFEs:

$$G_{ab} + \Lambda g_{ab} = 8\pi T_{ab}. \tag{2.36}$$

The constant Λ is negligible when considering black hole spacetimes, however, so we set $\Lambda = 0$ during our evolutions. The cosmological constant is relevant only when considering problems on a much larger scale, such as the expansion of the universe. Therefore, for the remainder of this thesis the reader should assume $\Lambda = 0$ in the construction of the EFEs and their subsequent numerical evolution.

2.2 Event and Apparent Horizons

Now that we have defined relevant concepts from differential geometry and topology, we are able to move on to a discussion about horizons. From a theoretical perspective, one must first understand what an event horizon is and how it is found both numerically and analytically. We will then move on to discussing apparent horizons, the distinction between the two types of horizons, and why we choose to use apparent horizons in our simulations rather than event horizons.

2.2.1 Black Holes and Event Horizons

We can simply and nonrigorously define an *event horizon* as being a surface past which neither massive nor massless particles can escape outward to spatial infinity. It is a null surface, rather than a timelike one, which means that the vectors normal to it are all null, or have zero length. We can then colloquially define a *black hole* as being a region of spacetime separated from the rest of spacetime and therefore null infinity by an event horizon. It is important to recognize that the region of spacetime outside of a black hole behaves exactly the same way as the region of spacetime surrounding a star or planet of equal mass.

There are also different types of black holes, all of which come out of different spacetime metrics; some are physical and some are likely not. We will discuss two physical types here: Schwarzschild black holes, which are uncharged and nonrotating, and Kerr black holes, which are rotating and uncharged. Kerr black holes were the type used to produce many of the results of this thesis.

Spacetime Metrics

Consider the Schwarzschild metric

$$ds^2 = -\left(1 - \frac{2M}{r}\right) dt^2 + \left(1 - \frac{2M}{r}\right)^{-1} dr^2 + r^2 d\theta^2 + \sin^2\theta d\phi^2, \tag{2.37}$$

where M is the mass of the body in question, with coordinates (t, r, θ, ϕ). The surface area $\mathcal{A}$ of the black hole is measured with respect to the radius of the event horizon $r = r_H$, and for an arbitrary $r = constant$ surface the area is given by

$$\mathcal{A} = \int \sqrt{|\gamma|} d\theta d\phi, \tag{2.38}$$

where γ_{ij} is the induced metric, which is obtained using the metric g_{ab} and $dt = dr = 0$. For any surface of radius $r = constant$, the surface area is found to be

$$\begin{aligned} \mathcal{A} &= \int_0^{2\pi} \int_0^{\pi} \sqrt{g_{\theta\theta} g_{\phi\phi}} d\theta d\phi \qquad (2.39) \\ &= \int_0^{2\pi} \int_0^{\pi} r^2 \sin\theta d\theta d\phi. \qquad (2.40) \end{aligned}$$

This equation can be used to find the surface area of the event horizon A_H by setting $r = r_H$. So

$$A_H = 4\pi r_H^2 \tag{2.41}$$

which, for the event horizon of a Schwarzschild black hole, where $r_H = 2M$, is

$$A_H = 16\pi M^2. \tag{2.42}$$

Notice that there are two singular points in the Schwarzschild metric: at radii $r = 2M$ and $r = 0$. The singularity at $r = 2M$ is called a *coordinate singularity* and can be removed by deriving a metric for the Schwarzschild spacetime in a different coordinate system. For example, in the *Kruskal-Szekeres* coordinate system, there exists no singularity at $r = 2M$:

$$ds^2 = \frac{32M^3}{r} e^{-r/2M} \left(-dv^2 + du^2\right) + r^2 d\theta^2 + r^2 \sin^2\theta d\phi^2. \tag{2.43}$$

where

$$v = (r/2M - 1)^{1/2} e^{r/4M} \sinh(t/4M) \tag{2.44}$$

$$u = (r/2M - 1)^{1/2} e^{r/4M} \cosh(t/4M). \tag{2.45}$$

The singularity that exists at $r = 0$, however, is a real, physical singularity that cannot be removed regardless of our choice of coordinates and in fact describes the singularity inside of a black hole.

The Kruskal-Szekeres coordinates are useful because they describe the full spacetime manifold; encoded in the metric is a description of a universe with a black hole as well as another parallel universe with a white hole. A helpful visualization is a Kruskal-Szekerez diagram, as shown in Figure 2.1.

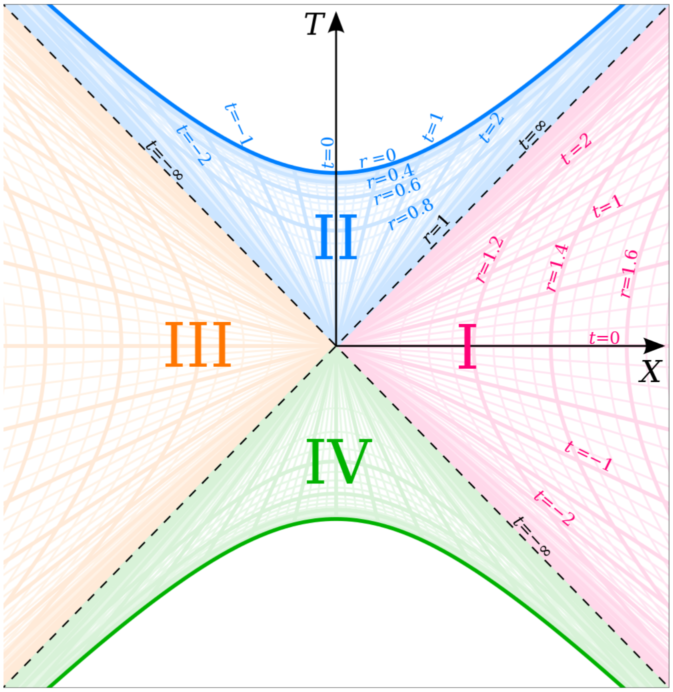

Figure 2.1: Kruskal-Szekeres diagram that covers the full spacetime manifold. The black hole and its corresponding spacetime are regions II and I respectively, and the white hole and its spacetime are regions IV and III respectively.

In Figure 2.1 there are four distinct regions of spacetime. Region I corresponds to our universe, region II is the interior of a black hole, region III is another universe inaccessible to us, and region IV is the interior of a white hole. Lines of constant time $t = constant$ extend outward radially from the origin of the diagram, while lines of constant radius are hyperbole. Regions II and IV have $r < 2M$ and regions I and III have $r > 2M$ with the $u = \pm v$ lines describing the event horizons of both black holes. The outermost hyperbole in the white and black hole regions represent the singularities of each object. At the singularities we have $r = 0$ and $v = \sqrt{1+u^2}$ for the black hole, and $r = 0$ with $v = -\sqrt{1+u^2}$ corresponding to the white hole.

We can relate these $u - v$ coordinates to the $t - r$ coordinates in Equation (2.37) depending on the quadrant in Figure 2.1. For the regions outside the event horizons, we have

$$v = \pm(r/2M - 1)^{1/2} e^{r/4M} \sinh(t/4M), \tag{2.46}$$

$$u = \pm(r/2M - 1)^{1/2} e^{r/4M} \cosh(t/4M), \tag{2.47}$$

where we take + if in region I and − if in region III. For the regions inside the event horizons the equations become

$$v = \pm(r/2M - 1)^{1/2} e^{r/4M} \cosh(t/4M), \tag{2.48}$$

$$u = \pm(r/2M - 1)^{1/2} e^{r/4M} \sinh(t/4M), \tag{2.49}$$

where + corresponds to the black hole region and − corresponds to the white hole region.

2.2.2 Kerr Black Holes

The previous section describes spacetimes which include non-rotating, uncharged black holes. Although these types of spacetimes are useful for helping us understand basics of black holes and how metrics work, the more physically interesting and relevant cases begin with adding rotation into our metric. To do this, we use the *Kerr Metric* [12]:

$$ds^2 = -\left(1 - \frac{2Mr}{\Sigma}\right) dt^2 - \frac{2aMr\sin^2\theta}{\Sigma}(dtd\phi + d\phi dt) \frac{\Sigma}{\Delta} dr^2 + \Sigma d\theta^2 + \frac{\sin^2\theta}{\Sigma}\left((r^2+a^2)^2 - a^2\Delta\sin^2\theta\right) d\phi^2 \tag{2.50}$$

with

$$a \equiv J/M, \quad \Delta \equiv r^2 - 2Mr + a^2, \quad \Sigma \equiv r^2 + a^2\cos^2\theta. \tag{2.51}$$

This metric uses *Boyer-Lindquist coordinates*, which have (t, r, θ, ϕ), although other formulations of this metric exist. Angular momentum of the black hole is given by J and the spin is scaled by M and restricted by $0 \leq a/M \leq 1$, where a maximally spinning black hole has $a/M = 1$, although this particular case is nonphysical. The horizon surface area, found using Equation (2.38), is $\mathcal{A} = 4\pi(r_+^2 + a^2)$ and is again used to help find the radius of the event horizon. There are two significant physical properties of this black hole. The first is called a *stationary limit surface*, which exists outside of the black hole itself, but allows for the existence of no static observers (who do not change position with respect to time) between it and the event horizon, in a region called the *ergosphere*. To find the location of the stationary limit surface, take the largest root of $g_{tt} = 0$, which is

$$r_{ergo} = M + (M^2 - a^2\cos^2\theta)^{1/2}. \tag{2.52}$$

Any timelike observers in this region are dragged along in the direction of rotation of the black hole. The ergosphere coincides with the event horizon only at the poles $\theta = 0$ and π. We will return to this in Chapter 5 when we discuss frame dragging. The second important physical property is the horizon of a black hole, to which much of this thesis is dedicated.

2.2.3 Event Horizons

When we discuss something existing inside a black hole, what we actually mean is that it exists inside the event horizon of a black hole. Colloquially, an event horizon is where no timelike paths exist for particles, massless or massive, to escape out to $r = \infty$. We can define an event horizon more rigorously, and we will use that definition to help motivate the coming few sections.

An event horizon is a global quantity; it is a $2+1$ dimensional null hypersurface in spacetime, so it is characterized by one time dimension and two spatial dimensions. It is formed by outward pointing future directed null geodesics which neither fall into the black hole nor escape outward to infinity; they remain on the event horizon for all time. It is helpful to think of null hypersurfaces as formed by null geodesics $x^\mu(\lambda)$ such that vectors tangent to these geodesics ξ^μ are proportional to the normal vectors $\partial_\mu f$ where

$$\xi^\mu = \frac{dx^\mu}{d\lambda} = h(x) g^{\mu\nu} \partial_\mu f, \tag{2.53}$$

in which we choose affinely parameterized h so that $\xi_\mu \xi^\mu = 0$ and $\xi^\mu \nabla_\mu \xi^\nu = 0$.

Consider the horizon H intersected with a spacelike $t =$ const hypersurface Σ. This provides us with a closed, 2D surface with surface area $\mathcal{A}$. The area of the horizon itself is nondecreasing ($dA \geq 0$) by the **null area theorem**, which states that given weak energy condition and cosmic censorship, the area of an event horizon in an asymptotically flat spacetime is nondecreasing.

From the null area theorem, we can define the *irreducible mass* of a black hole M_{irr}, which is the minimum amount of mass a black hole of surface area $\mathcal{A}$ can have and is also nondecreasing.

$$M_{irr} = \left(\frac{A}{16\pi}\right)^{1/2} \tag{2.54}$$

The null area theorem also gives us an upper limit to the gravitational energy emitted during binary black hole mergers although, in practice, these mergers emit far less than this theoretical upper bound. We can use M_{irr} to help us determine the mass of a black hole. For example, the mass of a Kerr black hole can be calculated via

$$M^2 = M_{irr}^2 + \frac{1}{4}\frac{J^2}{M_{irr}^2} \tag{2.55}$$

for angular momentum J and such that $\frac{M^2}{M_{irr}^2} \leq 2$ with $J = M^2$ being the extremal case.

To the uninformed, yet perceptive reader, a natural question now arises: do event horizons always exist? A naked singularity is one that exists enshrouded in no event horizon; in theory, these singularities would allow for timelike geodesics to pass by them arbitrarily closely, yet still escape to infinity. If the singularity were *not* naked, i.e. if it had an event horizon, that same timelike geodesic would be trapped within the event horizon and eventually fall to the singularity. The **Weak Cosmic Censorship Conjecture** states that naked singularities cannot exist as products of gravitational collapse from generic, initially nonsingular states in an asymptotically flat spacetime obeying the dominant energy condition. There is also the **Strong Cosmic Censorship Conjecture** which exists independent from the weak verson. It states, colloquially, that no singularity is ever visible to any observer, apart from an initial big-bang singularity. This holds for some spacetimes and not others and, in particular, we will focus on those spacetimes which this does not hold. For more information on Cosmic Censorship see [12] and [30].

Finding Event Horizons

In a spacetime that is stationary and asymptotically flat whose event horizons have spherical topology, it is straightforward to find an event horizon. The Schwarzschild metric provides us with one such case of this, so a natural first step is to find an event horizon in a Schwarzschild spacetime. In fact, we have already done this when we used Equation (2.38) for horizon surface area and found $r = r_H = 2M$.

In this section, however, we will discuss how horizons are found based on their differential geometric properties, rather than just providing a formula. For now, we will consider the Schwarzschild metric in Equation (2.37) to help us find the event horizon. This can be done in two ways, the first is the following: we can look at where a radially infalling light ray has zero velocity, which means

$\frac{dr}{dt} = 0$. Radially infalling implies $d\phi = d\theta = 0$, so the ray is changing only its radial distance from the black hole with respect to time and is not varying in any angular direction. We know light travels on a null geodesic so

$$0 = -\left(1 - \frac{2M}{r}\right) dt^2 + \left(1 - \frac{2M}{r}\right)^{-1} dr^2, \tag{2.56}$$

$$\frac{dr^2}{dt^2} = \left(1 - \frac{2M}{r}\right)^2, \tag{2.57}$$

$$\frac{dr}{dt} = \left(1 - \frac{2M}{r}\right), \tag{2.58}$$

and since we want $\frac{dr}{dt} = 0$, we find that

$$\frac{dr}{dt} = \left(1 - \frac{2M}{r}\right), \tag{2.59}$$

$$0 = \left(1 - \frac{2M}{r}\right), \tag{2.60}$$

$$r_H = r = 2M \tag{2.61}$$

is where the event horizon occurs. However, this method is not coordinate-independent. It is clear to see that for a different formulation of the coordinates, we might find $r = r_H$ occuring at different values of r.

Killing Horizons

We can also use the *killing vectors* $\partial_\sigma = K$ of a stationary spacetime to help us find an event horizon. A vector K is a killing vector if

$$\nabla_{(\mu} K_{\nu)} = 0. \tag{2.62}$$

where the parentheses around the indices imply symmetry (square brackets would denote antisymmetry). In particular, we are interested in Killing vectors $\partial_t = K$ that are asymptotically timelike with respect to radius r. Such vectors define stationary spacetimes. If we let $\partial_t g_{\mu\nu} = 0$, we have rewritten our metric so that it is time-independent, which will give us hypersurfaces of $t = constant$ with different (r, θ, ϕ) which asymptotically behave like Minkowski space. All $r = constant$ hypersurfaces Σ_r are of the form $S^2 \times \mathbb{R}$. As discussed earlier, it is possible that decreasing inward from $r = \infty$ gives timelike hypersurfaces for $r > r_H$, but at $r = r_H$, the hypersurface will be null provided that we have chosen an appropriate coordinate system [12]. To find this location, consider the one-form $\partial_u r$ that is normal to $t = constant$ hypersurfaces whose norm is given by

$$g^{\mu\nu}(\partial_\mu r)(\partial_\nu r) = g^{rr} \tag{2.63}$$

such that $g^{rr}(r) = 0$ where $r = r_H$. This method is particularly nice because, so long as coordinates are chosen appropriately, this method works not only for Schwarzschild, but also for Kerr (spinning, uncharged) and Reissner-Nordstrom (charged, nonspinning) black holes.

Consider a Killing vector field X^μ and a hypersurface Σ such that X^μ is null along Σ. Then, Σ is a **Killing horizon** of X^μ. Furthermore, an event horizon Σ is a Killing horizon if it exists in a stationary, asymptotically flat spacetime such as Schwarzschild. In the case of a spacetime that is axially symmetric and stationary, but not spherically symmetric (Kerr, for example) the event horizon is a Killing horizon for a linear combinations of Killing vectors with rotations R^μ and time translations K^μ [12]. This means that the killing vector field X^μ is given by the linear combination $X^\mu = K^\mu + \Omega R^\mu$ where Ω is the horizon angular velocity.

The Kerr metric in Boyer-Lindquist is one that has a timelike and a rotational Killing vector

$$K = \partial_t, \tag{2.64}$$

$$R = \partial_\phi. \tag{2.65}$$

The rotational symmetry is described by Killing vector R^μ, and the timelike Killing vector K^μ is not normal to *any* hypersurfaces [12]. The rotational symmetry implies the black hole is spinning the same way for all time and so is stationary; however, since we cannot reverse the angular momentum of the black hole, it is not time-reversal-invariant and thus not static.

Now we will try to apply Equation (2.63) to the Kerr metric (Equation (2.50)) in Boyer-Lindquist coordinates so that

$$0 = g^{rr} \tag{2.66}$$

$$= \frac{\Delta}{\Sigma} \tag{2.67}$$

$$= r^2 - 2Mr + a^2 \tag{2.68}$$

$$\implies r_\pm = M \pm \sqrt{M^2 - a^2}, \tag{2.69}$$

which, if $a \to 0$, approaches $r_+ = 2M$ and therefore is exactly the event horizon for a Schwarzschild black hole. Both r_+ and r_- are null surfaces, but we consider the outermost surface r_+ to define the event horizon since it is the boundary between the inside of a Kerr black hole and the rest of spacetime. As has already been discussed the Kerr spacetime is stationary but not static, which means that the associated timelike Killing vector $K^\mu = \partial_t$ is not null on the Killing horizon.We can easily show this by calculating the norm $K^\mu K_\mu$ and showing that it does not vanish for either $r = r_+$ or $r = r_-$:

$$K^\mu K_\mu = -\frac{1}{\Sigma}(\Delta - a^2 \sin^2\theta). \tag{2.70}$$

For $r = r_+$, recall

$$r = M + \sqrt{M^2 - a^2}, \tag{2.71}$$

$$\Sigma = r^2 + a^2 \cos^2\theta, \tag{2.72}$$

$$\Delta = r^2 + a^2 - 2Mr. \tag{2.73}$$

Then

$$K^\mu K_\mu = -\frac{1}{\Sigma}(\Delta - a^2 \sin^2\theta) \tag{2.74}$$

$$= \frac{a^2 \sin^2\theta}{2M(M + \sqrt{M^2 - a^2}) - a^2 \sin^2\theta}, \tag{2.75}$$

which vanishes only at the north and south poles $\theta = 0,\ \pi$ of the black hole. For $r = r_-$ we find:

$$K^\mu K_\mu = -\frac{1}{\Sigma}(\Delta - a^2 \sin^2\theta) \tag{2.76}$$

$$= \frac{a^2 \sin^2\theta}{2M(M - \sqrt{M^2 - a^2}) - a^2 \sin^2\theta}, \tag{2.77}$$

which also vanishes only for $\theta = 0,\ \pi$. So, the Killing vector K^μ is spacelike at $r = r_\pm$ and thus is not null on the hypersurface defined by $r = r_+$, despite it being a Killing horizon. In fact, the location where $K^\mu K_\mu = 0$ occurs at the *stationary limit surface.* Inside of this hypersurface, a region called the *ergosphere* exists, in which timelike paths are dragged along with respect to the rotation of the black hole. For more information regarding Killing vectors and Killing horizons, see [12] and [30], from which much of this section was derived.

Numerical Computation of Event Horizons

It seems, from the construction of an event horizon discussed in Section 2.2.3, and from the computations above, that determining the location of an event horizon analytically is simple and can be done relatively inexpensively. However, for interesting systems, this is not the case. The event horizon is a *global* quantity that is not easy to locate numerically. To find an event horizon, we need to send null geodesics outward from a source and see if they escape off to spatial infinity as $t \to \infty$. This is something that can only be answered after the full evolution of a spacetime. The event horizon size and location are dependent on the mass of the black hole, and if that varies, then so do the corresponding properties of the event horizon. So, for spacetimes that have significant changes happening like binary black hole systems, the event horizon cannot be computed along with the spacetime.

As an intuitive exercise, assume the location of an event horizon is known at time t_0 and at time t_1 send a geodesic outward from $r = r_H + \epsilon$, so just outside the horizon surface. At the same time, assume a particle falls into the black hole that increases its radius so that $r_H \geq r_H + \epsilon$. The null geodesic is no longer able to escape the event horizon of the black hole, despite having started from outside the horizon. We would have needed to know information about the infalling particle in advance in order to accurately say whether the null geodesic would be able to escape off to infinity, even though that is information unavailable to us when calculating the geodesic's path.

Assuming we want to study event horizons, how do we rectify this conundrum? A method of spacetime evolution effectively excises the interior of the black holes at $r < r_H$ and therefore gets rid of the problem of the singularity at their centers. This requires at least approximate knowledge of event horizon locations while the simulation is progressing, which for unchanging spacetimes we can do since the event horizons remain of constant size, but for any interesting spacetimes this is knowledge that we have already shown, at least intuitively, to be unavailable to us during evolution.

That said, we can in fact calculate event horizons numerically, but we are required to have full knowledge of the spacetime beforehand. What this means is that we can calculate the event horizons only after the spacetime has been fully evolved and has settled to its final state. So, after we have fully evolved the spacetime, we must go back and compute the event horizons using knowledge of the final form of the spacetime. Clearly this adds significant computational expense to our simulation and, unless significant advancements in computing are made, requires us to find a more efficient method of approximating horizon locations. For more information on the numerical computation of event horizons, see [7], [15], and [24].

2.2.4 Apparent Horizons

As was discussed in the previous section, event horizons are not efficient to calculate. A commonly used alternative is the *apparent horizon*, which we will define and then explain in detail. An apparent horizon is the outermost smooth 2-surface embedded in the timelike hypersurface Σ whose outgoing future null geodesics have *zero expansion* everywhere [7]. To understand what this means, begin by considering a surface $S \subseteq \Sigma$ such that s^a is the outward pointing unit normal to Σ

$$s_a s^a = 1, \qquad s^a k_a = 0, \tag{2.78}$$

where k^a is the unit normal to $t = \text{const}$ spatial hypersurfaces. Consider the spatial metric

$$\gamma_{ab} = g_{ab} + k_a k_b, \tag{2.79}$$

which considers a timeslice where $dt = 0$. Now we can clearly write the metric in the form

$$g_{ab} = \gamma_{ab} - k_a k_b. \tag{2.80}$$

Then we can write a similarly defined 2-metric m_{ab} in the following way:

$$\begin{aligned} m_{ab} &= \gamma_{ab} - s_a s_b \qquad (2.81)\\ &= g_{ab} + k_a k_b - s_a s_b. \qquad (2.82) \end{aligned}$$

Now use this metric to construct outgoing and ingoing tangents (l^a and n^a respectively) to the future-pointing null geodesics that are linear combinations of k^a and s^a and are orthogonal to S:

$$l^a \equiv \frac{1}{\sqrt{2}}(k^a + s^a), \qquad n^a \equiv \frac{1}{\sqrt{2}}(k^a - s^a). \tag{2.83}$$

The 2-dimensional metric m_{ab} can be expressed in terms of these null geodesics:

$$m_{ab} = g_{ab} + l_a n_b + n_a l_b, \tag{2.84}$$

where the *expansion* Θ of these outgoing null geodesics is defined to be:

$$\Theta = m^{ab}\nabla_a l_b \tag{2.85}$$

and surfaces of zero expansion have $\Theta = 0$. A surface is known as an *outer trapped surface* (OTS) if for some $S \subseteq \Sigma$ the expansion Θ of outgoing null geodesics which are orthogonal to S is such that $\Theta \leq 0$ everywhere on the surface [7]. A region of Σ that contains trapped surfaces is a *trapped region.* A *marginally outer trapped surface* (MOTS) is an OTS with $\Theta = 0$ everywhere [7]. An apparent horizon is an example of an MOTS. This means that an apparent horizon is contained inside of, or is equivalent to, the event horizon $r = r_H$ of a black hole. This makes it a useful replacement for event horizons when doing numerical calculations.

Consider a metric of an arbitrary spacetime in spherical polar coordinates (BS):

$$ds^2 = -(\alpha^2 - A\beta^2)dt^2 + 2A^2\beta dr dt + A^2 dr^2 + B^2 r^2(d\theta^2 + \sin^2\theta d\phi^2), \tag{2.86}$$

where α is the lapse of the spacetime, β is the radial component of the shift vector β^i, and all four A, B, α, and β are functions only of r and t. Furthermore, A and B are chosen to define the spacetime we are interested in and, most importantly, r is the coordinate radius of our point of interest. When written in this form, the outgoing null normal is

$$l_a = \frac{1}{\sqrt{2}}(A\beta - \alpha, A, 0, 0), \qquad l^a = \frac{1}{\sqrt{2}}(\alpha^{-1}, A^{-1} - \alpha^{-1}\beta, 0, 0) \tag{2.87}$$

with the corresponding spatial 2-metric

$$m_{ab} = \mathrm{diag}(0, 0, B^2 r^2, B^2 r^2 \sin^2\theta), \tag{2.88}$$

of which we consider only the invertible portion, so our metric takes the form of a 2 × 2 diagonal matrix. We can then rewrite our expansion in terms of these quantities, although the derivation is omitted.

$$\Theta = \frac{\sqrt{2}}{rB}\left(\frac{1}{\alpha}\partial_t(Br) + \left(\frac{1}{A} - \frac{\beta}{\alpha}\right)\partial_r\left(Br\right)\right). \tag{2.89}$$

In this form, the areal radius $R = Br$. If we want its directional derivative along l^a we have:

$$\begin{aligned} l^a\nabla_a R &= l^t\nabla_t R + l^r\nabla_r R & (2.90)\\ &= \frac{1}{\sqrt{2}}\left(\alpha^{-1}\partial_t R + \left(A^{-1} - \alpha^{-1}\beta\right)\partial_r R\right), & (2.91)\end{aligned}$$

which means that the expansion is proportional to the change of the areal radius along the null normal vector l^a.

The expansion Θ can be used to extract physical parameters such as mass M and angular momentum J of the black hole when defined in terms of the areal radius of the horizon R:

$$\Theta = \frac{2}{R}l^a\nabla_a R = \frac{1}{4\pi R^2}l^a\nabla_a\left(4\pi R^2\right), \tag{2.92}$$

where $R = \left(\frac{\mathcal{A}}{4\pi}\right)^{1/2}$ and is based on the surface area $\mathcal{A}$ of a spherical surface. When defined this way, it becomes clear that Θ can be interpreted as the measurement of the change of the cross-sectional area of a bundle of outgoing null rays. Practically, this tells us whether an outward pointing spherical flash of light moves immediately outward. If that is the case, it has been emitted outside of an apparent horizon.

Consider the evolution of a spacetime in which the apparent horizon of a black hole is being calculated at each timestep. This will result in a sequence of apparent horizons on neighboring spatial slices such that $S \subseteq \Sigma$ where apparent horizons move discretely to neighboring slices. The *world tube* H, or path of this object through spacetime, is discontinuous, whereas the worldtube for an event horizon moving through spacetime is continuous as in Figure 2.2 from [7].

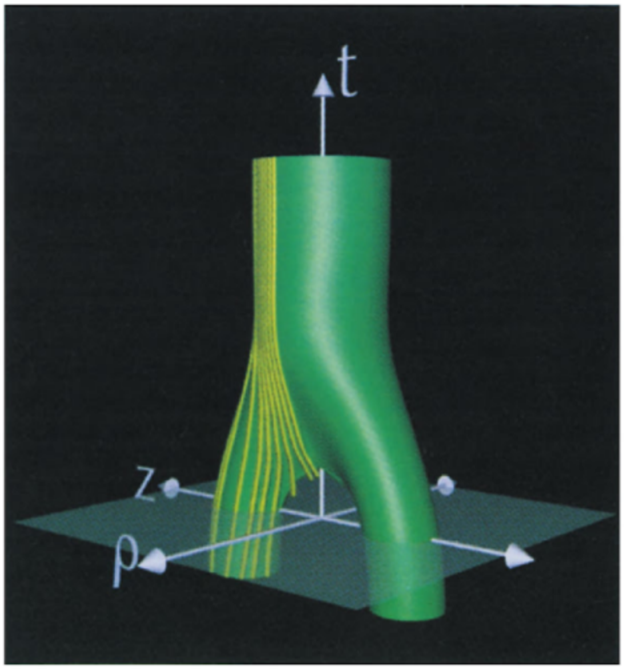

Figure 2.2: The *world tube* formed by the merging of the event horizons of two black holes. If we take planar spatial slices in the $x - y$ direction, and time moving in the $z-$direction there are clearly two black holes merging. However, spacetime can be sliced in such a way that we see one black hole [7], which is shown by the yellow slices.

If instead one were to calculate the event horizon of a black hole, the worldtube would be smooth for all time. In Figure 2.2, spatial slices of the event horizons of two merging black holes are calculated for all time and stacked to create a continuous, smooth world tube. The apparent horizons of black holes only form smooth H if they coincide with the black holes' event horizons and thus would be nonexpanding, null surfaces. However, if H is spacelike, we know that the apparent horizons are expanding and there exists a dynamical horizon. These dynamical horizons are precisely what we are most interested in calculating with efficiency as they are, practically, the most challenging to implement. Several techniques have been proposed to deal with such dynamic spacetimes. In the following section, we will discuss the method most relevant to the results presented in this thesis.

2.3 Isolated and Dynamical Horizons

Using isolated and dynamical horizons when evolving dynamic spacetimes is advantageous in several important respects. First, it is a quasi-local approach, which means it does not require global knowledge of the spacetime. This allows isolated horizons to provide insight into the evolution of the spacetime without being as computationally expensive as the explicit calculation of an event horizon. Isolated and dynamical formalism also allows us to gain some physical insight into the black holes present in the spacetime [7]. We can implement isolated and dynamical horizons to determine changes in mass ΔM and angular momentum ΔJ during evolution.

The approach most commonly used in GR considers a spacetime metric of form $(-,+,+,+)$ with scaling such that $G = c = 1$. Consider a unique outward pointing spacelike normal s^a tangent to some surface $S \subseteq \Sigma$, and also the two null vectors l^a and n^a but now impose the condition that

$$l \cdot n = -1. \tag{2.93}$$

Now take two orthonormal vectors e_1 and e_2 which are tangent to S. Construct a complex null vector

$$m = \frac{1}{\sqrt{2}} \left(e_1 + ie_2\right) \tag{2.94}$$

that satisfies

$$m \cdot m = 0, \qquad m \cdot \bar{m} = 1, \qquad l \cdot m = 0, \qquad n \cdot m = 0. \tag{2.95}$$

Then the four vectors $(l, n, m, \bar{m})$ form a null tetrad of four linearly independent, orthogonal vectors tangent to S. Expansions in the l and n directions (outward and inward) are defined as in Section 2.2.4:

$$\Theta = \Theta_{(l)} = m^{ab} \nabla_a l_b, \tag{2.96}$$

$$\Theta_{(n)} = m^{ab} \nabla_a n_b, \tag{2.97}$$

with an apparent horizon being the outermost MOTS such that

$$\Theta_{(l)} = 0, \tag{2.98}$$

$$\Theta_{(n)} < 0. \tag{2.99}$$

The apparent horizon world tube H is created by stacking these spatial slices S on top of each other at different timesteps. If H is smooth, the apparent horizon is either null or spacelike; if not, it is null and nonexpanding. An apparent horizon is null at late times in the evolution of a binary black hole merger, after the final horizon has taken shape and settled down. Then m_{ab} is viewed as a degenerate 3-metric on a null surface H. Isolated horizons are used when an apparent horizon S is non-expanding, which happens when the following conditions are satisfied:

- S is null and $S^2 \times \mathbb{R}$.
- $\Theta = 0$ on S.
- The equations of motion hold on S.

The world tube of an approximately isolated black hole can be modeled using non-expanding horizons (NEH), but the results are not exact. An apparent horizon is the *outermost* MOTS whereas an NEH may not have this property depending on spacetime slicing. Furthermore, the condition $\Theta_{(n)} < 0$ may not be satisfied by an isolated horizon. Although usually this is not the case, there do exist physical scenarios in which $\Theta_{(n)} = 0$.

NEH allows us to have insight into late-time behavior of the apparent horizons of black holes. In order to use this technique, however, one must be able to accurately locate apparent horizons on spatial slices Σ. This is done via the following questions:

- Is the world tube H a NEH?
- If yes, is the world tube H null?

To answer these questions, consider the metric m_{ab} on a single time slice. We will use the shear $\sigma^{(l)}_{ab}$ defined by

$$\sigma^{(l)}_{ab} = m^a m^b \nabla_a l_b, \tag{2.100}$$

where m^a and l^a are two of the four orthonormal tetrad vectors. It must be true that H is a NEH if and only if $\sigma^{(l)}_{ab} \equiv 0$ at all points of H. Note that we care about this equality only up to expected numerical errors in the computation. The knowledge that H is a NEH provides us with methods of extracting Killing vectors, and from those, quantities like ΔJ and ΔM, which provide insight into the spacetime evolution. Further discussion of isolated horizons and NEHs are beyond the scope of this thesis, however, so the reader is referred to [16] for further information. We use isolated horizons methodology to evolve the simulation outlined in Chapter 4, and we will discuss in further detail there the consequences of displaying apparent horizons using this technique [16].

2.3.1 Mean Curvature

One of the features of the black hole horizons we are particularly interested in is the mean curvature of the horizons themselves, as well as how this curvature changes throughout the evolution. The mean curvature κ of a surface is the trace of its *extrinsic curvature* K_{ab}. The extrinsic curvature is a spatial measurement of the gradient of normal vectors n^a which differ in direction. It encodes information regarding how much the direction of these vectors change across a spatial hypersurface Σ. The extrinsic curvature can be defined in terms of the spatial metric γ_{ab}:

$$K_{ab} = -{\gamma_a}^c {\gamma_b}^d \nabla_c n_d. \tag{2.101}$$

To measure the extrinsic curvature of a spacetime instead of the extrinsic curvature of a surface, we use vectors normal to the spacetime rather than a specific hypersurface Σ in a spatial slice. We will consider only extrinsic (and mean) curvature of a surface. The trace of the extrinsic curvature is the *mean curvature*

$$\kappa = g^{ab} K_{ab} = \gamma^{ab} K_{ab}, \tag{2.102}$$

whose negative calculates the change in the proper 3-volume along vectors n^a.

2.3.2 Flow Algorithms

Flow algorithms are used to find apparent horizons in spatial slices during a spacetime evolution. They consider the evolution of a 2-surface under some pseudo-time λ which, in the $\lambda \to \infty$ limit of such a surface, converge to the apparent horizons of black holes in a spacetime. The convergence of these algorithms is independent of the initial guess of the apparent horizon's location. This means that a guess very close to the horizon and one far away converge in the same amount of time, so there is no benefit to knowing the approximate location of an apparent horizon in a spatial slice [28].

A subset of apparent-horizon-finding algorithms use either mean curvature κ or expansion flow Θ methods to compute approximate apparent horizon locations during spacetime evolution. Tod [29] considered first the time symmetric case where $K_{ab} = 0$ in a spatial slice of a spacetime and found that since an MOTS is a minimum area surface it can be found by solving the parabolic partial differential equation

$$\partial_\lambda x^a = -\kappa s^a, \tag{2.103}$$

where s^a is the outward-pointing unit normal to the surface $S \subseteq \Sigma$ and x^a are the spatial coordinates of the surface point (which we are looking for). It has been shown formally that sending the pseudo-time parameter $\lambda \to \infty$ will allow us to find a minimum area surface within a spatial slice if such a surface exists. We have also made the assumption that the RHS of Equation (2.103) is known and the following equations hold:

$$s_a s^a = 1, \qquad s^a n_a = 0, \tag{2.104}$$

where n^a is the unit normal to Σ. It is also worth investigating how one finds the unit normal s^a to the surface S where S is not exactly spherical. This is done via [7]:

$$s^a = \lambda D^a \tau, \tag{2.105}$$

$$s_a = \lambda D_a \tau = \lambda \partial_a \tau, \tag{2.106}$$

where $\lambda = (\gamma^{ab} D_a \tau D_b \tau)^{-1/2}$, τ denotes units of proper time, and $D_a f = \gamma_a{}^b \nabla_b f$ for some scalar function f. This method, which works in the time symmetric case, is guaranteed to converge to an outermost MOTS as $\lambda \to \infty$.

Since the aforementioned method of finding an apparent horizon works only when we have $K_{ab} = 0$, we need some generalization of this algorithm which works for $K_{ab} \neq 0$. The following *expansion flow* algorithm uses Θ in place of κ so:

$$\partial_\lambda x^a = -\Theta s^a. \tag{2.107}$$

The $\lambda \to \infty$ convergence to an apparent horizon has not been proven rigorously for this method, but it is expected that the expansion flow is equivalent to the mean curvature flow at the apparent horizon. Numerical experiments have confirmed the convergence to an apparent horizon despite the non existence of a formal proof. Furthermore, improvements to the speed of convergence have also been made; replacing

$$\Theta \equiv \left[(\Theta - c)\arctan^2\left(\frac{\Theta - c}{\Theta_0}\right)\right], \tag{2.108}$$

which takes the initial guess for the horizon location Θ_0 and sets a goal value for the expansion $c \to 0$ as the number of iterations of the algorithm head to infinity. This method forces the surface to shrink at a faster rate farther from the horizon, thus reducing the number of unhelpful iterations of the algorithm.

The most common expansion flow algorithm is AHFinderDirect, which is available open-source through Einstein ToolKit. The reader is directed to the AHFinderDirect documentation[1] and [27] for more information.

Multiple Horizons

These algorithms seem to work well for spatial slices with one apparent horizon present, but most simulations are done of binary black hole (BBH) systems. A natural question is whether or not these algorithms can still be applied. In fact, they can be. If we start with one 2-sphere as our inital guess, as the algorithm progresses towards the apparent horizons, bifurcation will occur at some point closer to the horizons. This can be rather computationally expensive, but current algorithms are able to handle this with relative efficiency. Convergence is guaranteed to the outermost MOTS in a time slice for time-symmetric ($K_{ab} = 0$) cases only, and even then it is slow. Attempting to speed up convergence may result in the missing of apparent horizons in time slices and therefore eliminating the convergence guarantee. Once again, the reader is referred to AHFinderDirect documentation[2] for further information, as providing the methodologies with which convergence to a system of apparent horizons is achieved is beyond the scope of this thesis.

---

[1] https://einsteintoolkit.org/thornguide/EinsteinAnalysis/AHFinderDirect/documentation.html

[2] https://einsteintoolkit.org/thornguide/EinsteinAnalysis/AHFinderDirect/documentation.html

Chapter 3

Radiation

Gravitational radiation propagates through spacetime at the speed of light in the form of gravitational waves. These perturbations of spacetime geometry are predictions of general relativity and were successfully detected by LIGO in 2015. They are particularly important to numerical relativists; gravitational waves are associated with the presence of dynamic gravitational fields and carry significant quantities of energy and momentum away from a sufficiently massive binary system [3]. In this thesis, we choose to study the extraction of gravitational wave information using Newman Penrose Formalism, which takes the Weyl tensor with respect to a frame of null vectors. The alternative would be to use perturbations of a Schwarzschild spacetime. However, it is becoming increasingly more common (and more accurate) to extract gravitational wave data using the former method, so this is what we choose to study.

3.1 3+1 Decomposition of a Spacetime

Before we discuss gravitational wave extraction and radiation in detail, it is appropriate to briefly mention the 3+1 decomposition of a spacetime. The standard practice in Numerical Relativity is to use the 3+1 formation (also known as ADM) of the Einstein equations for numerical evolution. To evolve a spacetime, we are effectively solving a PDE initial value problem. There are robust techniques to solve such problems, provided the correct initial conditions are given. The evolution of a spacetime is determined by g_{ab} and $\partial_t g_{ab}$ at some initial time t_0. The second time derivative of the metric $\partial_t^2 g_{ab}$ is also necessary and can be determined from the Einstein Field Equations, but it is nontrivial to do so since four of the ten components have no second time derivative.

The equations in 3+1 formalism are equivalent to the standard equations of General Relativity. Writing the EFEs in 3+1 formalism allows us to overcome this hurdle by evolving 12 purely spatial quantities and forcing them to satisfy specific constraints on particular time slices (spatial hypersurfaces at an instant of time t). The development of the 3+1 formalism is motivated by the necessity of a numerical solution for the GR equations since analytic solutions are unobtainable. Since extensive documentation of 3+1 NR methodologies is available, we will go no further here than to say that these ADM equations are what were evolved to obtain the simulation of GW150914 used for this thesis. For more information, the reader is referred to [3] and [7].

3.2 Gravitational Radiation h

Before we begin our discussion on Newman Penrose formalism, we will first briefly mention the perturbative quantity h as it is relevant to us. Define the metric g_{ab} as

$$g_{ab} = \eta_{ab} + h_{ab}, \qquad |h_{ab}| \ll 1, \tag{3.1}$$

so that the radiative spacetime is defined by small perturbations given by h_{ab} on the Minkowski (flat space) metric η_{ab}. This perturbation is what is detected by LIGO when a gravitational wave source is observed. It is convenient to use a different formulation of this perturbation, called the trace-reversed perturbation which is defined by

$$\bar{h}_{ab} = h_{ab} + \frac{1}{2} h^c{}_c \eta_{ab}, \tag{3.2}$$

where $\bar{h}^a{}_a = -h^a{}_a$ (hence the name trace-reversed), with the harmonic gauge condition governing the propagation of waves in vacuum:

$$\Box \bar{h}_{ab} \equiv \nabla^c \nabla_c \bar{h}_{ab} = 0. \tag{3.3}$$

In a non-vacuum spacetime,

$$\Box \bar{h}_{ab} = -16\pi T_{ab} \tag{3.4}$$

for a weak-field, slow velocity source.

One can derive from the quantity h_{ab} two dimensionless amplitudes h_+ and $h_\times$ associated with the two polarizations of a linearized gravitational wave. Figure 3.1 from [7] is an illustration of what both h_+ and $h_\times$ represent physically:

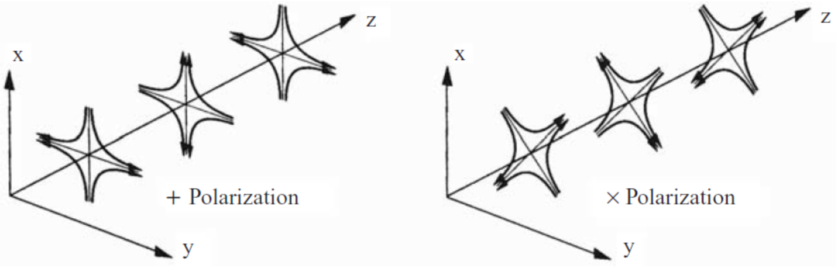

Figure 3.1: The polarizations h_+ and $h_\times$ of a plane gravitational wave emitted in the $z-$direction [7].

Using h_+ and $h_\times$, we can construct the *transverse-traceless* (TT) gauge which takes the form

$$h_{jk}^{TT} = h_+ e_{ij}^+ + h_\times e_{ij}^\times \tag{3.5}$$

for $e_{xx}^+ = -e_{yy}^+ = e_{xy}^\times = e_{yx}^\times = 1$, otherwise $e_{ij} = 0$ for all other values of i, j. The TT gauge is important since it provides a direct measurement of the Riemann tensor in the following way

$$R_{i0j0} = -\frac{1}{2}\ddot{h}_{ij}^{TT}. \tag{3.6}$$

We will discuss metric perturbations h_{ab} no further than this, but will instead refer the reader to [7] and dedicate the rest of this chapter to the construction of both tetrad and Newman Penrose formalisms.

3.3 Tetrad Formalism

In this section we will provide the reader with a necessary overview of tetrad formalism, Newman Penrose formalism, and tetrad properties that will be useful when discussing how we use numerical relativity to extract gravitational wave data. Our notes come from [3], [7], [13], and [14].

3.3.1 Tetrad Basis Vectors

We define a tetrad to be a set of four linearly independent basis vectors

$$\{\vec{e}_{\ a}\} \tag{3.7}$$

such that a ranges from $1, ..., n$ where n is the dimensionality of our spacetime ($n = 4$ for physical space) and identifies a vector. We also require that

$$\vec{e}_{\ a} \cdot \vec{e}_{\ b} = \eta_{ab} \tag{3.8}$$

for some constant, nonsingular matrix η_{ab} dependent only on our choice of tetrad vectors (i.e., independent of our coordinates or position). Consider η_{ab} to be our metric, so its inverse is denoted η^{ab} with

$$\eta^{ac}\eta_{cb} = \delta^a_b \tag{3.9}$$

for Kroenecker-delta δ. We can use this to define a set of vectors $\{\vec{e}^{\ a}\}$ orthogonal to Equation (3.7) as follows

$$\vec{e}^{\ a} = \eta^{ab}\vec{e}_{\ a} \tag{3.10}$$

$$\vec{e}^{\ a} \cdot \vec{e}_{\ b} = \eta^{ab}\vec{e}_{\ a} \cdot \vec{e}_{\ b} \tag{3.11}$$

$$\vec{e}^{\ a} \cdot \vec{e}_{\ b} = \eta^{ab}\eta_{ab} \tag{3.12}$$

$$\vec{e}^{\ a} \cdot \vec{e}_{\ b} = \delta^a_b \tag{3.13}$$

It would also be convenient to be able to express the tetrad vectors in terms of the coordinate basis and in fact we can. Using an arbitrary vector $\vec{v}$ where

$$\vec{v} = v^a\vec{e}_{\ a} = v_a\vec{e}^{\ a} \tag{3.14}$$

and

$$v^a = \vec{v} \cdot \vec{e}^{\ a} \tag{3.15}$$

$$v_a = \vec{v} \cdot \vec{e}_{\ a} \tag{3.16}$$

such that the indices on vector $\vec{v}$ indicate components of the vector, we can clearly compute the dot product of two vectors

$$\vec{v} \cdot \vec{u} = v^a \vec{e}_{\ a} u^a \vec{e}_{\ a} \tag{3.17}$$

$$= v^a \vec{e}_{\ a} u_a \vec{e}^{\ a} \tag{3.18}$$

$$= v^a u_a, \tag{3.19}$$

which is valid since a and μ are just dummy indices. We expect, now, that we can straightforwardly construct a formulation of the tetrad basis in terms of coordinates. This will later allow us to express a coordinate metric in terms of the coordinate-independent tetrad basis. Going forward, Latin indices denote individual vectors and Greek indices denote components. Directly substituting Equation (3.15) into Equation (3.14) gives

$$\vec{v} = v^a \vec{e}_{\ a} \tag{3.20}$$

$$= (\vec{v} \cdot \vec{e}^{\ a}) \vec{e}_{\ a}. \tag{3.21}$$

If we let $\vec{u} = \vec{e}^{\ a}$ in Equation (3.19), we can rewrite:

$$\vec{v} = (\vec{v} \cdot \vec{e}^{\ a})\ \vec{e}_{\ a} \tag{3.22}$$

$$= (v^{\ \mu}\ e^{\ a}_{\ \mu})\ (e^{\ \nu}_{\ a} \vec{e}_{\ \nu}). \tag{3.23}$$

We now have all necessary material to show it is possible to derive the metric components $g_{\mu\nu}$ in terms of the tetrad vectors. To begin the proof, we note the following:

$$g_{\mu\nu} = e_{a\mu}\ e^{\ a}_{\ \nu} \tag{3.24}$$

with

$$\vec{e}^{\ a} = e_{\nu}^{\ a} \vec{e}^{\ \nu}, \tag{3.25}$$

$$\vec{e}^{\ a} \vec{e}_{\ \nu} = e_{\nu}^{\ a} \tag{3.26}$$

and

$$\vec{e}_{\ a} = e_{a\mu} \vec{e}^{\ \mu},$$

$$\vec{e}_{\ a}\vec{e}_{\ \mu} = e_{a\mu}, \tag{3.27}$$

which can both be substituted into Equation (3.24) and then used in conjunction with Equation (3.10) as follows:

$$g_{\mu\nu} = e_{a\mu}\ e^{\ a}_{\ \nu} \tag{3.28}$$

$$= \vec{e}_{\ a}\vec{e}_{\ \mu}\vec{e}^{\ a}\vec{e}_{\ \nu} \tag{3.29}$$

$$= \vec{e}_{\ a}\vec{e}_{\ \mu}\eta^{ab}\vec{e}_{\ b}\vec{e}_{\ \nu}. \tag{3.30}$$

Now, using Equation (3.27), we can write

$$g_{\mu\nu} = e_{a\mu}\eta^{ab}e_{b\nu},$$

$$g_{\mu\nu} = \eta^{ab}e_{a\mu}e_{b\nu}, \tag{3.31}$$

and so we have a way to transform our metric $g_{\mu\nu}$ from a coordinate basis to a tetrad basis.

3.3.2 Ricci Rotation Coefficients

Consider an arbitrary vector $\vec{v} = v^a\vec{e}_{\ a}$. The tetrad components of $\vec{v}$ are just scalar functions, so the directional derivative of $\vec{v}$:

$$v_{a;b} = e^{\mu}_{\ b}\nabla_{\mu}v_a. \tag{3.32}$$

We can replace $v_a = e^{\nu}_{\ a}v_{\nu}$ and expand the covariant derivative to obtain the following construction of the directional derivative from which we can define the *Ricci Rotation Coefficients*, which are connection coefficients for a tetrad basis:

$$v_{a;b} = e_{\ a}^{\ \nu}e_{\ b}^{\ \mu}\nabla_{\mu}v_{\nu} + e_{\ b}^{\ \mu}e_{\ c}^{\ \nu}v^c\nabla_{\mu}e_{a\nu}, \tag{3.33}$$

which we define to be

$$\gamma_{abc} = e_{\ a}^{\ \mu}e_{\ c}^{\ \nu}\nabla_{\nu}e_{b\mu} \tag{3.34}$$

such that $e_{\alpha}^{\ \mu} = e^{\mu}_{\ \alpha}$. Then replacement into Equation (3.33) gives an expression similar to that of the covariant derivative for scalar functions:

$$v_{a;b} = e_{\ a}^{\ \nu}e_{\ b}^{\ \mu}\nabla_{\mu}v_{\nu} + \gamma_{abc}v^c. \tag{3.35}$$

We can say that Ricci Rotation Coefficients are antisymmetric over their first two indices, and, in fact, we can show it quite simply.

Lemma 1. *Given* $e_a^{\ \nu} \cdot e_{b\ \nu} = \eta_{ab}$ *where* η_{ab} *constant, we have*

$$\nabla_\mu (e_{\ a}^{\ \nu} e_{b\nu}) = 0. \tag{3.36}$$

From this we can show that the Ricci rotation coefficients are antisymmetric in their first two indices.

Proof. Since η_{ab} is constant, we have $\nabla_\mu (e_{\ a}^{\ \nu} e_{b\nu}) = 0$. From here, we have:

$$\nabla_\mu (e_{\ a}^{\ \nu} e_{b\nu}) = 0 \tag{3.37}$$

$$e_{\ a}^{\ \nu} \nabla_\mu (e_{b\nu}) + e_{b\nu} \nabla_\mu (e_{\ a}^{\ \nu}) = 0 \tag{3.38}$$

$$e_{\ a}^{\ \nu} \nabla_\mu (e_{b\nu}) = -e_{b\nu} \nabla_\mu (e_{\ a}^{\ \nu}) \tag{3.39}$$

$$e_{\ a}^{\ \nu} e_{\ c}^{\ \mu} \nabla_\mu (e_{b\nu}) = -e_{b\nu} e_{\ c}^{\ \mu} \nabla_\mu (e_{\ a}^{\ \nu}) \tag{3.40}$$

$$\gamma_{abc} = -\gamma_{bac}. \tag{3.41}$$

□

Then there are 24 independent γ for a 4-dimensional spacetime, as opposed to 40 independent connection coefficients. We will see in the following section that Ricci Rotation Coefficients have specific geometric interpretations in Newman-Penrose formalism.

3.4 Newman-Penrose Formalism

Using [3], [7], [13], and briefly [14], we will outline Newman Penrose Formalism as it pertains to gravitational wave extraction and determination of the Weyl Scalars. Newman Penrose Formalism is useful in particular when studying algebraically special gravitational fields. It is advantageous in several respects; all differential equations that arise are of first order, Gauge transformations simplify the field equations into a useful form, and finally we are not working in coordinates and thus can more effectively extract invariant properties of a gravitational field. In Newman Penrose formalism, we choose to use null basis vectors as opposed to orthonormal basis vectors. The light cone structure of a spacetime in a null basis allows for the eventual introduction of a spinor basis [13]. Newman Penrose is particularly adaptable to the spacetimes from which black hole solutions of General Relativity derive, namely, Type D spacetimes, which we will discuss in depth in the coming sections.

3.4.1 Null Tetrads

We will begin by discussing an arbitrary null tetrad's properties, construction, and constraints. In the following sections, we will further refine the requirements our tetrad must satisfy to be useful. Furthermore, notation in the following sections is nonstandard (since no standardized notation exists) and draws from that of [3], [7] and [13].

Once again, consider the orthonormal tetrad $\{\vec{e}_{\ a}\}$ such that our matrix $\eta_{\mu\nu}$ corresponds to the flat space (Minkowski) matrix

$$\eta_{\mu\nu} = \begin{bmatrix} -1 & 0 & 0 & 0 \\ 0 & 1 & 0 & 0 \\ 0 & 0 & 1 & 0 \\ 0 & 0 & 0 & 1 \end{bmatrix}. \tag{3.42}$$

Now let our tetrad vector $\{\vec{e}_{\ a}\}$ be of dimension four and defined with unit timelike $e_0^\mu \equiv e_n^\mu$ normal to the surface, unit radial $e_1^\mu \equiv e_r^\mu$, and angular vectors $e_2^\mu \equiv e_\theta^\mu$ and $e_3^\mu \equiv e_\phi^\mu$.

Since we are working in a coordinate basis, the vectors e_θ^μ and e_ϕ^μ are not necessarily unit vectors, nor do we expect them to be orthogonal to each other or to the unit radial vector e_r^μ. We must orthogonalize via Gram-Schmidt Orthogonalization and allow for complex vectors to exist and scale them so that the vectors we construct meet our requirement of unit size. Once we have an orthonormal basis, we can write the metric as

$$g_{\mu\nu} = -e_{n\mu}e_{n\nu} + e_{r\mu}e_{r\nu} + e_{\theta\mu}e_{\theta\nu} + e_{\phi\mu}e_{\phi\nu}. \tag{3.43}$$

by substituting our basis into Equation (3.31). To understand why e_θ^μ and e_ϕ^μ are not necessarily orthogonal or unit-size, consider the Minkowski metric in polar coordinates:

$$g_{\mu\nu} = -dt^2 + dr^2 + r^2 d\theta^2 + r^2 \sin^2\theta d\phi^2. \tag{3.44}$$

Then

$$\begin{aligned}
e_{n\mu} e_{n\nu} &= dt^2 &(3.45)\\
e_{r\mu} e_{r\nu} &= dr^2 &(3.46)\\
e_{\theta\mu} e_{\theta\nu} &= r^2 d\theta^2 &(3.47)\\
e_{\phi\mu} e_{\phi\nu} &= r^2 \sin^2\theta d\phi^2. &(3.48)
\end{aligned}$$

When written in this form, it becomes clear that e_θ^μ and e_ϕ^μ are not orthogonal or unit size even in flat space for $r > 1$ and $r \sin\theta > 1$, and so must be both normalized and orthogonalized. In standard form, our null tetrad is written as two real-valued null vectors l^μ (outgoing) and k^μ (ingoing) and a complex valued null vectors m^μ defined as follows:

$$\begin{aligned}
l^\mu &= \frac{1}{\sqrt{2}} \left(e_n^\mu + e_r^\mu\right), &(3.49)\\
k^\mu &= \frac{1}{\sqrt{2}} \left(e_n^\mu - e_r^\mu\right), &(3.50)\\
m^\mu &= \frac{1}{\sqrt{2}} \left(e_\theta^\mu + i e_\phi^\mu\right), &(3.51)\\
\overline{m}^\mu &= \frac{1}{\sqrt{2}} \left(e_\theta^\mu - i e_\phi^\mu\right). &(3.52)
\end{aligned}$$

Where the flat space metric takes the form:

$$\eta_{\mu\nu} = \eta^{\mu\nu} = \begin{bmatrix} 0 & -1 & 0 & 0 \\ -1 & 0 & 0 & 0 \\ 0 & 0 & 0 & 1 \\ 0 & 0 & 1 & 0 \end{bmatrix}. \tag{3.53}$$

Which means that the corresponding covariant must be

$$e^n = e_r = l, \qquad e^r = e_n = k, \qquad e^\theta = -e_\phi = -\bar{m}, \qquad e^\phi = -e_\theta = -m, \tag{3.54}$$

where vectors with up indices are covariant and low indices are contravariant. When we say $e^n = e_r$, it means that since our vectors are of unit size, we construct them such that We must construct the above vectors such that the following conditions hold:

- The following orthogonality conditions must hold:
$$l \cdot m = l \cdot \bar{m} = m \cdot m = k \cdot \bar{m} = 0. \tag{3.55}$$
- The requirements of null vectors must be satisfied:
$$l \cdot l = k \cdot k = m \cdot m = \bar{m} \cdot \bar{m} = 0. \tag{3.56}$$
- The only non-vanishing inner products between any two are
$$l^\mu k_\mu = -1 = -m^\mu \overline{m}_\mu, \tag{3.57}$$
which we call our normalization condition.

The normalization condition is not an explicit requirement; it can be ignored to gain more freedom in choice of basis vectors, but that is not always practically advantageous. If we do this, two important aspects of the spacetime are lost:

- There is no antisymmetry in the first two indices of the Ricci rotation coefficients:
$$\gamma_{abc} \neq -\gamma_{bac}. \tag{3.58}$$
- There no longer exists the ability to permute the raising and lowering of tetrad indices when differentiating.

The explicit choice is then made to utilize the normalization condition for the tetrad basis vectors. Then the matrix η_{ab} becomes:
$$\eta_{ab} = \begin{bmatrix} 0 & -1 & 0 & 0 \\ -1 & 0 & 0 & 0 \\ 0 & 0 & 0 & 1 \\ 0 & 0 & 1 & 0 \end{bmatrix}, \tag{3.59}$$
which is its own inverse, and from which the metric $g_{\mu\nu}$ naturally follows:
$$g_{\mu\nu} = -l_\mu k_\nu - k_\mu l_\nu + m_\mu \overline{m}_\nu + \overline{m}_\mu m_\nu. \tag{3.60}$$

3.4.2 Spin Coefficients

In Section 3.1 we briefly touched upon Ricci Rotation coefficients and mentioned their usefulness as connection coefficients of the directional derivative of an arbitrary vector (see Equation (3.35)). The Ricci Rotation coefficients are also used to define *spin coefficients*, many of which have specific geometric interpretation within a tetrad basis. They can also be defined in terms of the equation

$$\nabla_b \vec{e}_{\ a} = \gamma^c{}_{ab} \vec{e}_{\ b}; \tag{3.61}$$

however, we will refer the reader to [14] for those definitions. We follow the structure of [3] here and define our 12 distinct spin coefficients as the following nonzero connection coefficients of the second term in Equation (3.35):

$$\kappa = \gamma_{\theta nn} = m^\mu D l_\mu, \tag{3.62}$$

$$\tau = \gamma_{\theta nr} = m^\mu \Delta l_\mu, \tag{3.63}$$

$$\sigma = \gamma_{\theta n\theta} = m^\mu \delta l_\mu, \tag{3.64}$$

$$\rho = \gamma_{\theta n\phi} = m^\mu \overline{\delta} l_\mu, \tag{3.65}$$

$$\tau' = \gamma_{\phi rn} = \overline{m}^\mu D k_\mu = -\pi, \tag{3.66}$$

$$\kappa' = \gamma_{\phi rr} = \overline{m}^\mu \Delta k_\mu = -\nu, \tag{3.67}$$

$$\rho' = \gamma_{\phi r\theta} = \overline{m}^\mu \delta k_\mu = -\mu, \tag{3.68}$$

$$\sigma' = \gamma_{\phi r\phi} = \overline{m}^\mu \overline{\delta} k_\mu = -\lambda, \tag{3.69}$$

and

$$\epsilon = \frac{1}{2}(\gamma_{rnn} - \gamma_{\phi\theta n}) = \frac{1}{2}(k^\mu D l_\mu - \overline{m}^\mu D m_\mu), \tag{3.70}$$

$$\gamma = \frac{1}{2}(\gamma_{rnr} - \gamma_{\phi\theta r}) = \frac{1}{2}(k^\mu \Delta l_\mu - \overline{m}^\mu \Delta m_\mu), \tag{3.71}$$

$$\beta = \frac{1}{2}(\gamma_{rn\theta} - \gamma_{\phi\theta\theta}) = \frac{1}{2}(k^\mu \delta l_\mu - \overline{m}^\mu \delta m_\mu), \tag{3.72}$$

$$\alpha = \frac{1}{2}(\gamma_{rn\phi} - \gamma_{\phi\theta\phi}) = \frac{1}{2}(k^\mu \overline{\delta} l_\mu - \overline{m}^\mu \overline{\delta} m_\mu). \tag{3.73}$$

Here the directional derivative operators are

$$D = l^\mu \nabla_\mu, \qquad \Delta = k^\mu \nabla_\mu, \qquad \delta = m^\mu \nabla_\mu, \qquad \overline{\delta} = \overline{m}^\mu \nabla_\mu. \tag{3.74}$$

We have chosen to let the subscripts of the γ_{abc} correspond to the basis vector subscripts for clarity. The covariant derivatives defined in Equation (3.74) will help us geometrically interpret the spin coefficients. Since we can express the derivative of a tetrad vector as a linear combination of all four tetrad vectors, we can expand any of them in terms of the tetrad to derive the Transport equations as follows:

$$Dl_\mu = l^\nu \nabla_\nu l_\mu = a l_\mu + b k_\mu + c m_\mu + d\overline{m}_\mu \tag{3.75}$$

for arbitrary complex coefficients a, b, c, and d. Now choose a, b, c, and d to maintain the linear independence of our four tetrad vectors while also forcing the equality to hold. For Dl_μ our result is specifically:

$$Dl_\mu = -(\epsilon + \overline{\epsilon}) l_\mu + \overline{\kappa} m_\mu + \kappa \overline{m}_\mu . \tag{3.76}$$

There are 16 of these Transport equations in total, which are called such because they define how the tetrad vectors are propagated through the spacetime, all with specific geometric interpretation. They are defined below for completeness, but we will not discuss them further.

$$\begin{aligned} Dl^\mu &= (\epsilon + \bar{\epsilon}) l^\mu - \bar{\kappa} m^\mu - \kappa \bar{m}^\mu \\ \Delta l^\mu &= (\gamma + \bar{\gamma}) l^\mu - \bar{\tau} m^\mu - \tau \bar{m}^\mu \\ \delta l^\mu &= (\bar{\alpha} + \beta) l^\mu - \bar{\rho} m^\mu - \sigma \bar{m}^\mu \end{aligned}$$

$$\begin{aligned} Dk^\mu &= -(\epsilon + \bar{\epsilon}) l^\mu + \pi m^\mu + \bar{\pi} \bar{m}^\mu \\ \Delta k^\mu &= -(\gamma + \bar{\gamma}) k^\mu + \nu m^\mu + \bar{\nu} \bar{m}^\mu \\ \delta k^\mu &= -(\bar{\alpha} + \beta) k^\mu + \mu k^\mu + \bar{\lambda} \bar{m}^\mu \\ \bar{\delta} k^\mu &= -(\alpha + \bar{\beta}) k^\mu + \lambda m^a + \bar{\mu} \bar{m}^a \end{aligned}$$

$$\begin{aligned} Dm^\mu &= \bar{\pi} l^\mu - \kappa k^\mu + (\epsilon - \bar{\epsilon}) m^\mu \\ \Delta m^\mu &= \bar{\nu} l^\mu - \tau k^\mu + (\gamma - \bar{\gamma}) m^\mu \\ \delta m^\mu &= \bar{\lambda} l^\mu - \sigma k^\mu + (\beta - \bar{\alpha}) m^\mu \end{aligned}$$

$$\bar{\delta} m^\mu = \bar{\mu} l^\mu - \rho k^\mu + (\alpha - \bar{\beta}) m^\mu$$

$$D\bar{m}^\mu = -(\epsilon - \bar{\epsilon})\bar{m}^\mu + \pi l^\mu - \bar{\kappa} k^\mu$$

$$\Delta\bar{m}^\mu = -(\gamma - \bar{\gamma})\bar{m}^\mu + \nu l^\mu - \bar{\tau} k^\mu$$

$$\delta\bar{m}^\mu = (\beta - \bar{\alpha})\bar{m}^\mu + \mu l^\mu - \bar{\rho} k^\mu$$

$$\delta\bar{m}^\mu = -(b\bar{e}ta - \alpha)\bar{m}^\mu + \lambda l^\mu - \bar{\sigma} k^\mu$$

3.4.3 Tetrad Transformations

The tetrad $(l^\mu, k^\mu, m^\mu, \bar{m}^\mu)$ can be transformed while still maintaining its orthonormality and the previously developed formalism. These transformations are characterized by Lorentz boosts and arbitrary spatial rotations, leaving us with six degrees of transformational freedom classified in the following way:

- Class I null rotations:

$$l^\mu \to l^\mu, \qquad m^\mu \to m^\mu + a l^\mu, \qquad \bar{m}^\mu \to \bar{m}^\mu + \bar{a} l^\mu, \qquad k^\mu \to k^\mu + \bar{a} m^\mu + a \bar{m}^\mu + a\bar{a} l^\mu \quad (3.77)$$

- Class II null rotations:

$$k^\mu \to k^\mu, \qquad m^\mu \to m^\mu + b k^\mu, \qquad \bar{m}^\mu \to \bar{m}^\mu + \bar{b} k^\mu, \qquad l^\mu \to l^\mu + \bar{b} m^\mu + b \bar{m}^\mu + b\bar{b} k^\mu \quad (3.78)$$

- Class III null rotations (spin-boost transformations):

$$l^\mu \to \lambda^{-1} l^\mu, \qquad k^\mu \to \lambda k^\mu, \qquad m^\mu \to e^{i\theta} m^\mu, \qquad \bar{m}^\mu \to e^{-i\theta} \bar{m}^\mu. \quad (3.79)$$

Here a, b are complex and λ, θ are real, θ is the angle of rotation, and $\lambda = [(1-v)/(1+v)]^{1/2}$ for boost speed v. Class III rotations are spin-boost transformations. This means that since the l^μ and k^μ tetrad vectors are scaled by real quantities λ and λ^{-1}, and are dependent only on vectors $\vec{e}_n$ and $\vec{e}_r$, there is a Lorentz boost in the $(\vec{e}_n, \vec{e}_r)$ plane, and v is the boost speed in the $\vec{e}_r$ direction. Since m^μ and $\bar{m}^\mu$ tetrad vectors are transformed by the rotation parameters $e^{i\theta}$ and $e^{-i\theta}$, respectively, clearly there is a rotation in the $(\vec{e}_\theta, \vec{e}_\phi)$ plane. We will discuss the usefulness of this classification further once the necessary formalism for the Weyl Tensor and Weyl Scalars has been developed.

3.5 Weyl Tensor and Weyl Scalars

Before moving into a discussion of spacetimes and gravitational waves, it is necessary to define the *Weyl Tensor* and resultant *Weyl Scalars.* The Weyl Tensor will be defined in the context of the Riemann Tensor and its symmetries. We will then use the previously developed Newman Penrose Formalism to define the Weyl Scalars, classify them and discuss how they are used in gravitational wave extraction.

3.5.1 Weyl Tensor

The n-dimensional Riemann Tensor $R^{\alpha}{}_{\beta\mu\nu}$ (2.28) has n^4 components without accounting for symmetries. The Ricci Tensor $R_{\mu\nu}$ is the trace of the Riemann Tensor, but for $n \leq 3$, they are equivalent. In dimensions $n \geq 4$, the Riemann Tensor has more independent components than the Ricci Tensor, and the Ricci Tensor constitutes only the trace portion of the Riemann Tensor. The remaining components (in $n = 4$) make up the Weyl Tensor. Table 3.1 gives the number of independent components of each tensor.

Dimensions	Weyl Tensor	Ricci Tensor	Riemann Tensor
n	$\frac{n(n+1)(n+2)(n-3)}{12}$	$\frac{n(n+1)}{2}$	$\frac{n^2(n^2-1)}{12}$
2	undefined	1	1
3	undefined	6	6
4	10	10	20

Table 3.1: Components of the Weyl, Ricci, and Riemann Tensors in $n = 2, 3,$ and 4 dimensions.

The Weyl Tensor is defined below for a space of arbitrary dimension; however, we will only consider the physical case of $n = 4$:

$$C_{\alpha\beta\mu\nu} = R_{\alpha\beta\mu\nu} - \frac{2}{n-2}[g_{\alpha[\mu}R_{\nu]\beta} - g_{\beta[\mu}R_{\nu]\alpha}] + \frac{2}{(n-1)(n-2)}g_{\alpha[\mu}g_{\nu]\beta}R. \tag{3.80}$$

The Weyl Tensor has several useful properties.

1. Since it is composed of the trace-free components of the Riemann Tensor, it is clearly traceless (i.e. $C^{\alpha}_{\ \mu\alpha\nu} = 0$).
2. It is divergenceless in vacuum [3].
3. Under any conformal transformation $\tilde{g}_{\mu\nu} = \Omega g_{\mu\nu}$, the Weyl Tensor stays the same: $\tilde{C}^{\alpha}_{\ \beta\mu\nu} = C^{\alpha}_{\ \beta\mu\nu}$; thus, it is sometimes dubbed the *conformal curvature tensor*. The same cannot be said for the Riemann Tensor outside of vacuum spacetime.
4. It maintains the symmetries of the Riemann Tensor:

$$C_{\alpha\beta\mu\nu} = C_{[\alpha\beta][\mu\nu]}, \tag{3.81}$$

$$C_{\alpha\beta\mu\nu} = C_{\mu\nu\alpha\beta}, \tag{3.82}$$

$$C_{\alpha[\beta\mu\nu]} = 0. \tag{3.83}$$

5. In $n < 4$ dimensions it vanishes identically.
6. If and only if $g_{\mu\nu}$ is conformally flat does the Weyl tensor vanish.

The following definitions are introduced entirely for completeness; we will not discuss their derivations, nor will we explain them further as they are not necessary for the conclusions of this thesis.

The Bianchi Identities can be written in terms of the Weyl Tensor as below:

$$\nabla_{\alpha} C^{\alpha}_{\ \beta\mu\nu} = \nabla_{[\mu} R_{\nu]\beta} + \frac{1}{6} g_{\beta[\mu} \nabla_{\nu]} R, \tag{3.84}$$

as can the Einstein Field Equations:

$$\nabla_{\alpha} C^{\alpha}_{\ \beta\mu\nu} = 8\pi \left[\nabla_{[\mu} T_{\nu]\beta} + \frac{1}{3} g_{\beta[\mu} \nabla_{\nu]} T \right] \tag{3.85}$$

for stress energy tensor $T_{\mu\nu}$. The *dual* of the Weyl Tensor $C^{*}_{\alpha\beta\mu\nu}$can be used to construct the electric $E_{\mu\nu}$ and magnetic $B_{\mu\nu}$ components. The left dual and right dual are equivalent, so we arbitrarily choose to use the left dual:

$$C^{*}_{\alpha\beta\mu\nu} = \frac{1}{2} C_{\alpha\beta\mu\nu} \epsilon^{\lambda\sigma}_{\ \ \ \mu\nu} \tag{3.86}$$

where the *Levi-Civita Tensor* $\epsilon_{\alpha\beta\mu\nu}$ is defined as [3]

$$\epsilon_{\alpha\beta\mu\nu} = \begin{cases} |g|^{1/2} & \text{for even permutations of the indices} \\ -|g|^{1/2} & \text{for odd permutations of the indices} \\ 0 & \text{for repeated indices.} \end{cases} \tag{3.87}$$

The double dual is defined as

$$C^{**}_{\alpha\beta\mu\nu} = -C_{\alpha\beta\mu\nu}, \tag{3.88}$$

Then, for arbitrary unit timelike vector n^μ

$$E_{\mu\nu} = n^\alpha n^\beta C_{\alpha\beta\mu\nu}, \tag{3.89}$$

$$B_{\mu\nu} = n^\alpha n^\beta C^{*}_{\alpha\beta\mu\nu} \tag{3.90}$$

are the electric and magnetic components of the Weyl tensor, respectively. We expect to be able to express $C_{\alpha\beta\mu\nu}$ entirely in terms of $E_{\mu\nu}$ and $B_{\mu\nu}$, and in fact we can:

$$C_{\alpha\beta\mu\nu} = 2\left[l_{\alpha[\mu}E_{\nu]\beta} - l_{\beta[\mu}E_{\nu]\alpha} - n_{[\mu}B_{\nu]\lambda}\epsilon^{\lambda}_{\alpha\beta} - n_{[\alpha}B_{\beta]\lambda}\epsilon^{\lambda}_{\mu\nu}\right] \tag{3.91}$$

for

$$l_{\mu\nu} = g_{\mu\nu} + 2n_\mu n_\nu. \tag{3.92}$$

The ten independent components of the Weyl tensor are most useful to us when decomposed into the five complex Weyl scalars.

3.5.2 Weyl Scalars

The five complex Weyl scalars make up the ten independent components of the Weyl tensor. They are defined below in terms of the arbitrary tetrad $(l^\mu, k^\mu, m^\mu, \bar{m}^\mu)$

$$\Psi_0 = C_{\alpha\beta\mu\nu} l^\alpha m^\beta l^\mu m^\nu \tag{3.93}$$

$$\Psi_1 = C_{\alpha\beta\mu\nu} l^\alpha k^\beta l^\mu m^\nu \tag{3.94}$$

$$\Psi_2 = C_{\alpha\beta\mu\nu} l^\alpha m^\beta \bar{m}^\mu k^\nu \tag{3.95}$$

$$\Psi_3 = C_{\alpha\beta\mu\nu} l^\alpha k^\beta \bar{m}^\mu k^\nu \tag{3.96}$$

$$\Psi_4 = C_{\alpha\beta\mu\nu} k^\alpha \bar{m}^\beta k^\mu \bar{m}^\nu \tag{3.97}$$

Any other contraction of the four tetrad vectors with the Weyl tensor can be specified in terms of these five scalars. The Ψ_i can also be expressed in terms of a coordinate basis, but this has been omitted here since we will no longer use coordinate bases. The tetrad basis allows us to express the Weyl scalars independent of our chosen coordinate system, and thus the Weyl scalars are completely dependent on tetrad choice and are coordinate-invariant.

3.6 Petrov Classification of Spacetimes

As already mentioned, the Weyl scalars, while coordinate invariant, are not tetrad invariant. We can then ask the question: how do different tetrad choices affect the values of the Weyl scalars? This is in fact an important question, and consequently has an important answer: the tetrad choice changes properties of the spacetime that the Weyl scalars define. This means that choosing different tetrads can set one (or more) of the $\Psi_a = 0$, and we can classify different spacetimes according to which, and how many, Weyl scalars vanish. This is known as Petrov classification of spacetimes, and is useful when trying to extract gravitational waves since, in some spacetimes, gravitational waves do not appear. This section uses [3] and [14] as references; however, we will continue following the convention outlined by [3] in order to remain consistent.

3.6.1 Petrov Types

There are several methods of determining the Petrov classification of a given spacetime. Consider the following eigenvalue equation

$$\frac{1}{2} C_{\alpha\beta\mu\nu} X^{\mu\nu} = \lambda X^{\alpha\beta} \tag{3.98}$$

where $X^\mu\nu$ are eigenbivectors and λ is an eigenvalue. Using identities in [14], this equation can be written equivalently as

$$Q_{\alpha\beta} X^\beta = \lambda X_\alpha \tag{3.99}$$

where

$$Q_{\mu\nu} = E_{\mu\nu} - iB_{\mu\nu} \tag{3.100}$$

for the electric and magnetic components E and B of the Weyl tensor. The eigenvalues λ can be used to characterize a spacetime based on their distinctness. We can use the components of $Q_{\mu\nu}$ to express the complex, symmetric, traceless, 3×3 matrix Q such that the eigenvalue equation becomes

$$Q\vec{v} = \lambda\vec{v}. \tag{3.101}$$

This is clearly an equation that can be solved using traditional eigenvalue-eigenvector methods. So, we have taken a four-dimensional Lorentz frame (with one time dimension and three spatial dimensions) and projected it onto three-dimensional complex space with a Euclidean metric. The orthogonal transformations in complex 3-space we will perform on this matrix is isomorphic to the group of proper orthochronous (time-preserving) Lorentz transformations in the four-dimensional Lorentz frame.

We now solve this equation using the basic linear algebraic methodology of determining the characteristic equation and finding its roots. The matrix Q can have at most three linearly independent eigenvectors, corresponding to three eigenvalues λ. The distinct algebraic structures of the spacetimes are characterized by the divisors $(\lambda - \lambda_1)^{m_1}, \ldots, (\lambda - \lambda_k)^{m_k}$, where m_j are the multiplicities of the eigenvalues of the characteristic equation

$$\det |Q - \lambda I| = 0. \tag{3.102}$$

The type of matrix Q provides an invariant characterization of the gravitational field at some point p. Our characterization is based on the most restrictive criteria satisfied by the spacetime at that point and is invariant under both coordinates and tetrad choices.

Petrov Type	$m_1, ..., m_k$	Matrix Criterion
I	1,1,1	all unique
D	1,1,1	$m_1 = m_2 \neq m_3$
II	2,1	both unique
N	2,1	$Q^2 = 0$
III	3	$Q^3 = 0$
O	n/a	Q=0

Table 3.2: Classification of matrix Q with respect to multiplicities m_i and corresponding Petrov spacetime classification.

Table 3.2 shows the multiplicities of eigenvalues of matrix Q and how they correspond to specific Petrov spacetime classifications [14]. Petrov Types D, II, N, III, and O correspond to algebraically special gravitational fields, and Types I, D, or O correspond to matrices Q with either imaginary or real components exclusively (since the divisors are simple). We can apply Lorentz rotations that are equivalent to elements of the group $SO(3, \mathbb{C})$ to the system to find simple *normal forms* of matrix Q. These normal forms allow us to find expressions for the Weyl Scalars in terms of the eigenvalues and eigenbivectors of our system; this is not included since it is not relevant to this thesis; however, [14] has comprehensive information on the computation and use of the normal forms of matrix Q.

The Petrov type of a spacetime can also be calculated based on the spin/boost classification of the tetrad vectors defined in Equations (3.77), (3.78), and (3.79) above. Since the Weyl scalars can be represented entirely in terms of contractions of the Weyl tensor with the tetrad vectors, we can transform the Weyl scalars using Lorentz boosts and rotations for a desired effect. Following the convention of [3], we perform a Class II transformation first and then a Class I transformation (see Equations (3.78) and (3.77)). However, the opposite can also be done and we will elaborate further on the implications of doing so in the following sections. We will derive the transformation for several of the Weyl scalars under Class II transformations, just for illustrative purposes, but will omit the derivation under Class I as it is done similarly and will just state the result.

The goal here is to attempt to eliminate one of the Ψ_a. Since all of the Weyl scalars are directly dependent on the tetrad, we can do this using tetrad transformations as discussed above. We will arbitrarily choose one of the Ψ_a to remain nonzero, in our case Ψ_4 will be used since it will be useful in future discussion of gravitational waves, and we can do this for any non-flat spacetime. We now investigate how the components of all Ψ_a change with respect to tetrad transformations.

Under Class I transformations (following notational conventions of [13]):

$$\Psi_0 = C_{1313} = C_{\alpha\beta\mu\nu} l^\alpha m^\beta l^\mu m^\nu \tag{3.103}$$

$$\to C_{\alpha\beta\mu\nu} l^\alpha (m^\beta + a l^\beta) l^\mu (m^\nu + a l^\nu) \tag{3.104}$$

$$= C_{\alpha\beta\mu\nu} (l^\alpha m^\beta + a l^\alpha l^\beta)(l^\mu m^\nu + a l^\mu l^\nu) \tag{3.105}$$

$$= C_{\alpha\beta\mu\nu} l^\alpha m^\beta l^\mu m^\nu = \Psi_0 \quad \square \tag{3.106}$$

$$\Psi_1 = C_{1213} = C_{\alpha\beta\mu\nu} l^\alpha k^\beta l^\mu m^\nu \tag{3.107}$$

$$\to C_{\alpha\beta\mu\nu} l^\alpha (k^\beta + \bar{a} m^\beta + a \bar{m}^\beta + a\bar{a} l^\beta) l^\mu (m^\nu + a l^\nu) \tag{3.108}$$

$$= C_{\alpha\beta\mu\nu} (l^\alpha k^\beta + \bar{a} l^\alpha m^\beta + a l^\alpha \bar{m}^\beta + a\bar{a} l^\alpha l^\beta)(l^\mu m^\nu + a l^\mu l^\nu) \tag{3.109}$$

$$= C_{\alpha\beta\mu\nu} l^\alpha (k^\beta + \bar{a} m^\beta) l^\mu m^\nu \tag{3.110}$$

$$= C_{\alpha\beta\mu\nu} (l^\alpha k^\beta l^\mu m^\nu + \bar{a} l^\alpha m^\beta l^\nu m^\mu) \tag{3.111}$$

$$= \Psi_1 + \bar{a}\Psi_0 \quad \square \tag{3.112}$$

$$\Psi_2 = C_{1342} = C_{\alpha\beta\mu\nu} l^\alpha m^\beta \bar{m}^\mu k^\nu \tag{3.113}$$

$$\to \Psi_2 + 2\bar{a}\Psi_1 + \bar{a}^2\Psi_0 \tag{3.114}$$

$$\Psi_3 = C_{1242} = C_{\alpha\beta\mu\nu} l^\alpha k^\beta \bar{m}^\mu k^\nu \tag{3.115}$$

$$\to \Psi_3 + 3\bar{a}\Psi_2 + 3\bar{a}^2\Psi_1 + \bar{a}\Psi_0 \tag{3.116}$$

$$\Psi_4 = C_{2424} = C_{\alpha\beta\mu\nu} k^\alpha \bar{m}^\beta k^\mu \bar{m}^\nu \tag{3.117}$$

$$\to \Psi_4 + 4\bar{a}\Psi_3 + 6\bar{a}^2\Psi_2 + 4\bar{a}^3\Psi_1 + \bar{a}^4\Psi_0 \tag{3.118}$$

The derivation of Ψ_2, Ψ_3, and Ψ_4 is omitted since the arithmetic is tedious and it adds little to the conclusion of this thesis.

Under Class II transformations: [3] The calculations here are omitted since they are done in a similar manner to those for Class I transformations.

$$\Psi_0 \to \Psi_0 + 4b\Psi_1 + 6b^2\Psi_2 + 4b^3\Psi_3 + b^4\Psi_4 \tag{3.119}$$

$$\Psi_1 \to \Psi_1 + 3b\Psi_2 + 3b^2\Psi_3 + b^3\Psi_4 \tag{3.120}$$

$$\Psi_2 \to \Psi_2 + 2b\Psi_3 + b^2\Psi_4 \tag{3.121}$$

$$\Psi_3 \to \Psi_3 + b\Psi_4 \tag{3.122}$$

$$\Psi_4 \to \Psi_4 \tag{3.123}$$

We classify the spacetime using the roots of polynomials under either transformation.

By performing first a Class II transformation and then a Class I transformation, the information in Table 3.3 will be true for the respective spacetimes.

Petrov Type	Roots of Quartic	$\Psi_a = 0$	Property of spacetime
I	a_i distinct	$\Psi_0 = 0$	generic spacetime
II	$a_1 = a_2$	$\Psi_0 = \Psi_1 = 0$	Combines effects from types III, N, D
III	$a_1 = a_2 = a_3$	$\Psi_0 = \Psi_1 = \Psi_2 = 0$	Longitudinal gravitational wave
N	$a_1 = a_2 = a_3 = a_4$	$\Psi_0 = \Psi_1 = \Psi_2 = \Psi_3 = 0$	Plane gravitational wave
D	$a_1 = a_2,\ a_3 = a_4$	$\Psi_0 = \Psi_1 = \Psi_3 = \Psi_4 = 0$	Fields of massive objects
O		$\Psi_i = 0$	Conformal flatness

Table 3.3: Petrov types of a spacetime under a Class II transformation then a Class I transformation with corresponding types of roots for equations and vanishing Weyl scalars.

Table 3.3 shows the multiplicities of the roots of the resultant polynomial equations for the Weyl scalars. It also gives the the number of vanishing Weyl scalars, including which ones vanish, and classifies the Petrov type as corresponding to something physical (i.e., Petrov type O spacetime is conformally flat). We will be looking at spacetimes that asymptotically approach type D. Note that these transformations do not change the classification of a particular spacetime.

3.7 Invariants

The curvature invariants I and J of a spacetime can be defined in terms of the Weyl Tensor:

$$I = \frac{1}{2} C_{\alpha\beta\mu\nu} C^{\alpha\beta\mu\nu}, \tag{3.124}$$

$$J = \frac{1}{6} C_{\alpha\beta\lambda\sigma} C^{\lambda\sigma}_{\ \ \mu\nu} C^{\alpha\beta\mu\nu}, \tag{3.125}$$

and algebraically special fields satisfy

$$I^3 = 27J^2 \tag{3.126}$$

with specialty index $\mathcal{S}$:

$$, \mathcal{S} = 27J^2/I^3 \tag{3.127}$$

for all spacetimes where $I \neq 0$ (for Petrov types III, N, and O $I = J = 0$). We use $\mathcal{S}$ to help determine the behavior of a spacetime as time evolves within a numerical simulation. Such a spacetime will have $S \to 1$ if it is approaching Kerr (Petrov Type D).

In terms of the Weyl Scalars, I and J can be written as [14] [3]

$$I = \Psi_0\Psi_4 - 4\Psi_1\Psi_3 + 3\Psi_2^2, \tag{3.128}$$

$$J = \Psi_0(\Psi_2\Psi_4 - \Psi_3^2) + \Psi_1(\Psi_2\Psi_3 - \Psi_1\Psi_4) + \Psi_2(\Psi_1\Psi_3 - \Psi_2^2), \tag{3.129}$$

where

$$J \equiv \det \begin{pmatrix} \Psi_0 & \Psi_1 & \Psi_2 \\ \Psi_1 & \Psi_2 & \Psi_3 \\ \Psi_2 & \Psi_3 & \Psi_4 \end{pmatrix} \tag{3.130}$$

$$\equiv \det \begin{pmatrix} \Psi_4 & \Psi_3 & \Psi_2 \\ \Psi_3 & \Psi_2 & \Psi_1 \\ \Psi_2 & \Psi_1 & \Psi_0 \end{pmatrix}. \tag{3.131}$$

By definition, I and J are invariants and do not depend on choice of tetrad vectors; thus, these relationships will hold true for a particular spacetime regardless of tetrad choice.

Principal Null Directions of a Spacetime

Consider the following equation from [30]

$$k^b k^c k_{[e} C_{a]bc[d} k_{f]} = 0. \tag{3.132}$$

There exist exactly four distinct vectors which satisfy Equation 3.132, called the *principal null directions* of a spacetime. Different principal nulls of a spacetime give different Petrov classifications. These vectors provide us with another method of determining the Petrov type of our spacetime and directly correspond to the transformation of the tetrad vectors. Furthermore, a spacetime with non-unique principal nulls is considered *algebraically special*, and, in fact, this is the same measure of algebraic speciality as was discussed in Section 3.6.1.

- Petrov Type I: four distinct principal null directions. These directions may not be linearly independent. If there exists an observer who sees a purely electric or purely magnetic Weyl Tensor then the principal nulls are linearly dependent. This means that, for invariants I and J:
  - $I \in \mathbb{R}$
  - $I^3/J^2 - 6 \geq 0$
  - For electric only: $I > 0$, $J \in \mathbb{R}$
  - For magnetic only: $I < 0$, J imaginary.
- Petrov Type II: one double principal null directions, and two simple ones.
- Petrov Type III: two double principal null directions. Here, there exists a second principal null direction l such that

$$l_{[e} C_{a]bc[d} l_{f]} l^b l^c = 0 \iff \Psi_4 = C_{abcd} l^a \bar{m}^b l^c \bar{m}^d = 0. \tag{3.133}$$

- Petrov Type D: one triple principal null direction, and one simple one. Similarly to Petrov Type III spacetimes, there exists an additional principal null direction l such that

$$l_{[e} C_{a]bc[d} l_{f]} l^b l^c = 0 \iff \Psi_4 = C_{abcd} l^a \bar{m}^b l^c \bar{m}^d = 0. \tag{3.134}$$

- Petrov Type N: one quadruple principal null direction.
- Petrov Type O: equation vanishes identically, no principal null directions.

The multiplicities of roots of equations for Ψ_4 and Ψ_0 under Class I and II Lorentz transformations give us the number of principal null directions of a spacetime and thus allow for determination of the spacetime's Petrov type. We can also begin with the normal forms of the Petrov types (as discussed in Section 3.6.1) and calculate our roots based on the eigenvalues and eigenbivectors of those systems. The results remain the same regardless.

3.8 Gravitational Wave Extraction

One source of gravitational waves is the strong-field interaction of a binary black hole (BBH) system during merger. There are other sources, for example, black hole-neutron star or neutron star-neutron star mergers, which we are also interested in, but those produce gravitational waves that are much weaker than our instruments are currently capable of detecting. As such, this thesis deals primarily with the extraction of gravitational waves from BBH sources. This section will first discuss the general techniques of extracting gravitational waves and constructing a numerical tetrad that suits our purposes. Chapter 4 will discuss more about the numerical techniques for constructing a spacetime grid that allows for binary black hole mergers to evolve to completion.

We can represent outgoing radiation using Ψ_4, which can be related to the parameter h in the following way[22]:

$$\lim_{r\to\infty} r\Psi_4 = \lim_{r\to\infty} r\left(\ddot{h}_+ - i\ddot{h}_\times\right). \tag{3.135}$$

In fact, this relationship is important in the extraction of gravitational radiation from BBH systems. We discussed in Section 3.5.2 that the Weyl scalars, while coordinate-independent, are completely dependent on our choice of tetrad vectors. One should expect, then, that tetrad choice is vital to successful construction of a spacetime from which we are able to extract phenomenological waveforms. Two different tetrads will be discussed; the PsiKadelia tetrad and the quasi-Kinnersley tetrad, and in Chapter 5 we will present a comparative qualitative analysis of the two tetrads.

3.8.1 PsiKadelia and Lazarus I

The PsiKadelia tetrad [5] calculates the Weyl scalars Ψ_0, Ψ_1, Ψ_2, Ψ_3, and Ψ_4, and the invariants I and J based on the numerical tetrad:

$$l^\mu = \frac{1}{\sqrt{2}}(e_n^\mu - e_r^\mu), \tag{3.136}$$

$$n^\mu = \frac{1}{\sqrt{2}}(e_n^\mu + e_r^\mu), \tag{3.137}$$

$$m^\mu = \frac{1}{\sqrt{2}}(e_\theta^\mu - ie_\phi^\mu). \tag{3.138}$$

with

$$C_{\alpha\beta} = R_{\alpha\beta} - KK_{\alpha\beta} + K^\gamma{}_\alpha K_{\gamma\beta} - i\epsilon_\alpha^{\gamma\delta}\nabla_\delta K_{\beta\gamma} \tag{3.139}$$

where $R_{\alpha\beta}$ is the Ricci curvature tensor of the spatial metric $\gamma_{\alpha\beta}$ and $K_{\alpha\beta}$ is the extrinsic curvature of a slice. This construction of the tetrad vectors leaves us in a non-transverse frame whose Weyl scalars take the form:

$$\Psi_0 = C_{\alpha\beta}m^\alpha m^\beta, \tag{3.140}$$

$$\Psi_1 = \frac{1}{\sqrt{2}}C_{\alpha\beta}m^\alpha e_r^\beta, \tag{3.141}$$

$$\Psi_2 = \frac{1}{2}C_{\alpha\beta}e_r^\alpha e_r^\beta, \tag{3.142}$$

$$\Psi_3 = -\frac{1}{\sqrt{2}}C_{\alpha\beta}\bar{m}^\alpha e_r^\beta, \tag{3.143}$$

$$\Psi_4 = C_{\alpha\beta}\bar{m}^\alpha \bar{m}^\beta, \tag{3.144}$$

which, since $\Psi_1 \neq 0 \neq \Psi_3$, does not lie in a transverse frame. This means, then, that Ψ_4 is a linear combination of all five Weyl scalars, which introduces information encoded within that is not necessarily outgoing radiation. In the following section, we will discuss the benefit of using the *quasi-Kinnersley* tetrad, which does exist in a transverse frame.

3.8.2 Lazarus II: Quasi-Kinnersley Tetrad

The second method of gravitational wave extraction is via the computation of the quasi-Kinnersley tetrad, which lies in a transverse frame (i.e. has the Weyl scalars $\Psi_1 = \Psi_3 = 0$). In general, the procedure outlined in Section 3.8.1 will not yield a tetrad existing in a transverse frame. This will contribute to an inaccurate representation of outgoing radiation since more information is included in the output of Ψ_4 than radiation output.

We have already discussed (in Section 3.6) how to construct the symmetric, complex 3×3 matrix $Q_{\mu\nu}$ so that the eigenvalues of $Q_{\mu\nu}$ correspond to transverse frames of a spacetime and the corresponding eigenvectors give the principal directions of the spacetime. The components of $Q_{\mu\nu}$ are composed of combinations of the Weyl Scalars so that

$$Q_{\mu\nu} = \begin{pmatrix} -\Psi_2 + \frac{\Psi_0+\Psi_4}{2} & \frac{i(\Psi_0-\Psi_4)}{2} & \Psi_3 - \Psi_1 \\ \frac{i(\Psi_0-\Psi_4)}{2} & -\Psi_2 - \frac{\Psi_0+\Psi_4}{2} & -i(\Psi_1 + \Psi_3) \\ \Psi_3 - \Psi_1 & -i(\Psi_1 + \Psi_3) & 2\Psi_2 \end{pmatrix}, \tag{3.145}$$

whose characteristic polynomial is defined as

$$|Q - \lambda I| = \lambda^3 - I\lambda - 2J, \tag{3.146}$$

from which the eigenvalues can be calculated. Recall the speciality index S [4] calculated from the invariants I and J such that

$$S = \frac{27J^2}{I^3} \tag{3.147}$$

which measures deviations of a spacetime from algebraic speciality. As $S \to 1$ for a system, it approaches algebraic speciality and is close to Type D. Small deviations from $S = 1$ implies our system is a perturbed Type D spacetime. There exists one preferred eigenvalue of matrix Q, which has been shown to be the eigenvalue with largest complex norm. The frame associated with this eigenvalue is called the *quasi-Kinnersley* frame [9].

The quasi-Kinnersley tetrad

Recall that we can write $C_{ac} = Q_{(i)(j)} e_{(i)a} e_{(j)c}$. We have switched to Latin indices here because it is more standard, but the meaning of the equations has not changed. Choosing the correct eigenvector

V of this system allows us to define the spatial eigenvector [8], [23]

$$\vec{\sigma} = V_i e_i = \sqrt{2}\,[V_1 e_1 + V_2 e_2 + V_3 e_3] \tag{3.148}$$

such that $||\vec{\sigma}|| = 1$ and $\vec{\sigma}^a = x^a + iy^a$. We can use the 3D Levi-Civita tensor ϵ_{abc} to construct a third orthogonal vector $\vec{z}$:

$$z^a = \epsilon^a{}_{bc} x^b y^c. \tag{3.149}$$

The quasi-Kinnersley tetrad vectors are then

$$\vec{l}_{qK} = \frac{|c|}{\sqrt{2}} \left(||\vec{x}||\vec{e}_n + \frac{\vec{x} + \vec{z}}{||\vec{x}||} \right), \tag{3.150}$$

$$\vec{n}_{qK} = \frac{1}{|c|\sqrt{2}} \left(||\vec{x}||\vec{e}_n + \frac{-\vec{x} + \vec{z}}{||\vec{x}||} \right), \tag{3.151}$$

$$\vec{m}_{qK} = \frac{e^{i\xi}}{\sqrt{2}} \left(\sqrt{||\vec{x}||^2 - 1}\,\vec{e}_n + \frac{\vec{z} - i\vec{y}}{\sqrt{||\vec{x}||^2 - 1}} \right), \tag{3.152}$$

for arbitrary spin boost parameter $c \equiv |c|e^{i\xi}$; choose $c = 1$ and $\xi = \pi/2$ so that the above tetrad will approach the PsiKadelia formulation at large distances from the source.

An important consequence of the calculation of the Weyl scalars in terms of either of the tetrads defined above is the computation of the invariants I and J and thus the specialty index S, which helps us determine whether our system is approaching the Kerr (Type D) spacetime as it evolves. Once we have computed these values, we must then determine the Kinnersley tetrad values of Ψ_4, and evolve the spacetime using the Teukolsky equation [26], and finally we will be able to extract gravitational radiation information at a specified time. For more information, see [9]. This process is highly nontrivial and, while accurate, is less apt for dealing with the strong field region of a BBH system. In Chapters 4 and 5 we will discuss in great detail how well both tetrads resolve Ψ_4 very close to the sources by analyzing a visualization of a simulation of GW150914.

Chapter 4

Binary Black Holes

A binary black hole (BBH) system is made up of two black holes orbiting each other in close enough proximity so that merger is likely or inevitable. When discussing BBH systems, we typically consider black holes of tens of solar masses in size, but supermassive binary black hole systems of size millions of solar masses to tens of billions of solar masses are also possible. Upon merger, the BBH system produces an immense amount of energy that is radiated away in the form of gravitational waves. One of the main interests in numerical relativity lies in the simulation and extraction of gravitational wave information, which can then be compared to observational data from LIGO detectors. These NR simulations help LIGO to determine whether a BBH merger has occurred, and, if so, its size, the amount of gravitational radiation produced, and its approximate location. Extensive modeling of BBH systems of tens of solar masses has already been completed (SXS [21], Georgia Tech [18], RIT [17]), beginning in inspiral, and continuing through merger and ringdown.

4.1 Introduction to BBH Evolutions

Computational techniques for BBH evolutions are, at present, a topic of great interest in numerical relativity. At times sufficiently before merger, we use post-Newtonian approximations to simulate inspiral and transition to numerical relativity techniques as we get closer to merger. Post-Newtonian approximations of a spacetime essentially add terms to equations from Newtonian gravity in order to approximate relativistic scenarios. These are convenient as they can be solved analytically, whereas close to merger we must use numerical relativity techniques to fully and explicitly solve the equations of relativity, since no analytic solutions are known to exist. This chapter will focus on the binary black hole mergers produced by numerical relativity simulations and how visualizations of such simulations provide insight into the physical properties of a BBH system.

A common method for solving the Einstein Field Equations numerically is the discretization of spacetime into a grid-like structure. Close to the black holes (which are assumed to be distorted Kerr, since Schwarzschild is not of particular interest in this thesis), a very fine grid structure is required in order to evaluate the Einstein Field Equations at a significantly large number of points. This means that the computation of a spacetime very close to the balck holes during and near merger is highly nontrivial.This poses several problems;

1. computational efficiency - the equations we are concerned with are highly nonlinear, and computation requires weeks of supercomputer time,
2. discretization techniques - how to choose which technique for discretization is best (should the grid be circular or rectangular?), and
3. numerical instability - as is expected, a larger number of points leads to higher numerical error.

Despite these setbacks, current numerical methods are quite accurate and independent methods seem to agree with both one another and observational data [20]. At RIT, the Center for Computational Relativity and Gravitation (CCRG) uses LazEv implementation of the moving puncture approach. We choose to use a rectangular grid, but it is also possible to use spherical coordinates to construct the grid, and in fact the group SXS uses a Spectral code (SpEC) that decomposes the metric into bispherical coordinates [19]. Comparisons [20] have found that the two methods provide comparable results, but one method may be faster for a certain set of parameters than the other. Discussing when this is the case is beyond the scope of this thesis; however, the reader is referred to [20] for more detail.

4.2 Visualizations of BBH Evolutions

4.2.1 VisIt Visualization Software

The visualization was done using VisIt visualization software by LNLL laboratories. VisIt is a powerful tool that is used by researchers to help visualize simulation data and derive physical meaning from computational or numerical results. Using VisIt via the User Interface (UI) was found to be rather inefficient, since it required resetting all parameters and settings upon each login. Figure 4.1 shows a screenshot of the VisIt UI to give the reader an idea of how the interface looks.

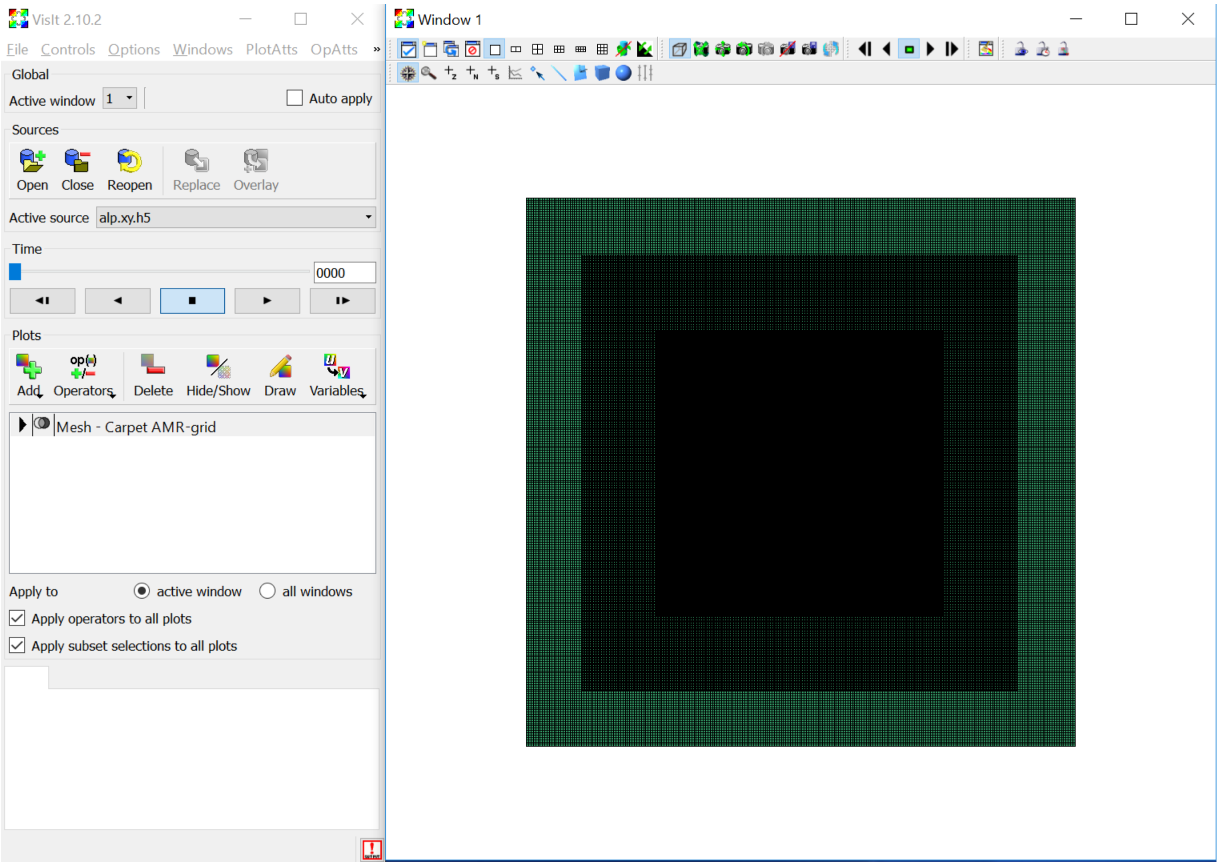

Active window 1

☐ Auto apply

Active source alp.xy.h5

Time 0000

Mesh - Carpet AMR-grid

Apply to ● active window ○ all windows

☑ Apply operators to all plots

☑ Apply subset selections to all plots

Figure 4.1: VisIt UI. The window on the right hand side shows what is being plotted, the UI is on the left hand side. The operators and attributes are changed via the drop down menus under the Plots section.

To rectify this, all parameter values and settings were changed within the Python command interface, which allows the user to save settings within a Python script that can just be run whenever VisIt is loaded. VisIt was also not capable of doing any camera manipulation when its built-in movie-making software was used, so a script was written for that as well. Included in Appendix B is a script that zooms in and out based on a function $f(x) = \tanh(x)$ where x is a timestep. More detail on this code is provided in the documentation.

In addition, VisIt's ability to create a movie was found to be somewhat lacking; whether this is a product of the use of a personal computer or problems in VisIt's own software is unknown and is beyond the scope of this thesis to discuss. To solve this problem, VisIt was used to generate .jpg images and a program called MakeAVI strung these .jpg images into a .avi movie file. VirtualDub was used for some post-processing features (including logos and increasing output quality), and Windows MovieMaker was used to sew the .avi clips together into a continuous movie, and for adding music, credits/text slides, and some transitions between clips.

Instead of using the UI to set parameters, scripts were created that set all relevant options. See Appendix A for explicit scripts. This is significantly more efficient and consistent than using the UI to change parameters and would potentially be helpful for constructing a visualization of another simulation of a different BBH system.

Tables 4.1-4.5 give the parameters for the entire visualization, the radiation before merger, the radiation after merger, the horizons, and the lapse respectively.

Parameter	Value
View	0 -1.75 -1
Zoom	2
Pan	0 .0343511460814625
Lighting	0 -.3 1

Table 4.1: These parameters are for setting the visualization parameters for the spacetime. Since the camera angle changes, these are not constant throughout, but they are the inital settings used. The code is attached in Appendix B. View, zoom, pan, and lighting change the angle and zoom of the visualization to exaggerate features we were interested in visualizing.

Parameter	Value
Project	n/a
Elevate	n/a
Transform	10000
Cylinder	100000 r = 10

Table 4.2: Radiation prior to merger initial settings. Transform scales the z values by 10000 to exaggerate outgoing radiation. Cylinder cuts out a cylinder of radius $r = 10$ from $z = -100000$ to 100000 to prevent the plane from jumping due to outliers in the dataset.

Parameter	Value
Project	n/a
Elevate	n/a
Transform	$z = 10000$
Cylinder	$z = 100000$, $r = 10$

Table 4.3: Radiation post merger final settings.

Parameter	Value
Max/Min	±1
Color	hot_desaturated
Transform	$z = 12$

Table 4.4: Settings for horizon curvature; these were maintained throughout the entire visualization. The maximum and minimum values set the bounds for the mean curvature so that the normalized values were visible on the horizons.Transform moved the horizons above the plane by $z = 12$ units so that they were visible during spacetime evolution.

Parameter	Value
Color	Spectral
Project	n/a
Elevate	n/a
Transform	$z = 5$

Table 4.5: Settings for lapse; these were maintained wherever lapse is shown in the visualization. The project and elevate operators project 3D data onto a 2D plane and elevate the data by the z value. Transform scales the z values by $z = 5$ to exaggerate the spacetime curvature.

4.2.2 Simulation

LazEv

There are two main methods to evolve BBH systems: the first is LazEv, an AMR (Adaptive Mesh Refinement)/finite differencing method, and the second is the SpEC pseudo-spectral code[25], [10], and [6]. Our simulation was done using the LazEv code. It takes as parameters the sum of the masses of the black holes M, the mass ratio q, and the spins a_1 and a_2. Since the spins in our simulation were rather small ($a_1 = -0.44$ and $a_2 = +0.33$) and the mass ratio was close to unity ($q = 0.82$), the code was able to evolve the simulation fully. As the spins approach ±1 and the mass ratio decreases to 0, the simulation becomes more expensive and current techniques are not equipped to handle such parameters in an effective way. LazEv was able to complete the simulation in 1-2 weeks depending on the grid discretization. The run was completed three times with different discretizations denoted N100, N110, and N120, with the N110 and N120 runs increasing in resolution by a factor of 1.1 and 1.2 respectively.

LazEv uses a moving puncture approach, which means that there are two punctures in a geometric plane which are orbiting with respect to time. The EinsteinToolKit implements this LazEv run, and the Carpet code defines how the spacetime is evolved. Carpet uses a style of mesh refinement called moving boxes where moving refined grids of fixed size are arranged around the coordinate singularities of both black holes so that neither singularity is actually on the grid. These grids are moved per the coordinate trajectories of the black holes and the EFEs are solved at each gridpoint in the spacetime. To solve the PDEs, a sixth-order Finite Difference (FD) approach was used in space, a fourth-order Runge-Kutta (RK4) method was used in time, and a seventh-order Kreiss-Oliger method was used as the dissipation operator. The FD increased efficiency by a factor of 4/3 with respect to an eighth-order FD approach. The CFL was allowed to be 1/3 as opposed to 1/4, which increased efficiency and speedup by another factor of 4/3. For the N100 run, the evolution ran at 250M/day on 16 supercomputer nodes.

To find the apparent horizons, as already discussed, AHFinderDirect was used, which finds the apparent horizons. At early times in the simulations (during inspiral) the black holes are treated as independent from one another. This allows for an increase in computational efficiency without sacrificing significant accuracy of our simulation results.

This methodology allows us to extract the remnant mass of the final black hole, where $m_{rem}/M < 1$ for $M = m_1 + m_2$, and tells us how much mass was radiated away in the form of gravitational waves, a final spin parameter for the black hole, and its final angular velocity. The particular simulation of GW150914 computed here is not particularly costly for the set of initial parameters used. However, for an inspiral that remains in the LIGO band for longer (meaning LIGO can detect the inspiral for longer time) and thus has a higher number of orbits can be significantly more computationally expensive and sometimes even impossible to simulate using our current techniques and hardware.

Grid Discretization

When performing a numerical simulation of a spacetime, one must discretize each spatial slice in the same way and perform computationally intensive calculations at each point. Far from the sources a coarse grid can be used, but very close to the sources we must use an extremely fine grid structure to see the intricacies of the numerical simulation. The point density of the grid in this simulation, beginning at the sources, decreases in number by a factor of 2 at each grid level, with the coarsest grid being farthest from the black holes. Figure 4.2 illustrates the density of the outer grid layers.

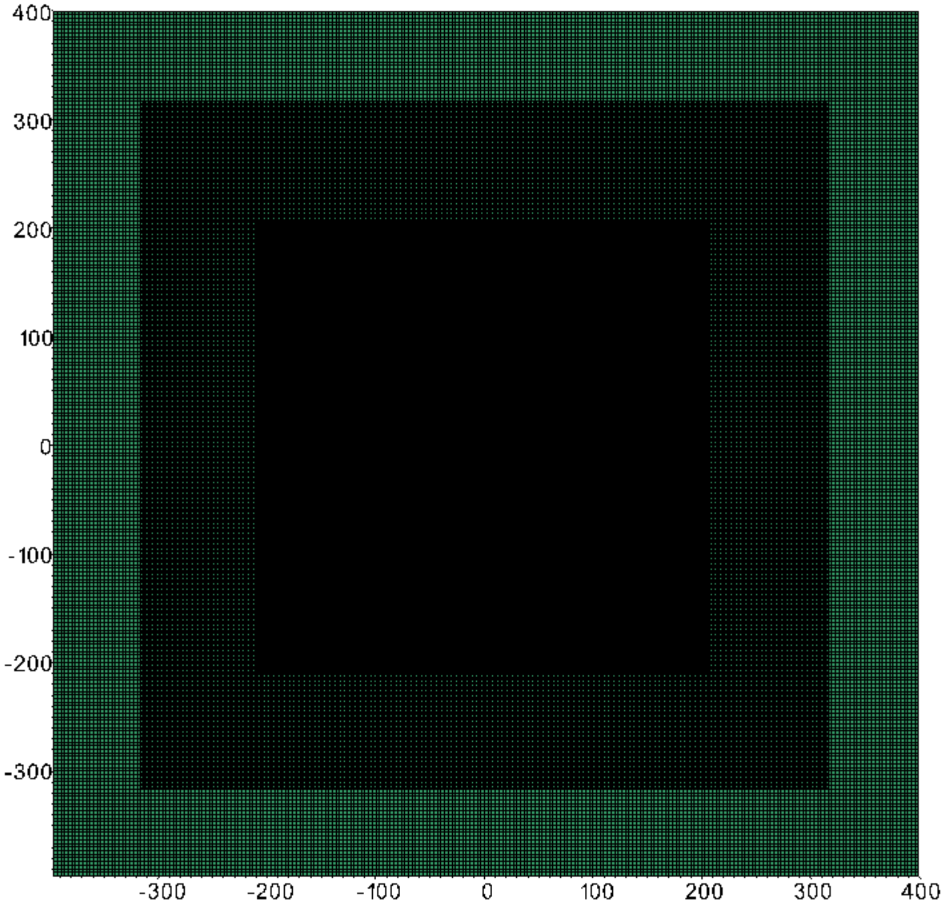

Figure 4.2: Outermost layers of the grid structure.

The grid has bounds in $x:\ (-400M, 400M)$ and $y:\ (-400M, 400M)$ and, on its outermost layer, has $240^2 - 192^2 = 20736$ points at a spacing of $\frac{10}{3}M$. The second grid halves the spacing between grid points, and subsequent grids further decrease the spacing by a factor of two. Figure 4.2 includes the three outermost layers of the grid system, leading up to two layers before the grid decomposes into two separate parts surrounding each black hole. The grid is shown in a bird's eye view to give the reader an accurate idea of what a grid discretized in this way looks like.

It also helps to illustrate how the grid structure is becoming more and more finely space as we move inward toward the black holes. Close to the sources exists the finest grid structure to give the most detail. Once we get close enough to the sources, the fine grids then split into two separate grids of equal resolution surrounding the black holes. Figure 4.3 shows the finest four grids.

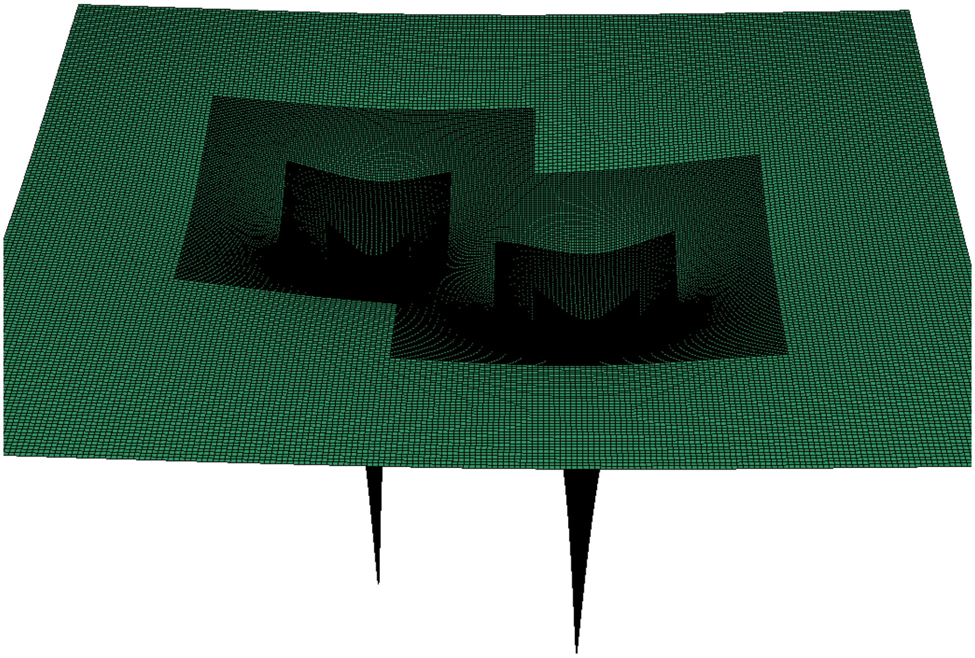

Figure 4.3: Grid layers close to the black holes split into two separate grids of equal spacing surrounding each black hole.

The grid structure close to the black holes is apparent in Figure 4.3. It includes the layer right before the grid decomposes into two separate parts surrounding each black hole, and then all the subsequent, more finely discretized grids. The grid is elevated in the $z-$ direction to make apparent the dramatic curvature changes closest to the singularities. We can see the grid structure becoming more and more finely spaced as we move inward toward the black holes. There are nine grid layers in total. Table 4.6 below shows the resolutions of each grid and the initial radii at which the grids are placed.

Grid	dx	Resolution res	rm	rp
0	3.33333333	M/0.3	400	400
1	1.66666667	M/0.6	300	300
2	0.83333333	M/1.2	200	200
3	0.41666667	M/2.4	50	50
4	0.20833333	M/4.8	12.8	13.6
5	0.10416667	M/9.6	6.4	6.8
6	0.05208333	M/19.2	3.2	3.4
7	0.02604167	M/38.4	1.6	2
8	0.01302083	M/76.8	0.9	1.2

Table 4.6: There are nine grid levels. Their spacing dx has units M and is the step size between points on the grid. The resolution/M is the resolution of each grid level; it should correspond to the parameter dx. The final two columns rm and rp are the sizes of the grids - for Grids 0-4, the rm and rp are centered around the origin so they should correspond, but for Grids 5-8 rm and rp are centered around the horizons at xm = -6.73077 and xp = 5.51923 respectively at the start of the simulation.

Table 4.6 shows the grid structure of the initial setup of the BBH system GW150914 in our simulation. There are a total of nine grid layers, with discretizations given by dx, which measures distance in M between each point. As we move upward in the grid layers, we see that $dx \to 0$ such that level 0 is the coarsest grid and level 8 is the finest. The resolution res gives the resolution of each grid level; this corresponds with the dx column and is such that $res = M \cdot dx$. At level 4, the grid splits into two parts: $r =$ rm and $r =$ rp with rm centered around the smaller black hole and rp centered around the larger black hole. The parameters rm and rp define the distance from the center of the grid level outward. So, for the coarsest grids (0-4), these parameters coincide since we have one grid at each layer surrounding both black holes. For the finer grids (5-8), however, rp and rm are centered around the centers of the black holes at xp = 5.51923 and xm = -6.73077 respectively and thus are dependent on the sizes of the black holes. From Table 4.6 and Figures 4.3 and 4.2 it is clear that these grids are finest closest to the singularities, since we want the most detail near the black hole horizons. However, problems occur at the singularities of the black holes. To successfully complete a simulation we have to force the grid to either excise the area inside the apparent horizon to avoid singularity issues, or we have to discretize our grid in such a way that the $r = 0$ singularity will never be a grid point (we do the latter).

Simulation Parameters

The initial parameters used to perform the simulation of the BBH merger shown in this visualization [20] allow us to numerically resolve the waveform that LIGO detected from the September 2015 merger of two black holes (see Figure 1.2). It is important to note, however, that this is only one of many mass/spin configurations of black holes that produce these waveforms, and there are a range of possible parameters for both mass and spin. The parameters used in this simulation are given in Table 4.7.

Parameter	Value
Mass Ratio	$q = \frac{m1}{m2} = 0.82$
Spins	$a_1 = -0.44$ $a_2 = +0.33$
Run Length	$t = 2400M$
Visualization Length	$t \approx 1700M$
Scale	$65M_\odot$

Table 4.7: Parameters that produce the gravitational waveform exhibited by GW150914.

The visualization begins approximately $t = 360$ milliseconds prior to merger with both apparent horizons displaying over the spacetime lapse α. A graphic of the mass/spin configuration of the system is shown in Figure 4.4.

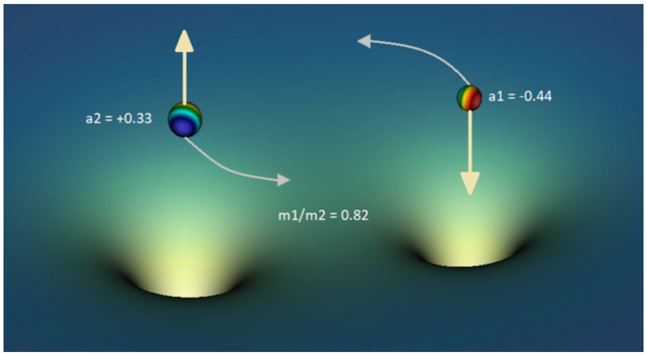

Figure 4.4: The mass/spin configuration of the simulated BBH system.

In Figure 4.4 we see that $m_1 < m_2$ since $q = \frac{m_1}{m_2} = 0.82$. The spins of the black holes are anti-aligned, with the spin of m_1 (referred to henceforth as AH1) in the negative $z-$direction so $a_1 = -0.44$, and the spin of m_2 (AH2) in the positive $z-$direction so $a_2 = +0.33$. The black holes are orbiting in the counterclockwise direction around their center of mass at an initial separation of $a = 12.25M$.

4.2.3 Visualization

The visualization begins with the apparent horizons AH1 and AH2 displayed over the spacetime lapse α and with their mean curvature plotted on top. Figure 4.5 is a still from the first part of the movie, at $t = -183$ ms before merger.

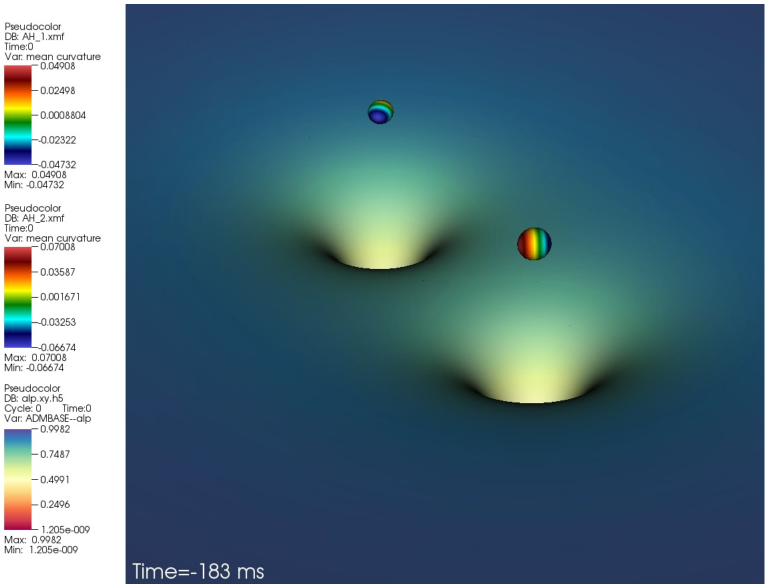

Figure 4.5: The first part of the visualization shows the apparent horizons with their mean curvature plotted over the spacetime lapse.

We will not be looking in depth at α; however, it is worth noticing how the spacetime heads toward asymptotic flatness far from the black holes but exhibits steep changes extremely close to (and underneath) the black holes. On the apparent horizons of the black holes is displayed the mean curvature. The color gradient is as follows: red denotes larger values of mean curvature and blue smaller values of curvature. The curvature on the apparent horizons is not axially symmetric since the horizons are orbiting at a fraction of the speed of light c and thus are distorted. We expect this distortion to occur with respect to the trajectory of the individual black holes, and in fact in Section 5.2.1 we will show that this is the case.

Now the movie zooms outward to see the radiation emitted by the BBH system during inspiral. In Figure 4.6, we see how outgoing radiation is visualized from simulation data. This image is still rather far from merger, so we do not see the large spikes of radiation we expect during merger.

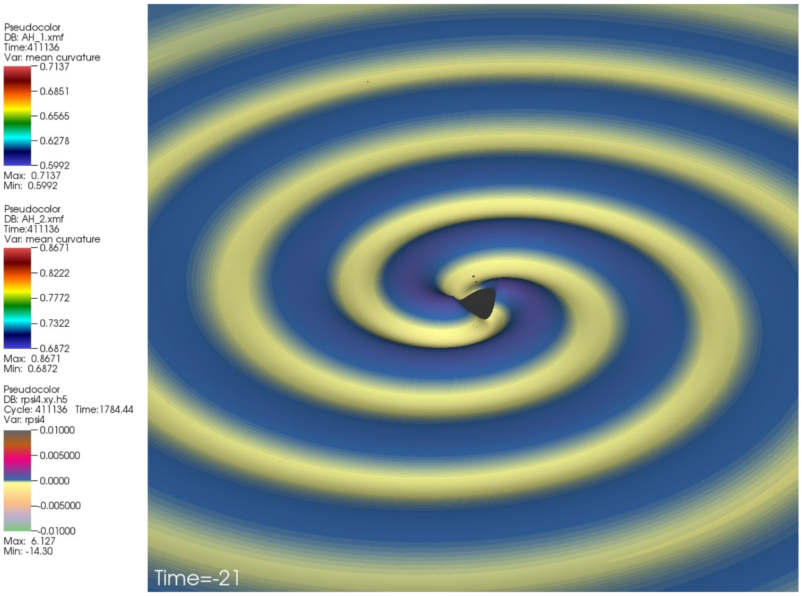

Figure 4.6: Radiation being emitted from the BBH system during inspiral.

The (2,2)-modes of Ψ_4 are clearly exhibited here. Both blue and yellow modes represent outgoing radiation such that blue are values of $\Psi_4 > 0$ and yellow are values of $\Psi_4 \leq 0$. The values of Ψ_4 are scaled here by a factor of 10000 so that planar radiation emission is visualized in the z-direction We can see the blue values growing in the $z-$direction since Figure 4.6 shows the BBH system at 21 milliseconds prior to merger. This means that as merger approaches, the amount of radiation emitted grows larger and larger until peaking just before merger as shown in Figure 4.7.

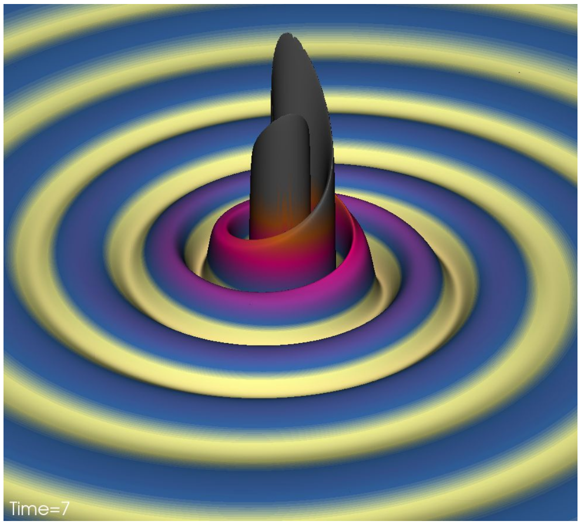

Figure 4.7: Radiation emitted from the BBH system at and after merger.

Here, the gray peak is the radiation emitted just at merger and since the screenshot has been taken only 7 milliseconds post-merger, the large spike in radiation is still obvious. As the final apparent horizon settles down, no more radiation will be emitted from the black hole; in Figure 4.7 this is almost evident since there seems to be no more peaks in radiation after the initial spike. The end of the visualization will confirm this, but first we must discuss what happens to the mean curvature and the apparent horizon surfaces during and just after merger.

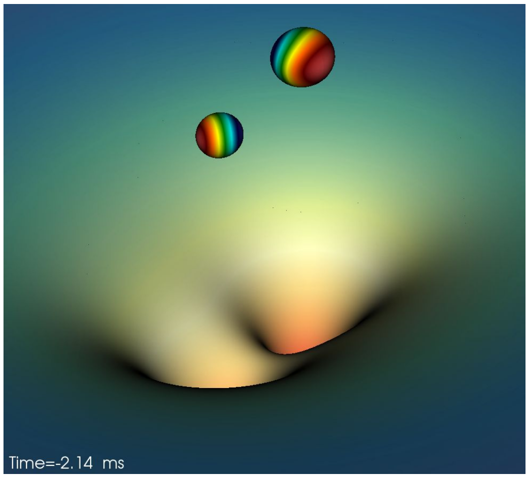

Figure 4.8: Apparent horizon mean curvature and distortion close to merger plotted over lapse.

In Figure 4.8 we see the mean curvature again displayed on the apparent horizons of the black holes and plotted over the spacetime lapse. Notice that even 2.14 milliseconds from merger, the mean curvature seems to follow the trajectory of the individual black holes. There exists some distortion in the horizon shapes and curvature, but this is nothing more than a product of the horizons being extremely close to merger. The following images in Figure 4.9 occur successively, and are separated by 1/100th of a millisecond.

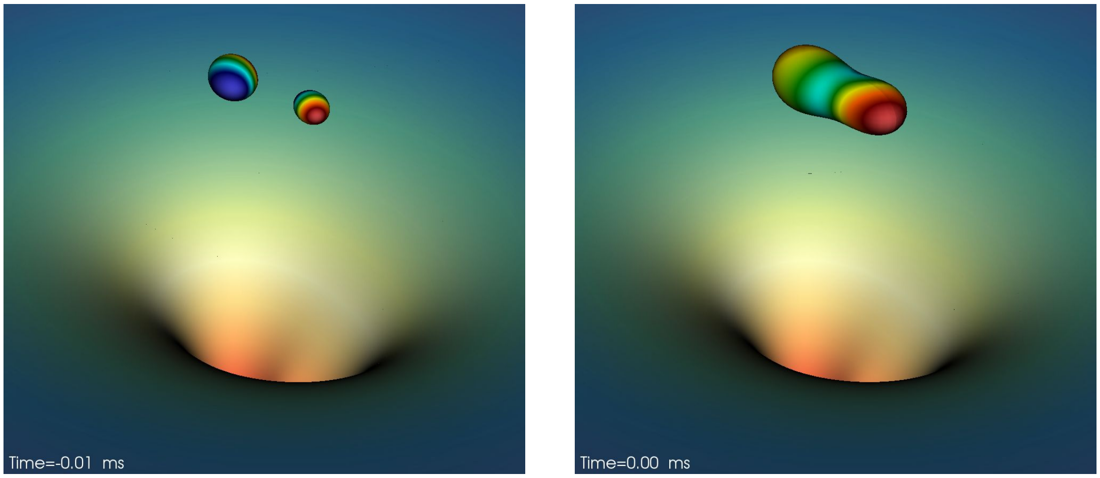

Figure 4.9: Successive screenshots of the apparent horizons at merger.

Since this simulation calculated apparent horizons, we do not see the horizons being pulled toward each other and deformed into needle-like shapes before touching as we would if event horizons were displayed [15], [24]. Instead, we see a third horizon jumping to encapsulate both initial apparent horizons. In fact, the initial apparent horizons do not disappear until the third horizon is completely settled into its axially symmetric shape. The curvature changes in the post-merger horizon (AH3) are drastic and in fact, for several milliseconds after merger it does not resemble the spherical structure one normally associates with black holes. Before we see the horizon curvature of the third black hole settle, we transition back to the radiation emitted after merger to verify that the radiation emitted drops to zero after merger as shown in Figure 4.10.

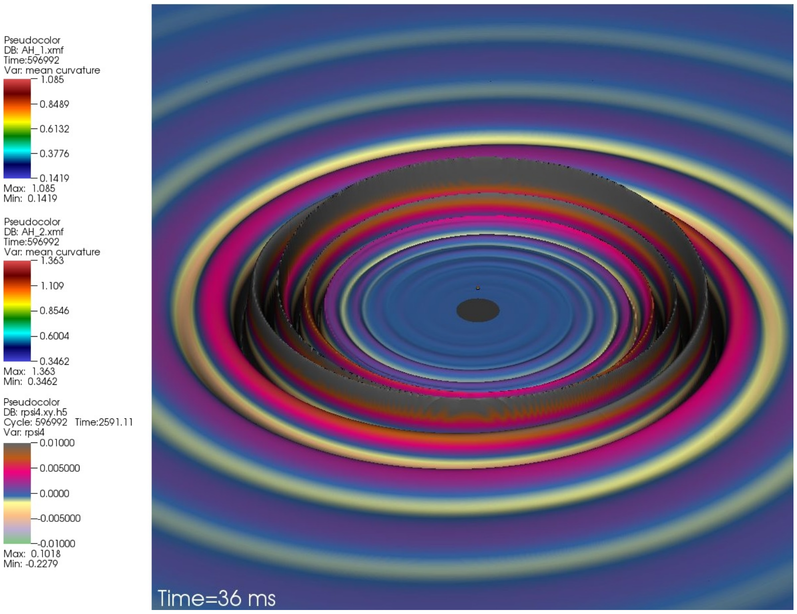

Figure 4.10: Radiation emitted from BBH system drops off to zero after merger.

The color scale is changed slightly here so blue implies no radiation emitted from the black hole (or at least values very close to zero). We see the spike in radiation moving outward from the remnant black hole (the gray concentric rings), but as was postulated earlier, there seems to be no more radiation emission after the final merger and ringdown of the BBH system. We can look a bit farther out after ringdown to confirm this remains true, as shown in Figure 4.11.

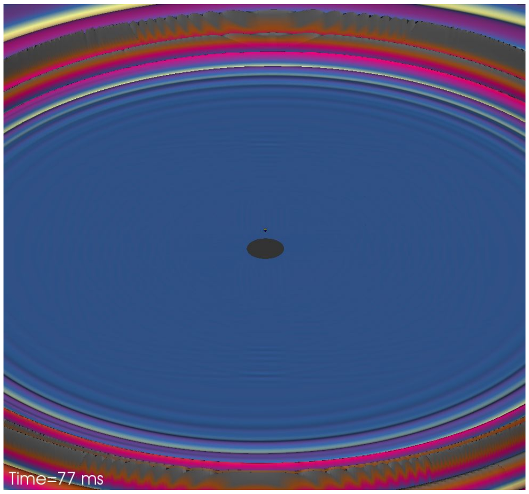

Figure 4.11: Radiation emitted from BBH system drops off to zero 77 ms after merger and post-ringdown.

Note here that the color scale has changed; blue now shows outgoing radiation values at or very close to zero. Since the plane surrounding the apparent horizon is solidly blue and flat, it is clear that there is no more radiation being emitted from the remnant black hole and thus $\Psi_4 \approx 0$.

The final part of the movie shows the mean curvature of AH3 settling during ringdown. We find that the final apparent horizon settles into a nearly axially symmetric spherical shape at around 20 milliseconds after merger, but significantly earlier than that the curvature is unsettled. Figure 4.12 shows AH3 at both 5.91 milliseconds and 11.83 milliseconds post-merger; since the final horizon is not yet converged to Kerr, its curvature is also not yet settled to a constant state.

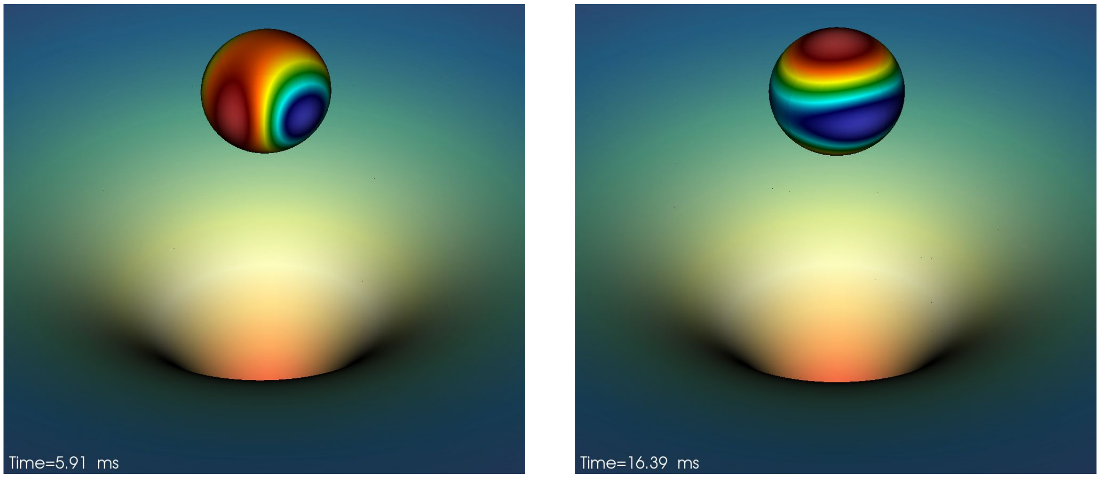

Figure 4.12: AH3 nearly settled 5.91 milliseconds and 11.83 milliseconds after merger.

Finally, the new horizon AH3 is finally settled to a Kerr black hole 23.77 milliseconds after merger. The mean curvature seems to align here in the direction of the spin of the final black hole (which is pointing in the positive z-direction).

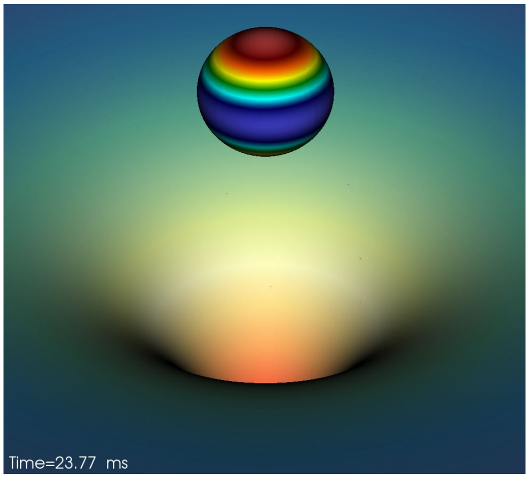

Figure 4.13: The resultant Kerr black hole 23.77 milliseconds after merger.

Figure 4.13 concludes the visualization. After merger and ringdown, the mean curvature of the newly formed apparent horizon settles in the direction of the spin of the new black hole, and there is no longer outgoing radiation being produced by the BBH system. The following chapter presents an analysis of interesting or notable features displayed in this visualization of a numerical simulation of BBH system GW150914.

Chapter 5

Results and Analysis

5.1 Simulating the Strong Field Region Using PsiKadelia and quasi-Kinnersley Tetrads

From careful analysis of the visualization in Section 4.2, we can compare how well PsiKadelia and quasi-Kinnersley perform in the strong field region of the BBH system. Recall that, when constructed via the Psikadelia tetrad, Ψ_4 is a linear combination of all five Weyl scalars, whereas in the quasi-Kinnersley frame, Ψ_4 has $\Psi_1 = \Psi_3 = 0$. Since we are interested in only outgoing radiation, it is important to minimize effects of quanities within Ψ_4 that are not pure outgoing radiation. This makes for more accurate simulated waveforms that can be compared with observational data from LIGO. Note that even though we extract Ψ_4 data from these BBH simulations, LIGO detects a different component called the *strain h*. Recall from Chapter 3 that the two parameters are related at large radii r in the following way [22]:

$$\lim_{r\to\infty} r\Psi_4 = \lim_{r\to\infty} r\left(\ddot{h}_+ - i\ddot{h}_\times\right). \tag{5.1}$$

We have already discussed that quasi-Kinnersley is a tetrad which exists in a transverse frame (such that $\Psi_1 = \Psi_3 = 0$), whereas PsiKadelia does not. This means that the approximation of outgoing gravitational waves calculated using the quasi-Kinnersley tetrad likely is more representative of actual outgoing radiation closer to the black holes, since Ψ_4 is influenced only by itself, Ψ_2 (the

Coulomb field) and Ψ_0 (ingoing radiation). The improvement of strong field region performance by using a transverse tetrad can be shown qualitatively by placing concentric circles of fixed radii around the center of the BBH system on both the quasi-Kinnersley and PsiKadelia plots. We choose these radii to be functions of the separation a or the distance in x, y, z coordinates of the system. In Figure 5.1, we see a bird's-eye view of the radiation at time $t = 1433$M as displayed by a computation of the Ψ_4 component of the Weyl Scalars.

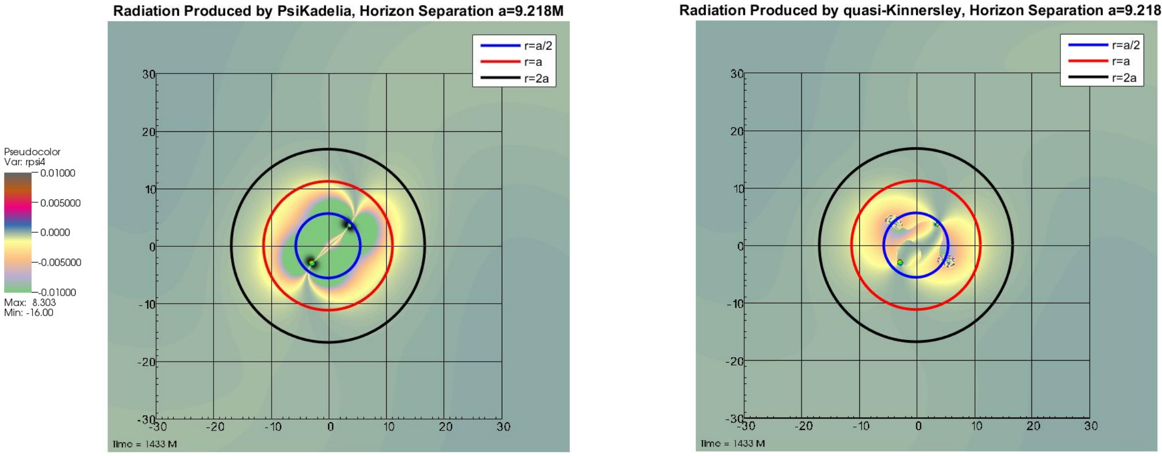

Figure 5.1: Left: strong field region of BBH system using PsiKadelia. Right: quasi-Kinnerlsey. Concentric circles are centered around the center of mass of the system, with radii $r = a/2, a, 2a$ for separation $a = 9.218$.

In both plots of Figure 5.1, the color scale used is exactly the same, which allows for accurate comparison. Outside of the circle $r = 2a$, for separation a, the outgoing radiation is visualized via the yellow-green color. We expect there to be two outgoing spirals coming from the black holes since we have $(l, m) = (2, 2)$, and they can be seen clearly in Figure 5.1. The colorbar gives an indication of the value of Ψ_4.

By [3], we expect radiation to be extracted accurately computed outside radii $r \geq 2T$ for period of radiation T using either method and, in fact, this is what we see. Since the quasi-Kinnersley and Psikadelia tetrads exhibit very similar behavior in this *weak field* region, our comparison focuses primarily on their differences within the radii $r \leq 2T$. The radii of the circles are spaced at a factor of the separation $a = 9.218\text{M}$ of the horizons.

In Figure 5.1, we have blue, red, and black circles centered between the black holes at radii of $r = a/2,\ a,\ 2a$. Outside these circles on the top right and bottom left of each plot, we see outgoing radiation in yellow, and on first inspection the visualizations seem to exhibit similar results. We will return to the weak-field region later in this section.

Inside the circle of radius $r = 2a$, we begin to see several major differences. In each plot there are two lobes extending outward from the horizons. These lobes are *not* numerical error, but rather are associated with which tetrad was chosen to compute Ψ_4. We cannot get an accurate representation of outgoing radiation in the strong-field region of the BBH system using either tetrad, since both contain Ψ_2 and Ψ_0, and the PsiKadelia tetrad also contains nonzero Ψ_1 and Ψ_3. The plots, however, accurate representations of Ψ_4 under a given tetrad.

In the PsiKadelia (left hand) plot of Figure 5.1, the lobes extend significantly outward into the area $r \in [a,\ 2a]$, even going so far as to affect the region outside of $r = 2a$ from about $[-8, -14]$ to $[0, 18]$ in the counterclockwise direction. The expectation is that we can accurately numerically compute radiation in the region outside radius $r = 2a$, and in fact that is not what we see in the PsiKadelia plot [3]. The lobe extension could be affecting the computation of radiation in the weak-field region, since there seem to be slight differences in those regions using the two methods. We will investigate this further later. As we move inward, the tetrad only performs worse. The interior of the circle with $r = a$ is almost entirely dominated by the lobe and nearly no accurate information regarding outgoing radiation can be gathered from the data provided here. The inside of the circle of radius $r = a/2$ contains no accurate information about outgoing gravitational radiation since the effects of the Coulomb field, the ingoing radiation, and Ψ_1 and Ψ_3 are overwhelming.

Moving on to the right-hand plot, which extracts gravitational radiation data using the quasi-Kinnersley tetrad, we see similar lobes extending from the black holes in this plot as we do in the PsiKadelia plot. However, from a qualitative inspection, these are clearly significantly smaller. In the areas between radii $r = a$, and $2a$, we are able to resolve more accurate information about outgoing gravitational waves. The lobes do not extend as far into this area and certainly do not propagate outward past the circle with $r = 2a$. Inside the circle with $r = a$, there is still significant overtaking of this region by the lobes, but they dominate around 50 percent of this circle and only their outermost edges reach $r = a$. This is an improvement from what we saw in the PsiKadelia plot. We can also see two spots perpendicular to the horizons that lie approximately at the same separation. These are numerical error due to eigenvalue computation, and are beyond the scope of this thesis to discuss. The reader is referred to [8] for more information. Inside $r = a/2$, unfortunately there is no waveform information available to us due to contamination of outgoing radiation information by the ingoing radiation and the Coulomb field.

Consider again the circle of radius $r = 2a$ in Figure 5.1. As discussed earlier, both the PsiKadelia and quasi-Kinnersley tetrads are expected to perform well at and outside of this radius. Figure 5.2 shows twenty values of Ψ_4 calculated using the PsiKadelia and quasi-Kinnersley tetrads. The values are extracted at equally spaced points on the circle of radius $r = 2a$, at angles $\phi = \frac{2\pi n}{20}$ for $n = 1, 2, \ldots, 20$. Blue circles are values of Ψ_4 calculated via PsiKadelia (Ψ_4^P) and red triangles are quasi-Kinnersley (Ψ_4^{QK}).

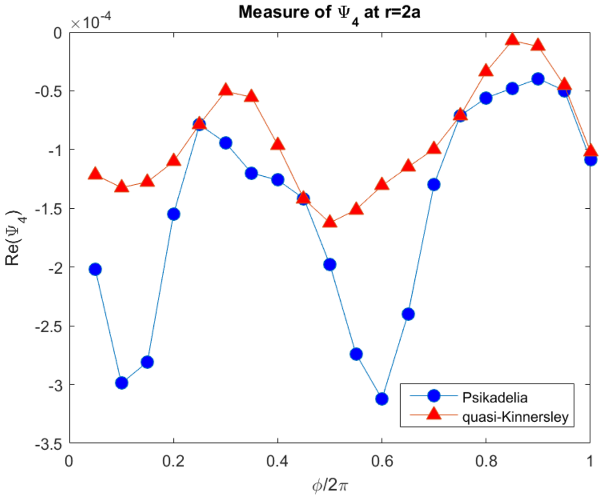

Figure 5.2: Values of Ψ_4^{QK} and Ψ_4^P at $r = 2a$ and $\phi = \frac{2\pi n}{20}$ for $n = 1, 2, \ldots, 20$, for $t = 1433M$. On average, Ψ_4^{QK} is smaller than Ψ_4^P by a factor of approximately 1.9155.

On the $y-$axis, the value of the real component of Ψ_4 is plotted for each of the two tetrads, and on the $x-$axis is the angle ϕ. In general, it can be said that quasi-Kinnersley produces smaller values of Ψ_4, in magnitude, than PsiKadelia does. The values outputted by the quasi-Kinnersley tetrad are smaller by a factor of ≈ 1.9155 on average. We expect that this is due to the fact that the PsiKadelia tetrad does not exist in a transverse frame (where $\Psi_1 = \Psi_3 = 0$) and so Ψ_4^P contains effects from all five Weyl scalars. Since Ψ_4^{QK} exists in a transverse frame, we expect it to more closely represent purely outgoing radiation. This means that smaller values of Ψ_4 are expected, and in fact, this is shown to be true in Figure 5.2.

The plots in Figure 5.3 below show how Ψ_4^{QK} and Ψ_4^P behave in the weak-field region. Outgoing radiation is visualized for coordinates $x, y \in [-100M, 100M]$. The blue, red, and black circles are set at radii $r = a/2,\ 3a/2,$ and $3a$ respectively, again with $t = 1433$M. The left plot is radiation extracted via the PsiKadelia tetrad, and the right plot uses quasi-Kinnersley.

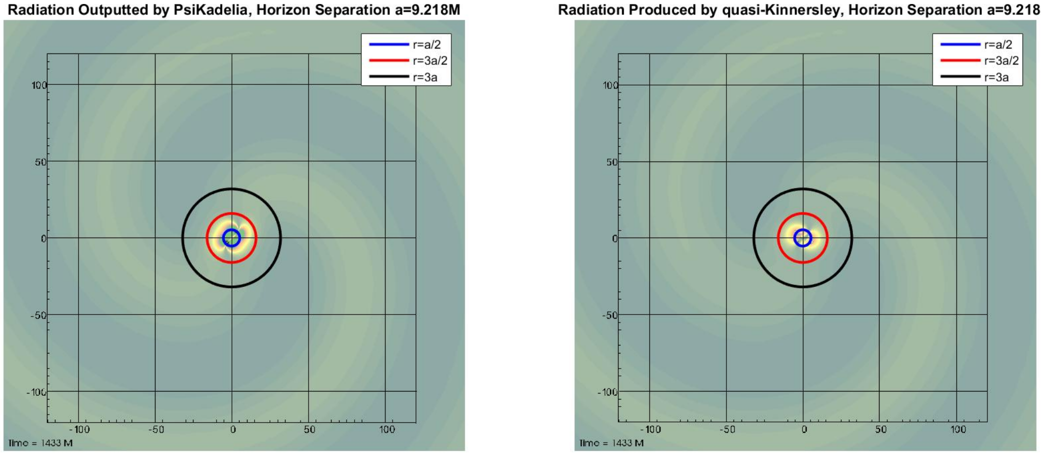
Radiation Outputted by PsiKadelia, Horizon Separation a=9.218M

Radiation Produced by quasi-Kinnersley, Horizon Separation a=9.218M

Figure 5.3: Left: weak field region of BBH system using PsiKadelia. Right: quasi-Kinnerlsey.

Here we can clearly see the $(2, 2)$-modes extending outward from the system (in the form of yellow arms). It is apparent from Figure 5.3 that using the quasi-Kinnersley tetrad for extraction allows us to compute accurate radiation values when resolving the strong-field region of the binary black hole system. The lobes stay almost entirely within the $r = a$ circle and, qualitatively, are prevalent in a significantly smaller portion of the plot resolved with quasi-Kinnersley than the plot using PsiKadelia. Comparing the two plots leads to subtle but important differences in the two visualizations. In the quasi-Kinnersley plot, the amount of radiation extending out from the left mode is significantly less than that of PsiKadelia. They begin to coincide around $r = [-60, 0]$ and then remain coincident in the rest of the spacetime. The right mode exhibits similar behavior, although it is less pronounced. This was quite unexpected; we hypothesized that outside $r = 2a$, there would be little (if any) difference between the quasi-Kinnersley result and the PsiKadelia one.

An interesting analysis can be performed as to why that difference is present and which tetrad better represents outgoing radiation in the weak-field region. When looking at the strong-field region from this distance, it is also obvious that there is more information about outgoing radiation visible close to the black holes when using the quasi-Kinnersley tetrad. This was expected, but it is helpful to notice that the difference is so explicitly apparent even at great distance from the system, which emphasizes the importance of using a tetrad that produces a Ψ_4 that is closer to purely radiative, even in the strong-field region. We will discuss the potential quantification of this difference in the final chapter of this thesis when future work is mentioned; however, the calculation itself is beyond the scope of this thesis.

5.2 Relationship between Horizon Trajectory and Curvature Changes on AH During and After Merger

5.2.1 Pre-Merger

From the visualization, we suspect that the trajectories of the individual horizons and the direction of mean curvature are related. It would be helpful, then, to analyze both the horizon trajectory data and the mean curvature maxima and minima in order to determine such a relationship. Figure 5.4 shows approximately three quarters of an orbit of the BBH system several orbits before merger. The horizons are moving in the counterclockwise direction and plotted over the lapse α of the spacetime. On the horizons is displayed the mean curvature (discussed in Section 2.3.1) with maximal values of curvature shown in red and minimal values shown in dark blue. If we follow one of the horizons through the counterclockwise orbit as it progresses, we see that the minimal values of mean curvature seem to lead the orbit, following the direction of trajectory of motion.

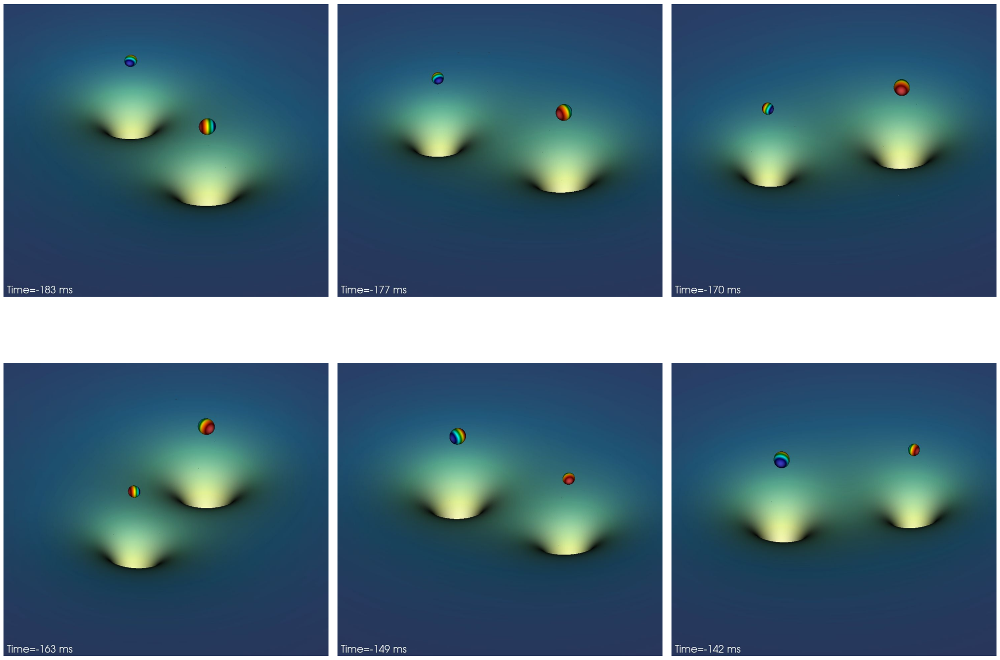

Figure 5.4: Left to right: The mean curvature of both black holes points in the direction of the trajectories of the individual black holes.

Since we are sufficiently close to merger here, the black holes are orbiting extraordinarily quickly (on the order of the speed of light c). We expect the mean curvature to point in the direction the black holes are moving since their curvature seems to be distorted by their orbital trajectory. In fact, from first glance, this seems to be what is happening.

To show this holds for our system, we calculate the approximate global maximum and minimum values of mean curvature for each timestep t using a simple iterative maximizer. We then subtract the maxima in the $x-$, $y-$, and $z-$directions from their respective minima and normalize the resultant vector so that our values fall on the interval $[0, 1]$. This is done via a simple calculation:

$$\vec{\mathrm{mc}} = \begin{bmatrix} x_{min} - x_{max} \\ y_{min} - y_{max} \\ z_{min} - z_{max} \end{bmatrix}, \qquad \vec{\mathrm{mc}} = \frac{\vec{\mathrm{mc}}}{\sqrt{\vec{\mathrm{mc}} \cdot \vec{\mathrm{mc}}}}. \tag{5.2}$$

Using the Python script in Appendix C, we can extract trajectory values $x(t)$, $y(t)$, $z(t)$ for each horizon from the simulation data and normalize, which will then allow us to compare the two datasets. Figure 5.5 shows the mean curvature direction overlaid with the trajectory of the apparent horizons for each AH1 and AH2. These plots follow the system from $t = 0M$ to right before merger at about $t = 2100M$ with the components $x(t)$ and $y(t)$ plotted individually with respect to time. Mean curvature direction is displayed in blue and trajectory at time t/M in orange. Since our system is nonprecessing, $z(t) = 0$ for all time so the plot is not included. There is a non-negligible phase shift present between the mean curvature curve and the trajectory curve in the plots for both the $x-$ and $y-$components, with one or the other lagging.

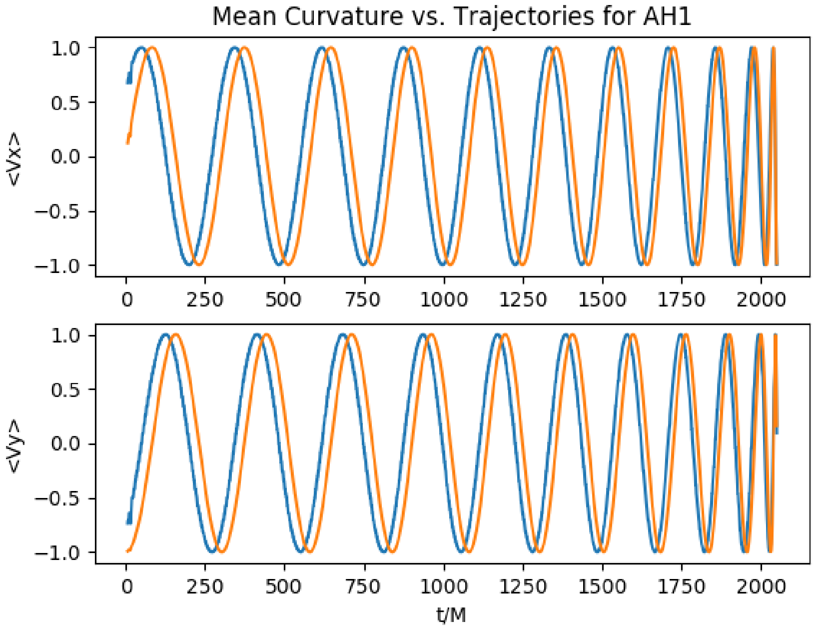

Figure 5.5: Plot of the direction of mean curvature (blue) and the trajectory of the horizon (red). The top plot shows the $x-$component with respect to time, with y and z below.

AH1

Figure 5.5 shows the mean curvature in blue overlaid with the trajectory in red of apparent horizon 1 (AH1) for $t = 0$ to 2100M approximately. Recall that per our simulation parameters AH1 refers to the smaller of the two black holes whose spin points in the negative direction. The mean curvature direction has a very small phase shift with respect to the trajectory of AH1 in the positive direction throughout the inspiral of the BBH system. However, it is obvious that the mean curvature direction and trajectory are intimately related throughout inspiral and up to merger, which is an interesting conclusion. It also seems to be the case that the curves approach synchronicity as merger approaches; however, this may not be the case. We will discuss this possibility further later in this section.

It is important to note that the normalization, while helpful to analyze phase shifts in the periodic direction, sacrifices any amplitudinal shifts present in the data. This does not hinder our results, however, since we are interested only in whether the directions of the mean curvature and trajectories compare, not the explicit values of either parameter.

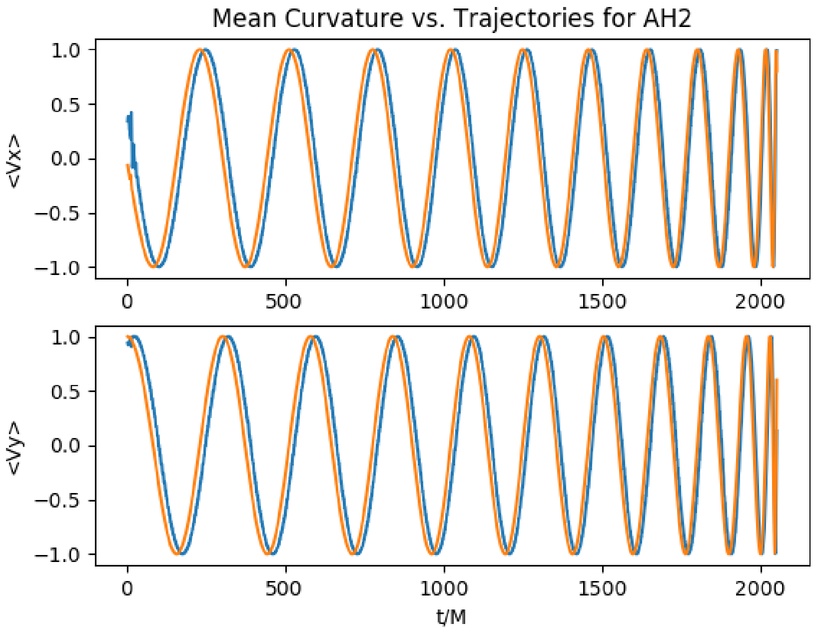

Figure 5.6: Plot of the direction of mean curvature (blue) tracking the trajectory of the horizon (red). The top plot shows the x component with respect to time, with y and z below.

AH2

In Figure 5.6 mean curvature points in the direction of horizon trajectory, so this time the mean curvature is shifted in the negative direction and lags behind the trajectory. The phase shift also seems more apparent in these plots; the mean curvature is further from the trajectory of AH2 than it was in the case of AH1. There are several reasons this may be occurring. We will discuss this in the forthcoming paragraphs. Finally, it seems again that the two curves seem to synchronize as the black holes approach merger, thus sending the phase shift to zero. However, in the coming few sections we will find that this is not actually the case.

5.2.2 Differences

There are two main features to these plots, and thus two important questions can be asked: first, is this phase shift constant, and, second, how are the directionality and amount of the phase shift ϕ determined? To address the first, notice that the periodicity of the waveforms shrinks as merger approaches, thus distorting the plots so the waveforms seem to be approaching synchronicity. We can calculate the exact amount of phase shift between the two curves via the following calculation.

$$\psi_1 = e^{i\omega t} = \cos(\omega t) + i\sin(\omega t) = x_1 + iy_1$$

$$\psi_2 = e^{i(\omega t+\phi)} = \cos(\omega t+\phi) + i\sin(\omega t+\phi) = x_2 + iy_2$$

and

$$\begin{aligned}
\frac{\psi_2}{\psi_1} &= e^{i\phi} = \frac{\psi_2\bar{\psi_2}}{\psi_1\bar{\psi_2}} = \frac{1}{\psi_1\bar{\psi_2}} \\
&= \frac{1}{(\cos(\omega t) + i\sin(\omega t))(\cos(\omega t+\phi) - i\sin(\omega t+\phi))} \\
&= \frac{1}{x_1x_2 + y_2y_1 + i(-x_2y_1 + x_1y_2)} \\
&= x_1x_2 + y_1y_2 + i(x_2y_1 - x_1y_2) \\
&= \cos\phi + i\sin\phi
\end{aligned}$$

so

$$\phi = \arctan\left(\frac{\sin(\omega)}{\cos(\omega)}\right) = \arctan\left(\frac{x_2y_1 - x_1y_2}{x_1x_2 + y_2y_1}\right) \tag{5.3}$$

Above, ψ_1 and ψ_2 give the $x, y-$components of the trajectory and mean curvature data respectively, and ϕ represents the shift between mean curvature and trajectory. See Appendix D for the Python script which implements this calculation and plots the phase shift of (respectively) AH1 and AH2 with respect to time. The result of this analysis can be seein in Figures 5.7a and 5.7b.

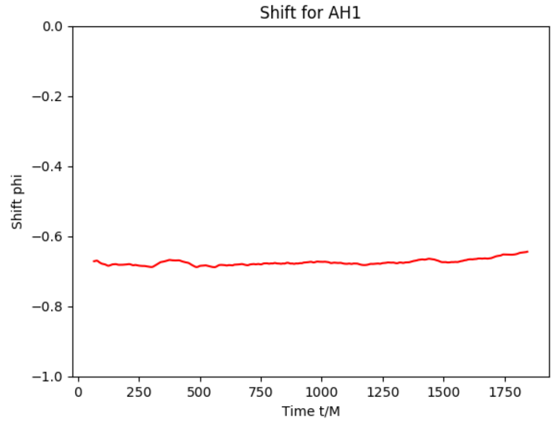

(a) Running averages for phase shift of AH1 plotted in red. The phase shift seems to remain constant throughout inspiral.

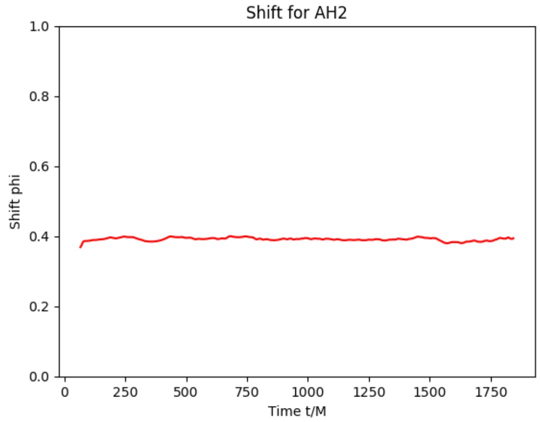

(b) Running averages for phase shift of AH2 plotted in red. The phase shift seems to remain constant throughout inspiral.

In Figures 5.7a and 5.7b, we have plotted the shift of the mean curvature relative to the values of the trajectory versus time t/M. In the case of AH1, the phase shift hovers around $\phi_1 = +0.4 \approx +0.127\pi$ radians, and for AH2 we have the phase shift staying around $\phi_2 = -0.7 \approx -0.223\pi$ radians. Note that the original data values for phase shift are subject to fluctuations due to either numerical noise present in the data or as a result of the linear interpolation function used to project both mean curvature and trajectory to the same set of points. Since we are interested in determining the behavior of the phase shift up to merger, it is important to make an analysis which holds independent of noise present in the plots. To aid us in this endeavor, we have employed the noise-reduction technique of *running averages* where, given a point p in the dataset, we average over a number of points before and after it to obtain a new value for that point:

$$p_{new} = \frac{1}{n+1} \sum_{i=-n/2}^{n/2} p_i \tag{5.4}$$

for some even n. In Figures 5.7a and 5.7b we have used $n = 30$, so 15 points before p_0 and 15 points after are included in the average for a total of 31 points being summed over. The result of this is what is being plotted in Figures 5.7a and 5.7b. Regardless of proximity of the apparent horizons (up until they merge), we can conclude that the directions in which both trajectory and mean curvature are pointing remain nearly the same relative to each other during inspiral.

It is important to also notice that in Figure 5.7b, at around $t = 1600M$, there is a slight increase in the phase shift. This potentially means that very close to merger the direction of mean curvature begins to head toward that of the trajectory in the horizon that begins with the two values more out of phase. The same cannot necessarily be said for the results displayed in Figure 5.7a and, in fact, due to the numerical noise present, we cannot say anything conclusive about what happens to the direction of mean curvature as merger approaches without more accurate numerical data.

Addressing the second question (how spin/mass ratio and phase shift amount/direction are related) is significantly more computationally intensive than addressing the first. A concrete answer would require more simulations to be performed with different spin/mass ratio combinations, so instead we will provide several educated guesses and briefly discuss those. We suspect that direction of phase shift is determined specifically by frame-dragging effects, or distortions in spacetime due to rotation of a massive object, of the individual black holes themselves. In fact, we can say something rather concrete regarding the phase shift and its relationship to the frame-dragging effects that occur close to black holes.

Frame dragging

We have already defined *frame dragging* to be the distortions of the spacetime metric due to the rotation of a black hole. This means that particles very close to such an object are unable to remain stationary but instead move along with the rotation of the black hole. Recall from Chapter 2 that the *stationary limit surface* is the point beyond which stationary particles cannot exist. It is timelike except at $\theta = 0,\ \pi$ (the poles), where it coincides with the event horizon and is null. Inside this surface, in a region of spacetime called the *ergosphere*, one must travel in the direction of rotation of the black hole ϕ but would still be able to move toward or away from the event horizon to either demise or escape. The stationary limit surface occurs at

$$(r - M)^2 = M^2 - a^2 \cos^2 \theta \tag{5.5}$$

(in Boyer-Lindquist coordinates) which, for a Schwarzschild black hole ($a = 0$), coincides with the event horizon at $r = 2M$ [12]. We expect that the frame-dragging effects of a Kerr black hole are directly related to the directionality and magnitude of the phase shift between the mean curvature and trajectories of the apparent horizons. To verify whether this is true, we can compute the angular velocities of the two black holes Ω_1 and Ω_2 and compare their ratio Ω_1/Ω_2 with that of the observed phase shifts for each horizon ϕ_1/ϕ_2. To calculate Ω_1 and Ω_2, we must first find the radii of the event horizons of each black hole using known spins $\chi_1 = a_1/m_1$ and $\chi_2 = a_2/m_2$:

$$r_1/m_1 = 1 + \sqrt{1 - \chi_1^2}, \tag{5.6}$$

$$r_2/m_2 = 1 + \sqrt{1 - \chi_2^2}, \tag{5.7}$$

and then use those to find the angular velocities [30]:

$$m_1\Omega_1 = \frac{a_1}{r_1^2 + a_1^2}, \tag{5.8}$$

$$m_2\Omega_2 = \frac{a_2}{r_2^2 + a_2^2}, \tag{5.9}$$

where m_1 and m_2 are the masses of the individual black holes. The ratio between the two is then

$$\gamma_{FD} = \frac{m_1\Omega_1}{m_2\Omega_2}\frac{1}{q} = \frac{\Omega_1}{\Omega_2}, \tag{5.10}$$

where the mass ratio $1/q$ is used to cancel out the masses m_1 and m_2. Substituting in $a_1 = -0.44$ and $a_2 = +0.33$ gives $\gamma_{FD} \approx -1.66541$. To compute the ratio γ_{obs} between the observed phase shifts, we simply average over the data for all time up to merger. The explicit calculation is the following:

$$\gamma_{obs} = \frac{\frac{1}{n}\sum_{t=0}^{n}\phi_1(t)}{\frac{1}{n}\sum_{t=0}^{n}\phi_2(t)} \tag{5.11}$$

for the total number of timesteps n and time t. The result is $\gamma_{obs} \approx -1.72132$, so the magnitude of the difference between the results is $|\gamma_{FD} - \gamma_{obs}| = 0.05591$ and has a relative error

$$\epsilon = \frac{|\gamma_{FD} - \gamma_{obs}|}{|\gamma_{FD}|} \approx 0.03357. \tag{5.12}$$

This relative error is not large, but for our hypothesis to be correct, the two ratios should be approximately equivalent. Our observed data is extremely noisy and a computation of the standard deviation σ of the measurements would be helpful in telling us how accurate we expect our results to be.

$$\sigma = \sqrt{\frac{1}{n}\sum_{i=0}^{n}\left(\frac{\phi_1(i)}{\phi_2(i)} - avg\left(\frac{\phi_1}{\phi_2}\right)\right)^2} \tag{5.13}$$

$$= 0.02978. \tag{5.14}$$

Then the difference $|\gamma_{FD} - \gamma_{obs}| = 0.05591$ is within 2σ. Furthermore σ itself tell us that our shift values fluctuate by approximately $\pm\sigma$ radians from the mean of the array of ratios ϕ_1/ϕ_2. Although this is not a significantly large amount, fluctuations of $|sigma|$ correspond to $\frac{5.3604}{\pi}$ degree variations due to noise. This means that the noise in our data contributes to the inaccuracy of γ_{obs}, and it is safe to say that our results may imply that the relationship between frame dragging effects and our phase shift parameters does in fact exist. More work needs to be done in order to confirm this relationship, namely, more simulations need to be run to verify this holds for different mass/spin configurations, but this information lays the groundwork for progress to be made.

5.2.3 Post-Merger

We now must discuss the behavior of the mean curvature once the horizon has settled into its final black hole (AH3). Per the simulation parameters, the final black hole has a trajectory of approximately 134 km/s and a final spin of ≈ 0.7. Table 5.1 shows the final parameters of AH3 per three simulation runs of GW150914 using LazEv as reported in [20].

Run	m_{rem}/M	α	V (km/s)
N100	0.952015	0.691961	131.79
N110	0.952020	0.691965	133.35
N120	0.952021	0.691969	134.38

Table 5.1: Mass, spin, and angular velocity of the final Kerr black hole of GW150914.

Run N100 has the coarsest resolution, and runs N110 and N120 have resolutions 1.1 and 1.2 times globally respectively that of the N100 run. The parameter m_{rem}/M gives the final mass of the black hole over the original mass $M = M_1 + M_2$ of the system, $\alpha = S/M^2$ is the final intrinsic spin of the black hole, and V is the coordinate recoil velocity in km/s. These data clearly show that the spin is significantly more prominent a gravitational effect than the final velocity of the black hole. Figure 5.8 shows the resultant horizon with settled curvature after merger has completed.

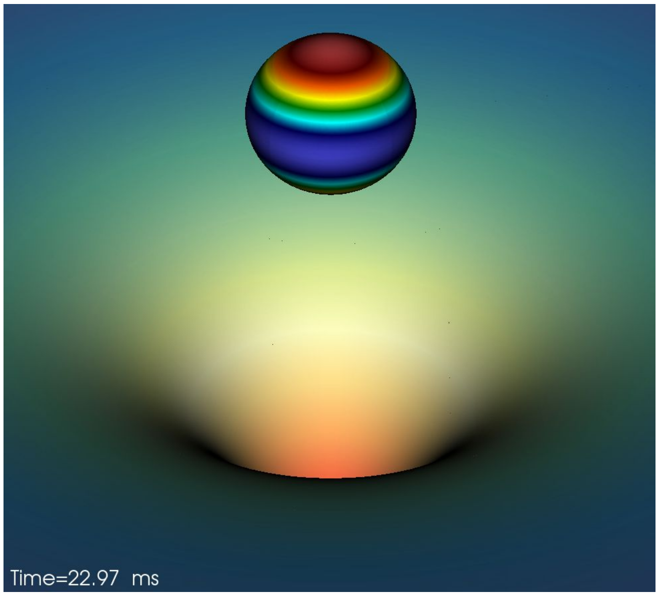

Figure 5.8: AH3 after ringdown with settled mean curvature displayed on the horizon of the black hole.

The maximum values of the mean curvature are still in red, while the minimum values are in blue. There are two maxima that lie on $\theta = 0$ and π, so a vector pointing from the bottom to the top maximum value (in the positive $z-$direction) lies in the direction of the spin of the final black hole. This means that in a spin-dominated system, mean curvature will point in the direction of the spin.

Chapter 6

Conclusions and Discussions

6.1 Future Work

Here we discuss some of the possible avenues for continuation of the research presented in this thesis.

6.1.1 Radiation

Quantitative comparison of PsiKadelia and quasi-Kinnersley

A quantitative comparison of PsiKadelia versus quasi-Kinnersley would involve performing a second simulation that extracts radiative data at $r = 100, 75, \ldots, a$, for $a =$ binary separation. Since the quasi-Kinnersley frame is transverse, we expect the associated tetrad to consistently produce values closer to outgoing radiation as we decrease r from $r : \infty \to a$. This will be one of the follow up studies motivated by the results of this thesis.

Determining the eigenvalues and eigenvectors of Q

Recall from Section 3.8.2 our discussion of the matrix Q_{ab}. There are three eigenvalue/eigenvector pairs associated with the Weyl Tensor C_{ab} that are all coordinate- and tetrad-independent, so how do we know which ones correspond to a spacetime that behaves asymptotically like Kerr? Consider again the characteristic polynomial (Equation 3.146) associated with matrix Q_{ab} [8]. We can rewrite in the following form:

$$P = |Q - \Lambda| = \psi^3 - I\psi + 2J = 0, \tag{6.1}$$

where Λ is a matrix with eigenvalues on the diagonal and ψ correspond to the three values of Ψ_2^T in the transverse frames at any point in the spacetime. This means that as $t \to \infty$ we should have Ψ_2 as the only nonzero component of the Weyl Scalars. The terms I and J can be computed as follows:

$$I = \frac{1}{2} C^a{}_b \tag{6.2}$$

$$J = -\frac{1}{6} C^a{}_b C^b{}_c C^c{}_a \tag{6.3}$$

To help us determine which eigenvalue ψ should be used, we return again to the Baker-Campanelli specialty index (Equation (3.127)) where $S = 27J^2/I^3$ and express our roots as follows:

$$\psi = -\frac{3J}{2I} Z(S) = -\frac{3J}{2I} \frac{[W(S)]^{1/3} + [W(S)]^{-1/3}}{\sqrt{S}}, \tag{6.4}$$

for $W(S) = \sqrt{S} - \sqrt{S-1}$ [8]. Recall that $S \to 1$ in late times of a numerical simulation of a spacetime in which a black hole is approaching an equilibrium state. Only one branch of $Z(S)$ is analytic at these late times. Define ψ^0 to be the expansion of ψ about $S = 1$ so that

$$\psi^0 = \frac{J}{I}\left[-3 + \frac{4}{3}(S-1) + \cdots\right]$$

is the preferred eigenvalue for a given spacetime. Currently, a numerical method is used [8], which directly solves the eigenvalue problem. However, that construction introduces numerical error and an analytical solution to this question would be ideal. An analytic solution involves finding the roots of the cubic characteristic equation $|Q - \Lambda| = \psi^3 - I\psi - 2J$ and choosing the one that is analytic near $S = 1$. In practice, this is done by either choosing the eigenvalue with the largest norm or the largest real part in magnitude so long as $|S - 1| < 1$[8]. Future work would involve the implementation of such an analytic method. Work has been done by [8], but no significant progress has been made.

6.1.2 Mean Curvature

Frame Dragging

As discussed in Chapter 5, the frame dragging-effects of a Kerr black hole may have a significant impact on the phase shift between the trajectories and the mean curvature of black holes in a binary system. We have already shown that our data supports this relationship, but further simulations must confirm this holds for more than just our current configuration and that no other factors are at play. We would like to use data from various catalogs and complete new simulations as needed for both aligned and anti-aligned spins of different sizes, with different mass ratio values q, including equal mass binaries and potentially those with extreme mass ratios.

Post-Merger

At the end of Chapter 5, we briefly discussed how at post merger, the spin of the black hole is the dominating source of curvature and so the mean curvature falls into alignment with the spin rather than the velocity of the black hole. This needs confirmation with other simulations, but also the need arises for quantification in this simulation as well. If we take a vector pointing in the direction of the spin (namely from the bottom-most maximum value of mean curvature to the top-most) and plot its directional changes from merger through ringdown, we should find that this vector converges to the direction of the spin itself. Work in this area is ongoing.

6.2 Conclusion

A significant portion of this thesis was dedicated to the study of gravitational radiation and various extraction techniques involving different Weyl scalars. To do this, we set up Newman-Penrose formalism and defined tetrads, without which a complete understanding of the importance of the Weyl scalars would not have been possible. Understanding the differences between the two tetrads used in gravitational wave extraction, quasi-Kinnersley and PsiKadelia, is vital to help us hypothesize and accurately determine which tetrad is more accurate when displaying outgoing radiation.

In fact, we visualized the Ψ_4 component of the Weyl scalars using both the PsiKadelia tetrad and the quasi-Kinnersley tetrad. We were able to analyze each output and found that quasi-Kinnersley produced a Ψ_4 which more accurately represented radiation moving outwards from the sources. This was what was expected, since Ψ_4 exists in a transverse frame ($\Psi_1 = \Psi_3 = 0$) which means Ψ_4 is a linear combination of only $\Psi_0,\ \Psi_2,$ and Ψ_4 rather than of all five of the Weyl scalars. This means that using the quasi-Kinnersley tetrad, we arrive at a Ψ_4 that is closer to displaying purely outgoing radiation.

Improvements can be made to this analysis; furthering it would include quantifying the results and showing that they hold throughout the entire simulation, rather than just in the few timeslices that were chosen. As always, we would want to test both tetrads on several mass/spin configurations of BBH systems to see whether one tetrad is preferred in all scenarios.

We also discussed in great detail why apparent horizons are much more efficient to compute than event horizons, and how to numerically locate an apparent horizon in a spacetime. The importance of mean curvature and how it is numerically evolved with a spacetime were both addressed as they pertained to the results included in the final two chapters of this thesis. Furthermore, from the visualization of the simulation done of LIGO's gravitational wave detection GW150914, it became clear that some relationship existed between the mean curvature of the apparent horizons and their trajectories.

After visualizing the merger behavior, we expected the mean curvature of the apparent horizons and the trajectory to coincide nicely; instead, we found that the mean curvature lagged behind (or preceded) the trajectory of the black holes. This led us into an investigation of the phase shift parameter ϕ between the mean curvature and the trajectory. An interesting result of this analysis is that ϕ, for both black holes, seems to remain constant up until relatively close to merger. It also seemed that, for AH1, the shift began to trend slightly toward zero as merger approached. Unfortunately, due to noise in the phase shift data, we cannot say with any certainty whether this will be true for all cases or even definitively for our AH1 or AH2, since we do not see the same subtle trend in both cases.

We also would like to know why this phase shift is occurring. A suspicion we have is that the magnitude of the phase shift is related to the mass ratio. The smaller black hole AH1 seems more out of phase than the larger one AH2, which potentially could imply that $|\phi|$ is inversely proportional to the mass ratio q of the system. Recall that in Chapter 5 we found the mass ratio q vanished when computing the ratio of angular velocities $m_1\Omega_1/m_2\Omega_2$ of the black holes, but if we wanted to resolve one of the angular velocity parameters, or if we wanted to see the effects of parameters on ϕ, q may have a significant impact. This question is another that cannot be answered without the analysis of other, differently configured, binary black hole systems. The phase shift has a certain directionality component; recall that for AH1 the mean curvature lagged behind the trajectory, whereas for AH2 the mean curvature preceded the trajectory. The suspicion is that this directionality component is due to the frame-dragging effects of a Kerr black hole. Our analysis and computation at the end of Chapter 5 suggest that this is likely the case, and that the frame dragging has a significant impact on the behavior of the mean curvature.

Our final result was that during post merger, the mean curvature moves from the plane into the direction of the spin of the final black hole. Since the final black hole spins at approximately ≈ 0.7 and travels at a velocity of ≈ 134 km/s, which is much smaller at $V/c \approx 4.5 \times 10^{-4}$, it is clear that the spin is the more dominant of the two sources of curvature. This is why we expect the mean curvature to settle into the direction of the spin of the final black hole. Although we were unable to show this numerically, the visualization shows this settling quite obviously. Future work on this front would be to complete a quantitative analysis of the behavior of the mean curvature of the resultant final black hole and confirm our hypothesis regarding its settling in the spin direction after a turbulent-looking period right after merger.

This thesis was helpful for delving deeply into areas which are not normally covered in courses on General Relativity and laid the groundwork to complete more involved research in the coming years. We would like to continue to study the horizon curvature and see if a relationship between linear momentum and mean curvature can be shown and fully quantified. More simulations will also be run to test whether our results hold for more simulations of BBH systems other than this configuration of GW 150914.

Acknowledgements

The author gratefully acknowledges the NSF for financial support from Grant No. PHY-1607520 Computational resources were provided by XSEDE allocation TG-PHY060027N and by NewHorizons and BlueSky Clusters at Rochester Institute of Technology, which were supported by NSF grant No. PHY-0722703, DMS-0820923, AST-1028087, and PHY-1229173.
The author thanks Yosef Zlochower and James Healy for their help with several technical aspects of this thesis.

Appendices

Appendix A

Parameters for Visualization

```
###################################################
# Opening horizons
###################################################
OpenDatabase("localhost:D:/patched ahs/AH_1.xmf")
AddPlot("Pseudocolor","mean curvature")

OpenDatabase("localhost:D:/patched ahs/AH_2.xmf")
AddPlot("Pseudocolor","mean curvature")

OpenDatabase("localhost:D:/patched ahs/AH_3.xmf")
AddPlot("Pseudocolor","mean curvature")

SetActivePlots((1, 2, 3))
p = PseudocolorAttributes()
p.colorTableName = "hot_desaturated"
SetPlotOptions(p)

AddOperator(’Transform’)
t = TransformAttributes()
t.doTranslate, t.translateZ = 1, 12
SetOperatorOptions(t)

DrawPlots()
#########################
#Open radiation (open after horizon files)
#########################
OpenDatabase("localhost:D:/Data/rpsi4.xy.h5")
DefineScalarExpression("rpsi4","polar_radius(<Carpet AMR-grid>)*<ANTENNASIMPLE--rpsi4>")
AddPlot("Pseudocolor","rpsi4")

#Radiation
SetActivePlots(2)

#Radiation pseudocolor attributes
p=PseudocolorAttributes()
p.colorTableName = "Accent"
p.opacityType,p.opacity = 1,0.5
p.minFlag, p.min = 1, -.01
p.maxFlag, p.max = 1, .01
SetPlotOptions(p)

#Radiation Operators
AddOperator(’Project’)
#AddOperator(’Cylinder’)
AddOperator(’Elevate’)
#AddOperator(’Transform’)
#AddOperator(’Box’)
```

```
#Radiation Operator Attributes
#c = CylinderAttributes()
#c.point1, c.point2, c.radius, c.inverse = (0, 0, -100000), (0, 0, 100000), 10, 1
#SetOperatorOptions(c)

#t = TransformAttributes()
#t.doScale, t.scaleZ = 1, 10000
#SetOperatorOptions(t)


#v = GetView3D()
#v.viewNormal = (0, -1.5, 1)
#v.imageZoom = 3.5
#SetView3D(v)
DrawPlots()


###############################################
#Opening lapse
###############################################

OpenDatabase("localhost:D:/Data/alp.xy.h5")

AddPlot("Pseudocolor","ADMBASE--alp")

#Attributes
p=PseudocolorAttributes()
p.colorTableName = "Spectral"
SetPlotOptions(p)

#Operator
AddOperator(’Project’)
AddOperator(’Elevate’)
AddOperator(’Transform’)

t=TransformAttributes()
t.doScale, t.scaleZ = 1, 10
SetOperatorOptions(t)

v = GetView3D()
v.viewNormal = (0, -1.5, 1)
v.imageZoom = 3.5
SetView3D(v)
DrawPlots()
################################
#Opening near merger horizons
################################

OpenDatabase("localhost:D:/PE82nearMerger/alp.xy.h5")
AddPlot("Pseudocolor", "ADMBASE--alp")

OpenDatabase("localhost:D:/PE82nearMerger/AH_1.xmf")
AddPlot("Pseudocolor", "mean curvature")

OpenDatabase("localhost:D:/PE82nearMerger/AH_2.xmf")
AddPlot("Pseudocolor", "mean curvature")

OpenDatabase("localhost:D:/PE82nearMerger/AH_3.xmf")
AddPlot("Pseudocolor", "mean curvature")
#Horizon Attributes
SetActivePlots((4,5,6))
p=PseudocolorAttributes()
p.colorTableName = "hot_desaturated"
SetPlotOptions(p)

#Horizon TranslateOperator
AddOperator(’Transform’)
t=TransformAttributes()
t.doTranslate, t.translateZ = 1, 6

#Lapse Attributes
SetActivePlots(3)
q=PseudocolorAttributes()
q.colorTableName = "Spectral"
SetPlotOptions(q)
```

```
#Lapse Scale Operator
AddOperator('Project')
AddOperator('Elevate')
AddOperator('Transform')
s=TransformAttributes()
s.doScale, s.scaleZ = 1, 5
SetOperatorOptions(s)

DrawPlots()
```

Appendix B

Code for Visualization

zoomCode.py

```
######
#Python script which allows for zooming with f(t) = A*tanh(t) + B for constants A and B
    and timestep (or frame) t.
######
from math import *

######Saving image
im= SaveWindowAttributes()
im.family = 0
im.format = im.JPEG
 #Can also be PNG, BMP, etc.
im.width = 977
im.height = 977

######Initial values - change based on user's need
start = 954 #Frame to start
end = 1600 #Frame to end
startZoom = 60
endZoom = 10

######Set pan and focus. These are currently specific to my needs, but modify (or
    remove) them as needed.
x_pan = 0.001806491710049952
y_pan = -0.01106605762463292
x_focus = 1.666671752929688
y_focus = 1.666671752929688
z_focus = -15.00431060791016
periodScale = .05 #elongates the period so that the zoom is not abrupt.

######SET ONLY ONE OF THE FOLLOWING TO TRUE AND THE OTHER TO FALSE. IF ZOOMING IN AND
    OUT, SET zoomBoth = True.
#######IF OUT ONLY, zoomOut = True.
#######IF IN ONLY zoomOut = False AND zoomBoth = False.
zoomBoth = True
zoomOut = False

######To determine if zooming in or out.
zoomOutIn = False #Set to True if you want to zoom out then in (or vice versa)
zoomInOut = False
zoomIn = False
###################################
##From here down, nothing should need modification unless you need to add pan/focus
###################################

######function parameters

if zoomOut == True:
```

```
   scaleFactor = startZoom/2
   shiftValue = startZoom/2 + endZoom
eif zoomIn == True:
   scaleFactor = endZoom/2
   shiftValue = endZoom/2 + startZoom
######Set view
v = GetView3D()
v.imageZoom = startZoom
#v.imagePan = (x_pan,y_pan)
#v.focus = (x_focus, y_focus, z_focus)
SetView3D(v)
for time in range(start,end):
######
#Loops over times from start to end, saves an image at each timestep, and zooms in a
    little bit (based on tanh function)
######
   TimeSliderSetState(time)
   im.fileName = "lapse_%04d.jpg" % (time -start)
      SetSaveWindowAttributes(im)
   SaveWindow()
   if zoomOut == True:
      z = -scaleFactor*tanh(periodScale*(time-start)) + shiftValue
   elif zoomOutIn == True:
      if time < end - 2/periodScale :
         z = -scaleFactor*tanh(periodScale*(time-start)) + shiftValue
      else:
         z = scaleFactor*tanh(periodScale*(time-end + 2/periodScale)) + shiftValue
   elif zoomInOut == True:
      if time < end - 2/periodScale :
         z = scaleFactor*tanh(periodScale*(time-start)) + shiftValue
      else:
         z = -scaleFactor*tanh(periodScale*(time-end + 2/periodScale)) + shiftValue
   elif zoomIn == True: #here, we just zoom in at the end (for start, change end to
       start)
      z = scaleFactor*tanh(periodScale*(time-end)) + shiftValue
   else:
      z = v.imageZoom
   v.imageZoom = z
   v.imagePan = (x_pan,y_pan) #These aren't necessary (pan and focus), but help to
       stabilize jumpy images
   v.focus= (x_focus, y_focus, z_focus)
   SetView3D(v)
```

Appendix C

Mean Curvature vs. Trajectory Plots

read_data.py

```
def find_match(ah1,ah2):
    #finds iteration number where merger occurs
    t1, x1, y1, z1, vx1, vy1, vz1 = read_trajectories(ah1)
    t2, x2, y2, z2, vx2, vy2, vz2 = read_trajectories(ah2)
    i=7000
    while x1[i] != x2[i]:
        i+=1
    return i
```

readfiles.py

```
#####
#Code that reads/plots MC vs. Trajectory as seen in Chapter 5.
#####

import h5py
import numpy as np
import matplotlib.pyplot as plt
from read_data import find_match

######
#Data files
#Local paths are for convenience only.
######
ah1 =
    'C:/Users/nicol/OneDrive/Documents/Research/thesis/horizons/ShiftTracker0.asc/ShiftTracker0.asc'
ah2 =
    'C:/Users/nicol/OneDrive/Documents/Research/thesis/horizons/ShiftTracker1.asc/ShiftTracker1.asc'
AH1 = 'D:/Data/AH_1.h5' #large horizon
AH2 = 'D:/Data/AH_2.h5'
AH3 = 'D:/Data/AH_3.h5'

track1 ='C:/Users/nicol/OneDrive/Documents/Research/thesis/horizons/track1.txt'
track2 ='C:/Users/nicol/OneDrive/Documents/Research/thesis/horizons/track2.txt'

def read_trajectories(file1):
######
#Reads and shifttracker data and gets x,y,z,vx,vy,vz and time t.
######
  h1 = open(file1,'r')

  t=[]
  x=[]
  y=[]
```

```
  z=[]
  vx=[]
  vy=[]
  vz=[]
  vec_x=[]
  vec_y=[]
  vec_z=[]
  for line in h1:
      line=line.strip()
      columns=line.split()
      t.append(float(columns[1]))
      x.append(float(columns[2]))
      y.append(float(columns[3]))
      z.append(float(columns[4]))
      vx.append(float(columns[5]))
      vy.append(float(columns[6]))
      vz.append(float(columns[7]))
  for i in range(1,len(vx)):
    norm = np.sqrt(vx[i]**2 + vy[i]**2 + vz[i]**2)
    vec_x.append(vx[i]/norm)
    vec_y.append(vy[i]/norm)
    vec_z.append(vz[i]/norm)
  return t, x, y, z, vec_x, vec_y, vec_z

def read_MC(file):
  file = h5py.File(file, "r")

  # This reads the h5 file and gets an ordered list of dump iterations
  # Mostly written by Yosef

  groups = [f for f in file ]

  its = [ int(name[3:]) for name in groups if name[0:3]==u'it_' ]

  its = sorted(its)
  xold = -1.0e99
  yold = -1.0e99
  zold = -1.0e99

  xmid = -1.0e99
  ymid = -1.0e99
  zmid = -1.0e99
  iterates=[]
  xs=[]
  ys=[]
  zs=[]
  #cyle over iterations
  for iteration in its:
    max = -1e99
    min = 1e99

    xavg = 0
    yavg = 0
    zavg = 0

    num_points = 0
    # For each iteration, cycle over 6 patches
    for patch in range(6):
      name = u'it_{0}/h_1/p_{1}/'.format(iteration, patch+1)
      x = file[name+"x"][:]
      y = file[name+"y"][:]
      z = file[name+"z"][:]
      mc = file[name+"mc"][:]

      ilen = len(x)
      jlen = len(x[0])
      num_points += ilen * jlen

      for i in range(ilen):
        for j in range(jlen):
          xavg += x[i,j]
          yavg += y[i,j]
          zavg += z[i,j]
```

```
          if mc[i,j] > max:
            max = mc[i,j]
            xmax = x[i,j]
            ymax = y[i,j]
            zmax = z[i,j]
          if mc[i,j] < min:
            min = mc[i,j]
            xmin = x[i,j]
            ymin = y[i,j]
            zmin = z[i,j]
    xavg /= (num_points)
    yavg /= (num_points)
    zavg /= (num_points)

    # dir1 is the coordinate line joining the min to max
    #vec = np.array((xmax - xmin, ymax - ymin, zmax - zmin), dtype=np.float64)
    vec = np.array((xmin-xmax,ymin-ymax,zmin-zmax),dtype=np.float64) #changed
    norm = np.sqrt(np.dot(vec, vec))

    # A missing horizon will be mapped to a sphere of size zero.
    # We drop these by checking that |vec|> 0
    if norm > 0:
      vec /= np.sqrt(np.dot(vec, vec))
      if xold > -1e99:
        # xvec is proportional to a second-order approximation of dX/dt
        xvec = np.array((xavg - xold, yavg - yold, zavg - zold),
          dtype=np.float64)
        xvec /= np.sqrt(np.dot(xvec, xvec))
        iteration = iteration*0.00434027777777778
        #iteration = (iteration-2)*float(5)/18
        iterates.append(iteration)
        xs.append(vec_mid[0])
        ys.append(vec_mid[1])
        zs.append(vec_mid[2])

        #print(iteration, xvec[0], xvec[1], xvec[2],\
         #      vec_mid[0], vec_mid[1], vec_mid[2])
      xold = xmid
      yold = ymid
      zold = zmid

      xmid = xavg
      ymid = yavg
      zmid = zavg

      vec_mid = vec.copy()
  return xs, ys, zs, iterates

def plot_premerger(ah,AH,fignum):
#####
#Plots mc vs. trajectory up to a point determined by find_match (approx timestep of
    merger).
#####
    tt,tx,ty,tz,tvx,tvy,tvz = read_trajectories(ah)
    xs,ys,zs,iterates=read_MC(AH)
    match = find_match(ah1,ah2)
    tvx1 =[0]*len(iterates)
    tvy1 =[0]*len(iterates)
    tvz1 =[0]*len(iterates)
    t1 =[0]*len(iterates)
    tol = 0.2
    i=0
    for j in range(len(iterates)):
      #i=j
      while abs(tt[i] - iterates[j])> tol:
        i+=1
      tvx1[j] = tvx[i]
      tvy1[j] = tvy[i]
      tvz1[j] = tvz[i]
      t1[j]=tt[i]
    plt.figure(fignum)
```

```
plt.subplot(2,1,1)
plt.plot(iterates[2:],xs[2:],t1[2:match-1],tvx1[2:match-1])
plt.ylabel('<Vx>')
plt.title('Mean Curvature vs. Trajectories for AH1')

plt.subplot(2,1,2)
plt.plot(iterates[2:],ys[2:],t1[2:match-1],tvy1[2:match-1])
plt.ylabel('<Vy>')
plt.xlabel('t/M')
plt.show()
```

Appendix D

Phase Shift

phase_shift.py

```
import numpy as np
from scipy import interpolate
from readfiles2 import *
from Interpolate import *
import matplotlib.pyplot as plt

def reduce_points(ah,AH,mc_reduc,traj_reduc,mx):
#####
# mx is max number t to go up to
# takes a horizon file (ah AH) and the factor the number of points in each mc
# and traj should be reduced by (mc_reduc and traj_reduc respectively).
#####
    t,vx,vy,vz = close_points(ah,AH)
    xs,ys,zs,iterates=read_MC(AH)
    mc_t = []
    mc_x = []
    mc_y = []
    t_t = []
    t_x = []
    t_y = []
    i=0
    j=0
    while iterates[mc_reduc*i]< mx:#len(xs)//mc_reduc -len(xs)//(2*mc_reduc):
    #reduces number of values we're interpolating over and limits max val
        mc_t.append(iterates[mc_reduc*i])
        mc_x.append(xs[mc_reduc*i])
        mc_y.append(ys[mc_reduc*i])
        i+=1
    while t[traj_reduc*j]< mx:#len(vx)//traj_reduc -len(vx)//(2*traj_reduc):
        t_t.append(t[traj_reduc*j])
        t_x.append(vx[traj_reduc*j])
        t_y.append(vy[traj_reduc*j])
        j+=1
    print(i,j)
    return mc_t, t_t, mc_x,mc_y,t_x,t_y

def phase_shift(mcx,trajx,mcy,trajy):
#####
#calculates phase shift between mc and traj curve
#####
    shift=[]
    y2=np.array(mcy)
    y1=np.array(trajy)
```

```
    x2=np.array(mcx)
    x1=np.array(trajx)
    y = x2*y1-x1*y2
    x = x1*x2 +y1*y2
    shift= np.arctan2(y,x)
    return shift

def running_averages(shift,r):
#####
#calculates running averages over r points of point-by-point phase shift data (shift)
#####
    avgs = []
    for j in range(r//2,len(shift)-r//2):
        i=0
        temp = 0
        while i < r//2:#r-1:
            if i == 0:
                temp+=shift[j]
            else:
                temp+=shift[j-i]
                temp+=shift[j+i]
            i+=1
        temp = temp/(2*i-1)
        avgs.append(temp)
        j+=1
    return avgs

def plot_phaseshift(ah,AH,mc_reduc,t_reduc,maxpoints):
#####
#plots smoothed phaseshift given data for traj/MC (ah/AH), reduction factors
    (mc_reduc/t_reduc), and a #max number of points to use (maxpoints)
#####
    mc_t, t_t, mc_x, mc_y,t_x,t_y = reduce_points(ah,AH,7,10,2000)
    print('reduction complete, beginning shift')
    interppoints = 500
    tvals = np.linspace(10, 1900, interppoints)
    if ah == ah1:
        val = 'AH2'
        lims = [0,1]
    else:
        val = 'AH1'
        lims = [-1,0]

    #interpolating functions - projects discrete data onto curves using linear
        interpolation
    mcx_ah = interpolate.interp1d(mc_t, mc_x, kind = 'linear')
    trajx_ah = interpolate.interp1d(t_t, t_x, kind = 'linear')
    mcy_ah = interpolate.interp1d(mc_t, mc_y, kind = 'linear')
    trajy_ah = interpolate.interp1d(t_t, t_y, kind = 'linear')

    #values
    mcx = mcx_ah(tvals)
    trajx = trajx_ah(tvals)
    mcy = mcy_ah(tvals)
    trajy = trajy_ah(tvals)

    r=30

    shift_temp = phase_shift(mcx,trajx,mcy,trajy)
    shift = running_averages(shift_temp,r)
    print(len(shift))
    plt.figure(1)
    #plt.plot(tvals[10:],shift_temp[10:],'bo') #plots raw point-by-point shift data
    plt.plot(tvals[r//2:len(shift)+r//2],shift,'r')
    plt.ylim(lims)
    plt.xlabel('Time t/M')
    plt.ylabel('Shift phi')
    plt.title('Shift for %s' %val)
    plt.show()

def avg_shift(ah,AH,mc_reduc,t_reduc,maxpoints):
###########################
```

```
#finds average of phase shift data, used in framedrag.py
###########################
    mc_t, t_t, mc_x, mc_y,t_x,t_y = reduce_points(ah,AH,7,10,2000)
    print('reduction complete, beginning shift')
    interppoints = 500
    tvals = np.linspace(10, 1900, interppoints)

    #interpolating functions
    mcx_ah = interpolate.interp1d(mc_t, mc_x, kind = 'linear')
    trajx_ah = interpolate.interp1d(t_t, t_x, kind = 'linear')
    mcy_ah = interpolate.interp1d(mc_t, mc_y, kind = 'linear')
    trajy_ah = interpolate.interp1d(t_t, t_y, kind = 'linear')

    #values
    mcx = mcx_ah(tvals)
    trajx = trajx_ah(tvals)
    mcy = mcy_ah(tvals)
    trajy = trajy_ah(tvals)
    r = len(mcx)
    shift_temp = phase_shift(mcx,trajx,mcy,trajy)
    return np.mean(shift_temp)
plot_phaseshift(ah1,AH1,5,7,2000)
plot_phaseshift(ah2,AH2,5,7,2000)
```

Appendix E

Frame Dragging

framedrag.py

```python
import h5py
import numpy as np
from phase_shift import *

def frame_drag(a1,a2,q,obs_shift1,obs_shift2):
#####
#takes spins a1,a2, a mass ratio q, and two observed shifts obs_shift1 and obs_shift2
#####
    r1 = 1+np.sqrt(1-a1**2)
    r2 = 1+np.sqrt(1-a2**2) #radii

    #angular velocities
    momega_1 = a1/(r1**2 + a1**2)
    momega_2 = a2/(r2**2 + a2**2)

    ratio = momega_1*momega_2**(-1)*q**(-1)
    obs_shift = obs_shift2*obs_shift1**(-1)
    return ratio,obs_shift

obs1=avg_shift(ah1,AH1,5,7,2000)
obs2=avg_shift(ah2,AH2,5,7,2000)
print(frame_drag(-.44,.33,.82,obs1,obs2))
# output (-1.6654100706291153, -1.721319088238584)
```

Bibliography

[1] B. Abbott et al., *Observation of Gravitational Waves from a Binary Black Hole Merger*, Phys. Rev. Lett. **116** (2016), no. 6, 061102, available at `1602.03837`.

[2] B. P. Abbott et al., *Binary Black Hole Mergers in the first Advanced LIGO Observing Run*, Phys. Rev. **X6** (2016), no. 4, 041015, available at `1606.04856`.

[3] M. Alcubierre, *Introduction to 3+1 Numerical Relativity*, Oxford University Press, 2008.

[4] John G. Baker and Manuela Campanelli, *Making use of geometrical invariants in black hole collisions*, Phys. Rev. **D62** (2000), 127501, available at `gr-qc/0003031`.

[5] John G. Baker, Manuela Campanelli, and Carlos O. Lousto, *The Lazarus project: A Pragmatic approach to binary black hole evolutions*, Phys. Rev. **D65** (2002), 044001, available at `gr-qc/0104063`.

[6] John G. Baker, Joan Centrella, Dae-Il Choi, Michael Koppitz, and James van Meter, *Gravitational wave extraction from an inspiraling configuration of merging black holes*, Phys. Rev. Lett. **96** (2006), 111102, available at `gr-qc/0511103`.

[7] Thomas W. Baumgarte and Stuart L. Shapiro, *Numerical relativity: Solving einstein's equations on the computer*, Cambridge university Press, Cambridge, 2010.

[8] C Beetle, M Bruni, L M Burko, and A Nerozzi, *Towards a wave-extraction method for numerical relativity. I. Foundations and initial-value formulation*, Phys. Rev. D **72** (2005), 024013, available at `gr-qc/0407012`.

[9] Manuela Campanelli, Bernard J. Kelly, and Carlos O. Lousto, *The Lazarus Project II: Space-like extraction with the Quasi-Kinnersley tetrad*, Phys. Rev. **D73** (2006), 064005, available at `gr-qc/0510122`.

[10] Manuela Campanelli, C. O. Lousto, P. Marronetti, and Y. Zlochower, *Accurate evolutions of orbiting black-hole binaries without excision*, Phys. Rev. Lett. **96** (2006), 111101, available at `gr-qc/0511048`.

[11] Vitor Cardoso, Leonardo Gualtieri, Carlos Herdeiro, Ulrich Sperhak, Paul M Chesler, Luis Lehner, Seong Chan Park, Harvey S Reall, Carlos F Sopuerta (section coordinators), Daniela Alic, Oscar J C Dias, Roberto Emparan, Valeria Ferrari, Steven B Giddings, Mahdi Godazgar, Ruth Gregory, Veronika E Hubeny, Akihiro Ishibashi, Greg Landsberg, Carlos O Lousto, David Mateos, Vicki Moeller, Hirotada Okawa, Paolo Pani, M Andy Parker, Frans

Pretorius, Masaru Shibata, Hajime Sotani, Toby Wiseman, Helvi Witek, Nicolas Yunes, and Miguel Zilhão, *NR/HEP: roadmap for the future*, Class. Quant. Grav. **29** (2012), 244001, available at `1201.5118`.

[12] Sean M. Carroll, *Spacetime and geometry: An introduction to general relativity*, Addison-Wesley, 2004.

[13] S. Chandrasekhar, *The mathematical theory of black holes*, Oxford University Press, Oxford, England, 1983.

[14] M. MacCallum D. Kramer H. Stephani and E. Herlt, *Exact solutions of Einstein's field equations*, Cambridge University Press, Cambridge, 1980.

[15] Peter Diener, *A new general purpose event horizon finder for 3d numerical spacetimes*, Class. Quant. Grav. **20** (2003), 4901–4918, available at `gr-qc/0305039`.

[16] Olaf Dreyer, Badri Krishnan, Deirdre Shoemaker, and Erik Schnetter, *Introduction to isolated horizons in numerical relativity*, Phys. Rev. **D67** (2003), 024018, available at `gr-qc/0206008`.

[17] James Healy, Carlos O. Lousto, Yosef Zlochower, and Manuela Campanelli, *The RIT binary black hole simulations catalog* (2017), available at `1703.03423`.

[18] Karan Jani, James Healy, James A. Clark, Lionel London, Pablo Laguna, and Deirdre Shoemaker, *Georgia Tech Catalog of Gravitational Waveforms*, Class. Quant. Grav. **33** (2016), no. 20, 204001, available at `1605.03204`.

[19] L. E. Kidder, M. A. Scheel, S. A. Teukolsky, E. D. Carlson, and G. B. Cook, *Black hole evolution by spectral methods*, Phys. Rev. D **62** (2000), 084032, available at `gr-qc/0005056`.

[20] Geoffrey Lovelace et al., *Modeling the source of GW150914 with targeted numerical-relativity simulations*, Class. Quant. Grav. **33** (2016), no. 24, 244002, available at `1607.05377`.

[21] Abdul H. Mroue, Mark A. Scheel, Bela Szilagyi, Harald P. Pfeiffer, Michael Boyle, et al., *A catalog of 174 binary black-hole simulations for gravitational-wave astronomy*, Phys. Rev. Lett. **111** (2013), 241104, available at `1304.6077`.

[22] Hiroyuki Nakano, James Healy, Carlos O. Lousto, and Yosef Zlochower, *Perturbative extraction of gravitational waveforms generated with Numerical Relativity*, Phys. Rev. **D91** (2015), no. 10, 104022, available at `1503.00718`.

[23] Andrea Nerozzi, Christopher Beetle, Marco Bruni, Lior M. Burko, and Denis Pollney, *Towards wave extraction in numerical relativity: The quasi- kinnersley frame*, Phys. Rev. D **72** (2005), 024014, available at `gr-qc/0407013`.

[24] Marcelo Ponce, Carlos Lousto, and Yosef Zlochower, *Seeking for toroidal event horizons from initially stationary BH configurations*, Class. Quant. Grav. **28** (2011), 145027, available at `1008.2761`.

[25] Frans Pretorius, *Evolution of binary black hole spacetimes*, Phys. Rev. Lett. **95** (2005), 121101, available at `gr-qc/0507014`.

[26] Saul A. Teukolsky, *Perturbations of a rotating black hole. 1. Fundamental equations for gravitational electromagnetic and neutrino field perturbations*, Astrophys. J. **185** (1973), 635–647.

[27] Jonathan Thornburg, *A fast apparent-horizon finder for 3-dimensional cartesian grids in numerical relativity*, AIP Conf. Proc. **686** (2003), 247–252, available at `gr-qc/0306056`.

[28] ———, *Event and Apparent Horizon Finders for* $3+1$ *Numerical Relativity*, Living Rev. Rel. **10** (2007), 3, available at `gr-qc/0512169`.

[29] K. P. Tod, *Looking for marginally trapped surfaces*, Class. Quantum Grav. **8** (1991), L115–L118.

[30] R. M. Wald, *General relativity*, The University of Chicago Press, Chicago, 1984.